





**Elektronische en fotonische geïntegreerde schakelingen  
voor millimetergolf-over-vezel**

**Electronic and Photonic Integrated Circuits  
for Millimeter Wave-over-Fiber**

**Laurens Bogaert**

**Promotoren: prof. dr. ir. G. Roelkens, prof. dr. ir. J. Bauwelinck  
Proefschrift ingediend tot het behalen van de graad van  
Doctor in de ingenieurswetenschappen: elektrotechniek**



**Vakgroep Informatietechnologie  
Voorzitter: prof. dr. ir. B. Dhoedt  
Faculteit Ingenieurswetenschappen en Architectuur  
Academiejaar 2019 - 2020**

ISBN 978-94-6355-383-4  
NUR 959  
Wettelijk depot: D/2020/10.500/60



Ghent University  
Faculty of Engineering and Architecture

Department of Information Technology  
iGent Tower, Tech Lane Ghent Science Park 126,  
B-9052 Ghent, Belgium

Tel.: +32 (9) 264 33 16

**Electronic and Photonic Integrated Circuits for  
Millimeter Wave-over-Fiber**

Laurens Bogaert

**Members of the examination board:**

Prof. dr. ir. Filip De Turck	(Chairman)	Ghent University
Prof. dr. ir. Gunther Roelkens	(Supervisor)	Ghent University
Prof. dr. ir. Johan Bauwelinck	(Supervisor)	Ghent University
Prof. dr. ir. Bart Kuyken		Ghent University
Prof. dr. ir. Guy Torfs		Ghent University
Prof. dr. ir. Piet Wambacq		VUB
Prof. dr. Zizheng Cao		TU/e
Dr. Amin Abbasi		Antwerp Space

Dissertation submitted to obtain the degree of  
Doctor of Electrical Engineering  
Academic year 2019-2020



# Dankwoord

Beste professoren, collega's, vrienden en familie,

Ongeveer 5 jaar geleden rondde ik mijn studies ingenieurswetenschappen af en kon ik op zoek naar een job. Uiteindelijk heb ik toen besloten om een doctoraat aan te vatten bij Johan Bauwelinck, die destijds promotor was van mijn thesis en nu dus mede-promotor van dit werk. Het onderwerp? Fotonica en elektronica combineren voor telecommunicatie toepassingen. Bij aanvang klonk dit interessant, en dat is het later ook gebleken, maar het was ook een sprong in het onbekende. Want fotonica was voor mij op dat moment toch nog een relatief nieuw onderzoeksdomein. Gelukkig kon ik rekenen op de uitgebreide kennis en het enthousiasme van mijn andere promotor, Gunther Roelkens, om mij wegwijs te maken in deze wondere wereld. Ik ben Gunther en Johan dus ook zeer dankbaar voor alle steun en feedback en om mij de kans te geven om te werken aan dit leerrijk, interessant en innovatief onderzoek. Ik kijk dan ook uit naar de toekomstige samenwerking. Vervolgens wil ik ook Guy Torfs en Piet Demeester bedanken voor het werk dat ik in het kader van het ATTO project heb kunnen doen. Vooral bij het ontwerp van de versterkers kon ik rekenen op de expertise van Guy en deze versterker is uiteindelijk een zeer belangrijk deel van dit proefschrift geworden met een ECOC-tripje naar Dublin en een virtuele OFC postdeadline paper als gevolg. Daarnaast wil ik ook nog Bart Dhoedt, Roel Baets en Johan Bauwelinck bedanken, respectievelijk hoofd van de vakgroep *Informatietechnologie* en hoofd van de onderzoeksgroepen *Photonics Research Group* en *IDLab Design*, om dit doctoraat mogelijk te maken.

De volgende categorie van mensen die ik wil bedanken, zijn mijn collega's. Dankzij de toffe sfeer zijn de afgelopen 4-en-een-half jaar voorbij gevlogen. Ik heb het geluk gehad om deel te mogen uitmaken van twee zeer collegiale

en aangename onderzoeksgroepen: *IDLab Design* en de *Photonics Research Group*. De werkrelatie was aangenaam en er was ook tijd om stoom af te laten na drukke periodes met deadlines en tape-outs: game- en filmavonden, hotpot bij Haolin, sportdagen, retreats naar de Belgische kust, etc. Een aantal collega's wil ik hier in het bijzonder vermelden. Eerst wil ik mijn IOT- eilandgenoten Joris Van Kerrebrouck, Haolin, Chia-Yi en Achim bedanken, het was aangenaam samenwerken. Overigens kaderde een groot deel van dit doctoraat in het GOA/EPIC project. Hierbij was er een zeer productieve en toffe samenwerking met Laurens Breyne, Jochem, Kasper, Jing, Amin, Hongtao, Scott, Johan en Gunther. Daarnaast waren er ook nog, dankzij het enthousiasme van Bart Kuyken, enkele studentenprojecten waarbij ik betrokken was. In het bijzonder herinner ik mij nog de LIDAR-projectjes die we dan konden demonstreren tijdens het lichtfestival en bij een architectenbureau. Natuurlijk wil ik ook de mensen bedanken die achter de schermen alles regelen en ervoor zorgen dat wij ons op ons onderzoek kunnen focussen. Bedankt Mike, Ilse ( $\times 2$ ), Kristien, Jean, Jasper, Michael en Bert. Daarnaast heb ik tijdens mijn doctoraatswerk het genoeg gehad om enkele mensen van de elektromagnetisme groep beter te leren kennen. In het bijzonder wil ik hier Sam, Quinten en Olivier vermelden voor de interessante gesprekken die we de afgelopen 4.5 jaar gehad hebben.

Vervolgens wil ik ook mijn vrienden bedanken voor de ontspanning en steun: Alexander, Thomas, Zeger, Kristof en Laura, Stef en Laura. Tegen de corona-verveling waren er de afgelopen maanden wekelijkse gaming momenten die voor ontspanning en afleiding zorgden in deze toch wel drukke periode. Uiteraard hoop ik dat we binnenkort terug eens offline kunnen afspreken en zoals steeds kijk ik uit naar onze jaarlijkse vakantie tijdens de eindejaarsperiode en ik hoop dat we dit nog lang kunnen doen.

Ten slotte wil ik dit dankwoord afsluiten door mijn familie te bedanken. In het bijzonder dank ik mijn ouders Jan en Veerle, mijn broer Alexander, en mijn grootouders Rita, Gerardus<sup>†</sup>, Gabriëlle en Maurice<sup>†</sup>. Bedankt om mij onvoorwaardelijk te steunen en altijd voor mij klaar te staan. Ik ben dankbaar voor de kansen die jullie mij gegeven hebben, zowel tijdens mijn studie en doctoraat als daarbuiten. Dit werk was niet mogelijk geweest zonder jullie, bedankt!

*Nevele, juni 2020*  
*Laurens Bogaert*

# Table of Contents

<b>Dankwoord</b>	<b>vii</b>
<b>Nederlandstalige Samenvatting</b>	<b>xxiii</b>
<b>English Summary</b>	<b>xxvii</b>
<b>List of Publications</b>	<b>xxxii</b>
<b>1 Introduction</b>	<b>1</b>
1.1 Evolution of Wireless Communication . . . . .	1
1.2 Radio over Fiber . . . . .	6
1.3 Microwave Silicon Photonics . . . . .	8
1.4 Outline of Dissertation . . . . .	10
<b>2 RF Amplification for Narrowband Communication</b>	<b>19</b>
2.1 Detection and Modulation . . . . .	19
2.2 Power budget . . . . .	20
2.2.1 Downlink with Beamforming . . . . .	20
2.2.2 Downlink without Beamforming . . . . .	22
2.3 Narrowband Amplification . . . . .	23
2.4 Resonant Transimpedance Amplifier . . . . .	25
2.4.1 Input Circuit Model . . . . .	25
2.4.2 Series Inductive Peaking . . . . .	25
2.5 Narrowband Photoreceiver . . . . .	28
2.5.1 0.1 $\mu\text{m}$ pHEMT GaAs Technology . . . . .	28
2.5.2 Photoreceiver Design and Assembly . . . . .	30
2.5.2.1 Input Circuitry . . . . .	30
2.5.2.2 LNA Design . . . . .	32
2.5.2.3 Photoreceiver Assembly . . . . .	34
2.5.3 LNA Performance . . . . .	36
2.5.3.1 Small Signal Behavior . . . . .	36

---

2.5.3.2	Linearity . . . . .	38
2.5.3.3	Noise . . . . .	39
2.5.4	State of the art . . . . .	40
2.6	Narrowband Reflective EAM Driver . . . . .	41
2.6.1	Reflective EAM Modulator . . . . .	42
2.6.2	Driver Design . . . . .	44
2.6.3	Driver Performance . . . . .	47
2.6.3.1	Small Signal Behavior . . . . .	47
2.6.3.2	Linearity . . . . .	50
2.6.3.3	Noise . . . . .	52
2.7	Conclusion . . . . .	52
<b>3</b>	<b>High Linearity Optoelectronic Conversion</b>	<b>61</b>
3.1	Optical Amplification . . . . .	61
3.2	Impact on system performance: optical versus electrical amplification . . . . .	62
3.2.1	Gain . . . . .	62
3.2.2	Cost and Power Consumption . . . . .	63
3.2.3	Noise . . . . .	63
3.2.3.1	Thermal Noise . . . . .	64
3.2.3.2	Shot Noise . . . . .	64
3.2.3.3	Relative Intensity Noise . . . . .	65
3.2.4	Linearity . . . . .	65
3.2.5	Conclusion . . . . .	66
3.3	Fundamentals of a Germanium Photodetector . . . . .	66
3.3.1	Small Signal Behavior . . . . .	67
3.3.2	Linearity . . . . .	69
3.4	Traveling Wave Photodiode . . . . .	72
3.4.1	Proposed Architecture . . . . .	73
3.4.1.1	Photodetector . . . . .	73
3.4.1.2	Star Coupler . . . . .	74
3.4.1.3	Schematic Overview . . . . .	74
3.4.2	Design Procedure . . . . .	75
3.4.3	Frequency Dependent Behavior . . . . .	80
3.4.3.1	Output Impedance . . . . .	80
3.4.3.2	Transfer Characteristics . . . . .	82
3.4.4	Linearity . . . . .	85
3.4.4.1	DC Linearity . . . . .	85
3.4.4.2	RF Linearity . . . . .	88

---

3.4.5	Second Iteration TWPD . . . . .	90
3.5	Narrowband Matching of a Photodiode . . . . .	94
3.5.1	A Comparison with the Broadband TWPD Approach . . . . .	94
3.5.2	RF Passives on a Silicon Photonics Platform . . . . .	96
3.5.2.1	Capacitors . . . . .	97
3.5.2.2	Inductors . . . . .	97
3.5.3	Design and Results for an LC-Matched Single Photodetector . . . . .	98
3.5.4	Design and Results for an LC-Matched 4-PD Array . . . . .	100
3.5.5	Linearity . . . . .	101
3.6	Conclusion . . . . .	101
<b>4</b>	<b>Beamforming</b> . . . . .	<b>107</b>
4.1	Optical Beamforming Networks . . . . .	107
4.1.1	Electrical or Optical Beamforming . . . . .	108
4.1.2	Centralized or Distributed Beamforming . . . . .	109
4.1.3	True Time Delay or Phase steering . . . . .	110
4.2	True Time Delay . . . . .	110
4.2.1	True Time Delay Architectures . . . . .	110
4.2.2	Specifications . . . . .	112
4.2.3	First Generation TTD . . . . .	113
4.2.3.1	Design . . . . .	113
4.2.3.2	Post-Processing . . . . .	116
4.2.3.3	Delay Measurement . . . . .	117
4.2.4	Second Generation TTD . . . . .	118
4.3	Phase Steering . . . . .	121
4.3.1	Concept . . . . .	121
4.3.2	Optical Single Sideband . . . . .	122
4.3.3	Add Drop Ring Resonator . . . . .	124
4.3.4	First Generation Phase Steering . . . . .	125
4.3.4.1	Design . . . . .	126
4.3.4.2	Post-Processing . . . . .	128
4.3.4.3	Measurement . . . . .	128
4.3.5	Second Generation Phase Steering . . . . .	129
4.4	Performance Comparison of the Fabricated Optical Beamforming Networks . . . . .	131
4.4.1	Size . . . . .	131
4.4.2	Power Consumption . . . . .	131
4.4.3	Beamsteering Speed . . . . .	131

---

4.4.4	Insertion Loss and Variations . . . . .	131
4.4.5	Tuning Resolution and Range . . . . .	132
4.5	Conclusion . . . . .	132
<b>5</b>	<b>System Experiments</b>	<b>139</b>
5.1	Introduction . . . . .	139
5.2	Narrowband Photoreceiver . . . . .	140
5.2.1	5G New Radio . . . . .	141
5.2.2	High Data Rate . . . . .	141
5.3	Narrowband Reflective EAM Driver . . . . .	144
5.3.1	5G New Radio . . . . .	145
5.3.2	High Data Rate . . . . .	146
5.3.3	Reflective Modulator Operation . . . . .	147
5.4	Narrowband mmWave-over-Fiber RAUs . . . . .	149
5.4.1	Setup . . . . .	150
5.4.2	Multichannel Single Carrier Data Transmission . . . . .	152
5.4.3	Orthogonal Frequency Division Multiplexing . . . . .	153
5.5	Conclusion . . . . .	154
<b>6</b>	<b>Conclusions &amp; Future Work</b>	<b>159</b>
6.1	Conclusion . . . . .	159
6.2	Future Work . . . . .	161
6.2.1	Optical Beamforming Networks . . . . .	161
6.2.2	MEMS Switches for True Time Delay . . . . .	162
6.2.3	Reflective Modulator . . . . .	162
6.2.4	60 GHz . . . . .	163
6.2.5	Antenna-on-Interposer . . . . .	163

# List of Figures

1.1	Usage scenarios of 5G . . . . .	2
1.2	Global mobile data traffic 2014-2024 . . . . .	3
1.3	Mobile data traffic per application . . . . .	4
1.4	Priority frequency bands for 5G . . . . .	5
1.5	Centralized architecture with RoF fronthaul . . . . .	7
1.6	RoF implementation types . . . . .	8
1.7	Microwave photonic link . . . . .	9
1.8	Remote antenna unit for a 2x2 antenna array . . . . .	10
1.9	System architecture . . . . .	11
1.10	Antenna element . . . . .	12
2.1	Downlink with beamforming: power budget calculation. . . . .	20
2.2	Shunt-feedback transimpedance amplifier . . . . .	24
2.3	Transimpedance amplifier with detailed input circuit model. . . . .	25
2.4	Input circuitry TIA with series inductive peaking . . . . .	26
2.5	Transmitter array technology fit per EIRP . . . . .	29
2.6	Technology landscape [21]. . . . .	29
2.7	Schematic overview of the photoreceiver. . . . .	31
2.8	Input circuit seen by the LNA consisting of a photodetector-wirebond combination . . . . .	31
2.9	Amplifier stage 1 . . . . .	32
2.10	Amplifier stage 2 . . . . .	33
2.11	Amplifier stage 3 . . . . .	33
2.12	Narrowband photoreceiver assembly. . . . .	34
2.13	3-stage mmWave low noise amplifier. . . . .	35
2.14	LNA S-parameters . . . . .	36
2.15	$S_{11}$ of the LNA on the Smith chart for a $50 \Omega$ reference. . . . .	37
2.16	Simulated noise figure of the LNA for 2 and 3V supply. . . . .	39
2.17	Spurious free dynamic range of the LNA. . . . .	40
2.18	Static insertion loss of the standalone EAM. . . . .	43
2.19	Reflective modulator: EAM in front of mirror. . . . .	44

---

2.20	Reflective modulator: EAM in mirror. . . . .	44
2.21	DEIM assembly. . . . .	45
2.22	3-stage mmWave EAM driver. . . . .	46
2.23	EAM driver S-parameters . . . . .	47
2.24	$S_{11}$ of the driver shown on the Smith chart. . . . .	48
2.25	Setup for $S_{21}$ characterization of the DEIM . . . . .	49
2.26	Transfer function DEIM transmitter. . . . .	50
2.27	Setup for 1dB compression measurement of the transmitter . . . . .	51
2.28	Simulated noise figure of the driver for 2 and 3V drain supply. . . . .	52
3.1	Centralization of amplification functionality . . . . .	62
3.2	Schematic representation of the different noise contributions . . . . .	63
3.3	Stack of the iSiPP50G platform . . . . .	67
3.4	Vertical PIN Ge-on-Si photodetector . . . . .	67
3.5	Simple pin photodetector model . . . . .	68
3.6	Measured output impedance of the Ge photodetector . . . . .	69
3.7	Physical model pin photodetector . . . . .	69
3.8	Quality of fitting on the standalone Ge VPIN PD using the improved model . . . . .	70
3.9	State of the art photodetector linearity . . . . .	71
3.10	Lumped parallel photodetector configuration . . . . .	73
3.11	Star coupler . . . . .	74
3.12	Germanium traveling wave photodetector structure . . . . .	76
3.13	TWPD model for a single photodetector-loaded transmission line segment . . . . .	77
3.14	Norton equivalent of the photodetector. . . . .	79
3.15	Parallel 16-photodetector reference design. . . . .	80
3.16	Output impedance of the parallel combination of 16 photodetectors . . . . .	81
3.17	Output impedance of the 16-PD TWPD with dummy termination . . . . .	82
3.18	Output impedance of the 16-PD TWPD with open termination . . . . .	82
3.19	Effective resistance value of the $50 \Omega$ termination resistance as a function of the applied DC voltage. . . . .	83
3.20	Simulated output power photodiode structures . . . . .	84
3.21	Setup used for bandwidth measurements . . . . .	84
3.22	Normalized measured $S_{21}$ after calibration of the MZM response . . . . .	85
3.23	Setup used for DC linearity measurements . . . . .	86

---

3.24	Linearity of the dual fed standalone photodetector in function of the reverse voltage. . . . .	87
3.25	Current contributions in a terminated TWPD . . . . .	88
3.26	Setup used for TOI linearity measurements . . . . .	90
3.27	High power beamforming cell for 2 antenna elements. . . . .	92
3.28	Second generation TWPD. . . . .	92
3.29	Output impedance of the 2nd generation 8-PD TWPD with dummy termination . . . . .	93
3.30	Output impedance of the 2nd generation 8-PD TWPD with open termination . . . . .	93
3.31	Measured $S_{21}$ of the 2nd generation 8-PD TWPDs after calibrating out the MZM response . . . . .	93
3.32	Equivalent network of the LC matched photodetector . . . . .	94
3.33	Structures for narrowband matching and testing of RF passives on iSiPP. . . . .	96
3.34	Layout of the implemented LC matched single-PD . . . . .	98
3.35	Reflection coefficient at the output of the LC matched Ge photodetector as a function of the reverse bias . . . . .	99
3.36	Comparison between the measured $S_{out}$ at 3V and the simulated $S_{out}$ (single PD) . . . . .	99
3.37	Layout of the implemented LC matched 4-PD array design. . . . .	100
3.38	Reflection coefficient at the output of the LC matched 4-PD array as a function of the reverse bias. . . . .	100
3.39	Comparison between the measured $S_{out}$ at 2V and the simulated $S_{out}$ (4-PD array). . . . .	101
4.1	Beamforming gain: optical versus electrical beamforming. . . . .	108
4.2	Centralized versus distributed analog beamforming. . . . .	109
4.3	Beam squint . . . . .	111
4.4	Optical ring resonator: Group delay . . . . .	112
4.5	Switchable optical delay line. . . . .	112
4.6	Beamforming: resulting wavefronts. . . . .	113
4.7	Thermal switch. . . . .	114
4.8	True time delay optical beamforming network generation 1. . . . .	115
4.9	Thermal switch post-processing. . . . .	116
4.10	Optical delay line measurement setup. . . . .	117
4.11	Optical delay line measurement results. . . . .	118
4.12	True time delay optical beamforming network generation 2. . . . .	120
4.13	Phase steering principle. . . . .	122
4.14	Optical single sideband generation with a DD-MZM. . . . .	123

---

4.15	Phase steering principle with add drop ring resonators. . . . .	124
4.16	Transfer functions of the ADRR in function of frequency detuning ( $Q=30K$ ). . . . .	125
4.17	Parasitic PM-AM conversion due to finite Q-factor. . . . .	125
4.18	Phase steering optical beamforming network generation 1: microscope image. . . . .	126
4.19	Phase steering optical beamforming network generation 1: annotated design. . . . .	127
4.20	Microscope image of heater on add drop ring resonator . . . . .	128
4.21	Measured transfer characteristics of the adopted ADRR . . . . .	129
4.22	Phase steering optical beamforming network generation 2. . . . .	130
5.1	Setup used for photoreceiver link experiments (5G NR). . . . .	140
5.2	Photoreceiver – EVM as a function of the carrier frequency. . . . .	142
5.3	Photoreceiver – Constellation diagram at the RTO when transmitting 100/400 MBaud at 28 GHz over 21 km SSMF . . . . .	142
5.4	Photoreceiver – EVM as a function of the $V_{out,pp}$ of the LNA. . . . .	142
5.5	Photoreceiver – EVM as a function of the baud rate. . . . .	143
5.6	Photoreceiver – (a) 5 GBd, (b) 6 GBd at 27.5 GHz, OB2B. . . . .	143
5.7	Photoreceiver – 4 GBd, 27.5 GHz, 21km SSMF. . . . .	144
5.8	Setup used for EAM-driver link experiments (5G NR). . . . .	144
5.9	DEIM – EVM as a function of the carrier frequency. . . . .	145
5.10	DEIM – EVM as a function of the RF input power. . . . .	146
5.11	DEIM – EVM as a function of the baud rate. . . . .	147
5.12	DEIM – 4 GBd, 27 GHz, OB2B. . . . .	147
5.13	DEIM – EVM as a function of SSMF length. . . . .	148
5.14	DEIM – EVM degradation due to reflective operation. . . . .	148
5.15	DEIM – Received signal when unmodulated and modulated light pass over the same fiber due to reflective operation. . . . .	149
5.16	Block diagram and experimental setup for bidirectional 28 GHz RFoF link. . . . .	151
5.17	S21 narrowband RFoF link . . . . .	153
5.18	Downlink single carrier – $5 \times 400$ MBaud multiband. . . . .	154
5.19	Measured EVM in RFoF-wireless for OFDM signals – Data rate per channel = 2.34 Gb/s. . . . .	155

## List of Tables

1.1	5G Requirements for the eMBB usage scenario . . . . .	4
2.1	Power budget downlink, 8x8 antenna matrix. . . . .	20
2.2	Photoreceiver state of the art . . . . .	41
2.3	Comparison to state of the art mmWave silicon low noise amplifiers. . . . .	42
2.4	Input impedance EAM-wirebond combination at 28.5 GHz. . . . .	42
2.5	Transmitter input referred 1dB compression point . . . . .	51
3.1	GPDCTE_SVPINCFWTT_2K_15K2_600: Equivalent model values in function of the reverse bias. . . . .	70
3.2	Linearity: DC 1dB compression point . . . . .	86
3.3	Output referred third order intercept point at 28 GHz . . . . .	90
3.4	Responsivity comparison for broadband and narrowband solutions. . . . .	95
5.1	OFDM signal parameters. . . . .	154



# Glossary

## A

ADRR	Add Drop Ring Resonator
ARoF	Analog Radio over Fiber
AWG	Arbitrary Waveform Generator

## B

BCN	Beamforming Control Network
BEOL	Back End of Line

## C

CMOS	Complementary Metal-Oxide-Semiconductor
CO	Central Office
CPRI	Common Public Radio Interface
CW	Continuous Wave

## D

DEIM	Driver and EAM In Mirror
DL-RAU	Downlink Remote Antenna Unit
DRV	Driver
DUT	Device Under Test

**E**

EAM	Electro-Absorption Modulator
EBFN	Electrical Beamforming Network
EDFA	Erbium Doped Fiber Amplifier
EIC	Electronic Integrated Circuit
EIRP	Effective Isotropic Radiated Power
ESA	Electrical Spectrum Analyzer
EVM	Error Vector Magnitude

**F**

FDD	Frequency Division Duplexing
-----	------------------------------

**I**

IF	Intermediate Frequency
IoT	Internet of Things

**L**

LNA	Low Noise Amplifier
LO	Local Oscillator

**M**

MIM	Metal-Insulator-Metal
MIMO	Multiple Input, Multiple Output
MMI	Multi Mode Interferometer
MOM	Method of Moments
MPW	MultiProject Wafer
MWP	Microwave Photonics
MZM	Mach Zehnder Modulator

**N**

NF Noise Figure

**O**

O/E Optoelectronic

O1dBCP Output referred 1-dB Compression Point

OB2B Optical Back-to-Back

OBFN Optical Beamforming Network

OFDM Orthogonal Frequency-Division Multiplexing

OIP3 Output referred third order Intercept Point

ORR Optical Ring Resonator

OSSB Optical Single Sideband

**P**

PAPR Peak-to-Average Power Ratio

PC Polarization Controller

PCB Printed Circuit Board

PD Photodetector

PDK Process Design Kit

PDN Power Distribution Network

pHEMT Pseudomorphic High-Electron Mobility Transistor

PIC Photonic Integrated Circuit

**Q**

QAM Quadrature Amplitude Modulation

**R**

RAN Radio Access Network

RAU Remote Antenna Unit

RFG	RF Ground
RFoF	Radio Frequency over Fiber
RIN	Relative Intensity Noise
RMS	Root Mean Square
RoF	Radio over Fiber
RTO	Real-Time Oscilloscope

## **S**

SFDR	Spurious Free Dynamic Range
SNR	Signal-to-Noise Ratio
SODL	Switchable Optical Delay Line
SOI	Silicon on Insulator
SOLT	Short-Open-Load-Thru
SRF	Self-Resonant Frequency
SSMF	Standard Single Mode Fiber

## **T**

TDD	Time Division Duplexing
TIA	Transimpedance Amplifier
TOI	Third Order Intercept point
TTD	True Time Delay
TWPD	Traveling Wave Photodetector

## **U**

UE	User Equipment
UTC	Uni-Traveling-Carrier

## **V**

VGA	Variable Gain Amplifier
VNA	Vector Network Analyzer
VOA	Variable Optical Attenuator

# Nederlandstalige Samenvatting

## –Dutch Summary–

Mobiele netwerken van de toekomst zullen moeten rekening houden met het exponentieel toenemend dataverkeer. Tegen eind 2013 bedroeg de maandelijkse hoeveelheid draadloos wereldwijd dataverkeer 2 EB (Exabyte, dit wil zeggen  $10^{18}$  bytes). Als we kijken naar het begin van 2019, dan zien we dat het mobiel dataverkeer gestegen is naar 29 EB per maand en dit zal alleen maar groeien in de toekomst. Tegen 2024 wordt 131 EB maandelijks mobiel dataverkeer verwacht en tegen dan zou ongeveer 35% van dit verkeer gebruik moeten maken van het 5G netwerk. De grootste bijdrage van deze stijging in dataverkeer is toe te schrijven aan video gerelateerde toepassingen zoals Youtube en Netflix.

Om tegemoet te komen aan deze vereiste datacapaciteiten, dient een combinatie van verschillende oplossingen gebruikt te worden. Ten eerste is het belangrijk om de communicatiecellen te miniaturiseren. Deze oplossing laat toe om de beschikbare bandbreedte te delen over een beperkter aantal gebruikers waardoor de datacapaciteit per gebruiker stijgt. Ten tweede zal er ook gekeken worden om gebruik te maken van niet-traditionele delen van het frequentiespectrum. In de hoog-frequentere gebieden van het spectrum, bijvoorbeeld bij millimetergolf frequenties, is er meer aansluitende bandbreedte beschikbaar. Daarnaast zijn de laag-frequentere delen ( $< 6$  GHz) van het spectrum typisch ook niet meer vrij beschikbaar door de aanwezigheid van talloze andere draadloze toepassingen. De derde en laatste oplossing die bekeken werd in dit doctoraat is bundelsturing. Bundelsturing is belangrijk om het netwerk vermogen-efficiënt te houden. Bij millimetergolf-frequenties is dit in het bijzonder belangrijk aangezien het verhogen van de draaggolffrequentie tot gevolg heeft dat de kanaalverliezen zullen toenemen.

Het miniaturiseren van de communicatiecellen is een belangrijk onderdeel om uiteindelijk hogere datacapaciteiten te kunnen aanbieden. Echter zal dit ook tot gevolg hebben dat het uitrollen van een dergelijk netwerk veel duurder en complexer wordt. Om dit tegen te gaan is het cruciaal om de hoog-complexe functionaliteit te gaan centraliseren. Bijgevolg zal het signaal voor het downlink-pad (communicatie naar de gebruiker) gegenereerd worden in een hoofdkantoor (*central office*) en zal het signaal voor het uplink-pad (communicatie van de gebruiker) geïnterpreteerd worden in het hoofdkantoor. Optische communicatie volgens het analoge radio-overvezel principe zal dan gebruikt worden om het signaal van het hoofdkantoor naar de gewenste antenne-eenheid (*remote antenna unit*) te brengen en omgekeerd. Dit werk focust zich op de antenne-kant aangezien er veel meer antenne-eenheden vereist zullen zijn dan hoofdkantoren. In de downlink-richting is er nood aan een omzetting van het optisch naar het elektrisch domein en vervolgens een versterking om dan uiteindelijk het signaal draadloos naar de eindgebruiker te versturen. Het uplink signaal start van deze eindgebruiker en zal initieel over het draadloos pad propageren en vervolgens opgevangen worden door de antennes. Dit signaal is zwak en moet dus eerst versterkt worden alvorens het op een optische drager wordt gezet. Finaal keert dit optisch signaal dus terug naar het hoofdkantoor waar de verzonden data geïnterpreteerd wordt.

Hoofdstuk 2 van dit werk richt zich op het omzetten tussen het elektrisch en optisch signaal in de antenne-eenheid. Daarbij zal er vooral gekeken worden naar smalbandige versterking. Traditionele optische zenders en ontvangers maken gebruik van breedbandversterkers. Dit is echter niet de optimale oplossing aangezien mobiele communicatie typisch gebruik maakt van dataverkeer met beperkte relatieve bandbreedte ten opzichte van de gebruikte radiofrequentie.

In een eerste instantie is er in hoofdstuk 2 gebruik gemaakt van een breedband optische ontvanger waarbij een spoel toegevoegd werd aan het ingangsnetwork van de versterker om de gewenste communicatieband te versterken. Vervolgens werd de smalbandige aard van het dataverkeer reeds in rekening gebracht van bij de start van het ontwerpproces. Dit resulteert in een optische ontvanger waarbij een lage-ruis versterker ontworpen in GaAs werd gecombineerd met een fotodetector ontworpen in silicium fotonica. In het laatste deel van hoofdstuk 2, werd de versterker – ontworpen voor de optische ontvanger – aangepast zodat het in combinatie met een reflecterende elektroabsorptie modulator (EAM) kon gebruikt worden

als optische zender voor smalband communicatie. Door de reflectieve werking van de zender kan de laser verplaatst worden van de antenne naar het hoofdkantoor, hetgeen de complexiteit en kost van het netwerk sterk kan reduceren. Zowel de optische zender als ontvanger werden ontworpen voor het gebruik in de 5G banden rond 26 en 28 GHz resulterend in een aaneensluitend frequentie-bereik van 24.25 tot 29.5 GHz.

In hoofdstuk 3 wordt bekeken of de versterking (deels) geïmplementeerd kan worden in het optisch domein. Dit laat eventueel toe om de versterking te centraliseren maar vereist wel hoge-lineariteit fotodetectors. Wanneer meerdere fotodetectors worden gecombineerd, kan het vermogen per fotodetector beperkt worden en op deze manier zal de lineariteit toenemen. Dergelijke oplossingen leiden typisch tot trage fotodetectors. Voor het behouden van de hoge bandbreedte van de detectors zal het belangrijk zijn om de transmissielijn, die de signalen afkomstig van de verschillende fotodetectors terug samenbrengt, correct te dimensioneren. Dergelijke *traveling wave photodetectors* slagen erin hoge lineariteit te combineren met een hoge bandbreedte van de opto-elektronische omzetting. Dit is echter een breedbandige structuur en in het laatste deel van hoofdstuk 3 wordt een smalbandige oplossing bestudeerd waarbij impedantietransformaties gerealiseerd worden op de silicium fotonica chip om optimale vermogenextractie te realiseren. Wanneer de breedband en smalband architecturen vergeleken worden, kan men opmerken dat de smalband oplossing tot compactere en dus goedkopere structuren zal leiden. Bovendien resulteren deze smalband structuren typisch tot een vermogen-efficiëntere opto-elektronische omzetting.

Een laatste functionaliteit die in detail bekeken werd in dit werk (hoofdstuk 4) is bundelsturing. Terwijl de trend voor toekomstige architecturen neigt naar doorgedreven centralisatie, lijkt dit geen oplossing voor bundelsturing. Centralisatie van de bundelsturing resulteert in een radio-over-vezel communicatie die niet langer schaalbaar is. Bijgevolg zal de implementatie van deze functionaliteit bekeken worden aan de kant van de antenne. Optische bundelsturing netwerken zijn hierbij te verkiezen ten opzichte van elektrische varianten door het potentieel tot goedkopere, lichtere, compactere en vermogen-efficiëntere implementaties. Overigens resulteren dergelijke optische bundelsturingsnetwerken in verbeterde resistentie tegen elektromagnetische interferentie. Daarnaast is een dergelijke optische oplossing veel schaalbaarder naar hogere draaggolffrequenties en bijgevolg meer ge-

richt naar toekomstige generaties van mobiele netwerken. In hoofdstuk 4 wordt er eerst gekeken naar een breedband oplossing voor een 4-elementen antenne rooster. Daarnaast is er een beschrijving van een fasesturing implementatie, hetgeen een smalbandige topologie is. Fasesturing steunt op het principe waarbij de draaggolf en data eerst van elkaar worden gescheiden, vervolgens is er een fase draaiing van de draaggolf ten opzichte van de data en finaal combineren we beide terug met elkaar. De scheiding en combinatie van draaggolf en data gebeuren in dit werk met microringen.

Om dit werk af te ronden werden er enkele systeemexperimenten uitgevoerd. Deze worden beschreven in hoofdstuk 5, waarbij er gestart wordt met het karakteriseren van de optische zender en ontvanger voor 5G banden rond 26 en 28 GHz. In het frequentiebereik tussen 24.25 en 29.5 GHz werd op deze manier gemerkt dat zowel de zender als ontvanger kunnen gebruikt worden voor 256-QAM, 400 MBd communicatie. Daarnaast vertonen de optische zender en ontvanger maximale datacapaciteiten van respectievelijk 36 Gb/s en 24 Gb/s. Het laatste deel van hoofdstuk 5 bestudeert het gebruik van de optische ontvanger en zender in een smalbandige bidirectionele antenne-eenheid. De ontvanger-zender combinatie laat toe om lage-kost, lage-complexiteit antenne-eenheden te gaan uitrollen om op deze manier een schaalbare radio-over-vezel architectuur te gaan implementeren en zo een centralisatie en miniaturisatie van het netwerk toe te laten. De ontvanger-zender combinatie verbruikt slechts 427 mW en laat toe om 7 Gb/s downlink en uplink te verzenden over 2km vezel en 5m draadloos met een EVM van ongeveer 10%. Wanneer 2m draadloos volstaat, laat de EVM zelfs 64-QAM toe en zo kan er 10.53 Gb/s downlink en uplink verzonden worden.

## English Summary

Future wireless communication will require increasingly higher data capacities. At the end of 2013 the global wireless data traffic accounted for 2 EB (Exabyte, i.e.  $10^{18}$  bytes) per month and by the start of 2019 this has already increased to 29 EB per month. The total mobile data traffic is expected to keep on growing fast and reach 131 EB per month by the end of 2024 and by then 5G should carry around 35% of it. The main contribution to this exponential increase in mobile data traffic can be attributed to video related applications like Youtube and Netflix.

To meet these ever increasing demands in wireless data rates, a combination of a multitude of solutions is envisioned. A first important evolution is the densification of the cellular network. By shrinking the cell sizes, resources are shared among fewer users and hence the data capacity per user is increased. Secondly, future wireless networks envision the usage of higher-frequency parts of spectrum, typically mmWave frequencies. These higher-frequency ranges offer much wider (consecutive) bandwidth and are significantly less congested than the sub-6 GHz band. A final part of the solution to enable higher throughput communication that is looked at in this work consists of beamforming. Beamforming not only helps to improve the power efficiency of the network but also helps to overcome the high path losses present in the wireless channel at mmWave frequencies.

While the densification of the mobile network helps to get higher wireless data capacity, it also heavily increases deployment costs. To counter this, centralization of the high-complexity functionality is key. Consequently, the downlink (communication to the user) and uplink (communication from the user) RF signal will respectively be generated and interpreted at the central office. Optical communication, based on the Analog Radio or mmWave-over-Fiber principle, is adopted to perform the signal distribution between central office and remote antenna units. At the antenna side, the downlink signal needs to be converted to the electrical domain and subsequently amplified before passing the signal to the wireless channel and

eventually the user. The data generated at the user side first passes via the wireless link before the signal is received by the antenna. Subsequently, the signal is amplified and put on an optical carrier before traveling back through the optical fiber to the central office.

In chapter 2 of this work, the detection and modulation functionality at the opto-electrical interface of the antenna is discussed with particular focus on the narrowband electrical amplification. Typical optical communication schemes rely on broadband devices to perform this amplification functionality while data formats in mobile communication schemes use limited relative bandwidth. Therefore a broadband device was initially reused and optimized for narrowband operation. The principle used in that device is the addition of series inductive peaking at the input of a broadband transimpedance amplifier to enhance the gain for the desired frequency band. Next, a Si photonics / GaAs electronics photoreceiver was designed combining the opto-electrical conversion functionality performed by a photodetector and narrowband amplification by a dedicated low noise amplifier. The final part of chapter 2 focuses on the design of the driver and modulator for the uplink communication. A reflective EAM was devised to allow for laser-less operation in the active antenna units resulting in a further reduction in the complexity and cost of the network. The driver used to amplify the incoming wireless signal before feeding it to the reflective modulator is based on the amplifier design in the photoreceiver. The detection and modulation building blocks in the active antenna unit are designed to operate in the same spectral band, namely the new radio channels spanning from 24.25 to 29.5 GHz band.

Chapter 3 of this dissertation discusses the design of the high-linearity photodetectors required to (partially) shift the amplification functionality to the optical domain. The first step is the design of a broadband device, namely a traveling wave photodetector combining a photodetector array with transmission lines to get a high-bandwidth, high-linearity detector. Subsequently, a narrowband solution is devised by designing LC matching networks on the photonic chip to get optimal power transfer to the output at a given frequency. This allows for a size reduction in the high-linearity photodetector topology and typically results in a more efficient detector.

The last functionality that is looked at is the beamforming capability of the active antenna unit (chapter 4). Centralizing beamforming capabili-

ties tends to be unscalable and the beamforming functionality should therefore be located at the antenna side. Optical beamforming networks are considered since they offer improved immunity to electromagnetic interference and promise cost, weight, size and power consumption reductions compared to their electrical counterparts. Furthermore, optical solutions are more futureproof to deal with the tendency to increasing carrier frequencies in subsequent generations of mobile networks. As with the high linearity detectors, broadband topologies are first covered and a true time delay beamforming network is designed to offer beamforming functionality for a 4-element antenna array. Eventually, narrowband phase steering is discussed targeting mmWave narrowband communication. The optical RF phase steering principle consists of separating carrier and data, adjusting the phase of the carrier and finally recombining carrier and data components. Finally, a proof-of-principle is devised for a 4-element antenna array where the required separation and combination functionality is performed by microring resonators.

To conclude this work, data transmission experiments were performed as described in chapter 5. Both the transmitter and receiver were tested in the new radio bands spanning the 24.25 to 29.5 GHz spectrum resulting in signal quality levels good enough to transmit 256-QAM, 400 MBd radio signals. The photoreceiver and EAM-driver are also tested for high-data rate links resulting in data capacities of respectively 36 Gb/s and 24 Gb/s. The final part of chapter 5 addresses the GaAs electronics/Si photonics bidirectional narrowband transceiver chipset based on the components described in chapter 2. The transceiver chipset enables low-cost, low-complexity remote antenna units for scalable RFoF architectures and consumes only 427 mW. With this transceiver, over 7 Gb/s downlink and uplink were demonstrated for a 2km fiber — 5m wireless mmWave link with an EVM around 10%. For 2km fiber — 1m wireless, the measured EVMs can even support 64-QAM, resulting in a potential aggregated capacity of 10.53 Gb/s for downlink and uplink.



# List of Publications

## Publications in International Journals

- **L. Bogaert**, H. Li, K. Van Gasse, J. Van Kerrebrouck, J. Bauwelinck, G. Roelkens, and G. Torfs, *36 Gb/s Narrowband Photoreceiver for mmWave Analog Radio-over-Fiber*, Journal of Lightwave Technology, vol. 38, no. 12, pp. 3289-3295, June 2020.
- **L. Bogaert**, K. Van Gasse, T. Spuesens, G. Torfs, J. Bauwelinck, and G. Roelkens, *Silicon Photonics Traveling Wave Photodiode with Integrated Star Coupler for High-Linearity mmWave Applications*, Optics Express, vol. 26, no. 26, pp. 34753-34765, December 2018.
- **L. Bogaert**, J. Van Kerrebrouck, A. Abbasi, J. Lambrecht, G. Torfs, X. Yin, G. Roelkens, and J. Bauwelinck, *Resonant Optical Receiver Design by Series Inductive Peaking for sub-6 GHz RoF*, Microwave and Optical Technology Letters, vol. 59, no. 9, pp.2279-2284, June 2017.
- K. Van Gasse, **L. Bogaert**, L. Breyne, J. Van Kerrebrouck, S. Dhoore, C. Op de Beeck, A. Katumba, C.Y. Wu, H. Li, J. Verbist, A. Rahim, A. Abbasi, B. Moeneclaey, Z. Wang, H. Chen, J. Van Campenhout, X. Yin, B. Kuyken, G. Morthier, J. Bauwelinck, G. Torfs, and G. Roelkens, *Analog Radio-over-Fiber Transceivers Based on III-V-on-Silicon Photonics [Invited]*, IEEE Photonics Technology Letters, vol. 30, no. 21, pp. 1818-1821, November 2018.
- O. Caytan, **L. Bogaert**, H. Li, J. Van Kerrebrouck, S. Lemey, G. Torfs, J. Bauwelinck, P. Demeester, S. Agneessens, D. Vande Ginste, and H. Rogier, *Passive Opto-Antenna as Downlink Remote Antenna Unit for Radio Frequency Over Fiber*, Journal of Lightwave Technology, vol. 36, no. 19, pp. 4445-4459, October 2018.

- O. Caytan, **L. Bogaert**, H. Li, J. Van Kerrebrouck, S. Lemey, S. Agneessens, J. Bauwelinck, P. Demeester, G. Torfs, D. Vande Ginste, and H. Rogier, *Compact and Wideband Transmit Opto-Antenna for Radio Frequency over Fiber*, Optics Express, vol. 27, no. 6, pp. 8395-8413, March 2019.
- H. Li, M. Verplaetse, J. Verbist, J. Van Kerrebrouck, L. Breyne, C.-Y. Wu, **L. Bogaert**, B. Moeneclaey, X. Yin, J. Bauwelinck, P. Demeester, and G. Torfs, *Real-Time 100-GS/s Sigma-Delta Modulator for All-Digital Radio-over-Fiber Transmission [Invited]*, Journal of Lightwave Technology, vol. 38, no. 2, pp. 386-393, January 2020.
- Q. Van den Brande, S. Lemey, S. Cuyvers, S. Poelman, L. De Brabander, O. Caytan, **L. Bogaert**, I. Lima De Paula, S. Verstuyft, A. C. F. Reniers, B. Smolders, B. Kuyken, D. Vande Ginste, and H. Rogier, *A Hybrid Integration Strategy for Compact, Broadband and Highly Efficient Millimeter-Wave On-Chip Antennas*, IEEE Antennas and Wireless Propagation Letters, vol. 18, no. 11, pp. 2424-2428, November 2019.

## Publications in International Conferences

- **L. Bogaert**, J. Van Kerrebrouck, H. Li, I. L. De Paula, K. Van Gasse, S. Lemey, H. Rogier, P. Demeester, G. Roelkens, J. Bauwelinck, and G. Torfs, *SiPhotonics/GaAs 28-GHz Transceiver for mmWave-over-Fiber Laser-Less Active Antenna Units [Postdeadline Paper]*, 2020 Optical Fiber Communication Conference and Exhibition (OFC 2020), San Diego, United States of America, March 2020.
- **L. Bogaert**, H. Li, K. Van Gasse, J. Van Kerrebrouck, J. Bauwelinck, G. Roelkens, and G. Torfs, *Narrowband Photoreceiver for Analog Radio-over-Fiber in the 24.25-29.5 GHz Band*, 45th European Conference on Optical Communication (ECOC 2019), Dublin, Ireland, September 2019.
- **L. Bogaert**, J. Verbist, K. Van Gasse, G. Torfs, J. Bauwelinck, and G. Roelkens, *Germanium Photodetector with Monolithically Integrated Narrowband Matching Network on a Silicon Photonics Platform*, 21st European Conference on Integrated Optics (ECIO 2019), Ghent, Belgium, April 2019.

- **L. Bogaert**, K. Van Gasse, G. Torfs, J. Bauwelinck, and G. Roelkens, *High-Power Traveling Wave Photodetector in Silicon Photonics with Monolithically Integrated Optical Power Splitter*, 22nd Annual Symposium of the IEEE Photonics Society Benelux Chapter, Delft, Netherlands, November 2017.
- O. Caytan, **L. Bogaert**, G. Torfs, J. Bauwelinck, P. Demeester, D. Vande Ginste, S. Lemey, and H. Rogier, *Air-Filled Substrate-Integrated-Waveguide Cavity-Backed Slot Antenna with Optical Feeding*, 2nd URSI Atlantic Radio Science Conference (URSI AT-RASC 2018), Gran Canaria, Spain, May 2018.
- O. Caytan, **L. Bogaert**, H. Li, J. Van Kerrebrouck, S. Lemey, J. Bauwelinck, P. Demeester, G. Torfs, D. Vande Ginste, and H. Rogier, *Passive Opto-Antenna using Air-Filled Substrate-Integrated-Waveguide Technology*, 23rd IEEE Workshop on Signal and Power Integrity, Chambéry, France, June 2019.
- J. Van Kerrebrouck, **L. Bogaert**, H. Li, C.-Y. Wu, P. Demeester, G. Roelkens and G. Torfs, *Monolithically Integrated Quadrature EAM Structure for 28 GHz Full Duplex Radio over Fiber*, 24th Annual Symposium of the IEEE Photonics Society Benelux Chapter, Amsterdam, Netherlands, November 2019.
- H. Li, O. Caytan, J. Van Kerrebrouck, **L. Bogaert**, C.-Y. Wu, L. Breyne, J. Bauwelinck, H. Rogier, P. Demeester, and G. Torfs, *Sigma-Delta Radio-over-Fiber with Passive Opto-Antenna for Low-Power Short-Reach Optical-Wireless Downlink*, 23rd Annual Symposium of the IEEE Photonics Society Benelux Chapter, Brussels, Belgium, November 2018.
- H. Li, J. Van Kerrebrouck, H. Ramon, **L. Bogaert**, J. Lambrecht, C.-Y. Wu, L. Breyne, J. Declercq, J. Bauwelinck, X. Yin, P. Ossieur, P. Demeester, and G. Torfs, *Low Power All-Digital Radio-over-Fiber Transmission for 28-GHz Band using Parallel Electro-Absorption Modulators*, 2020 Optical Fiber Communication Conference and Exhibition (OFC 2020), San Diego, United States of America, March 2020.

- C.-Y. Wu, H. Li, J. Van Kerrebrouck, L. Breyne, **L. Bogaert**, P. Demeester, and G. Torfs, *Real-time 4x3.5 Gbps Sigma Delta Radio-over-Fiber for a Low-Cost 5G C-RAN Downlink*, 44th European Conference on Optical Communication (ECOC 2018), Rome, Italy, September 2018.
- J. Lambrecht, J. Verbist, H. Ramon, M. Vanhoecke, B. Moeneclaey, **L. Bogaert**, P. Ossieur, J. Van Campenhout, J. Bauwelinck, G. Roelkens, and X. Yin, *53 GBd PAM-4 DAC-Less Low-Power (1.5 pJ/b) Silicon Integrated Transmitter*, 45th European Conference on Optical Communication (ECOC 2019), Dublin, Ireland, September 2019.
- H. Li, M. Verplaetse, J. Verbist, J. Van Kerrebrouck, L. Breyne, C.-Y. Wu, **L. Bogaert**, X. Yin, J. Bauwelinck, P. Demeester, and G. Torfs, *Real-Time 100-GS/s Sigma-Delta All-Digital Radio-over-Fiber Transmitter for 22.75-27.5 GHz Band*, 2019 Optical Fiber Communication Conference and Exhibition (OFC 2019), San Diego, United States of America, March 2019.
- J. Bauwelinck, P. Ossieur, G. Roelkens, M. Vanhoecke, J. Lambrecht, H. Ramon, L. Breyne, C. Bruynsteen, **L. Bogaert**, J. Van Kerrebrouck, M. Verplaetse, G. Torfs, B. Moeneclaey, J. Van Campenhout, and X. Yin, *High-speed electronics for silicon photonics transceivers [Invited]*, SPIE Photonics Europe – Integrated Photonics Platforms: Fundamental Research, Manufacturing and applications, Strasbourg, France, March 2020.

## Publications in National Conferences

- **L. Bogaert**, *Electro-Optic Co-Design for Radio-over-Fiber 5G Applications: Beamforming and Amplification*, 19th FEA research symposium (FEARS 2019), February 19, 2019, Ghent, Belgium

# 1

## Introduction

### 1.1 Evolution of Wireless Communication

The past decades, the mobile communication infrastructure has undergone huge advancements [1, 2]. In the early 1980s, the first generation cellular network was introduced and offered wireless analog voice communication. About a decade later, a second generation introduced digital communication standards. This allowed for the advent of Short Message Service (SMS) and basic internet services. In 2003, a third generation cellular network saw the light of day and mobile broadband data became important. In 2009, 4G was introduced and it focused mainly on achieving true mobile broadband resulting in data rates two orders of magnitude larger than what 3G offered. Another decade later, and we are on the verge of taking another leap forward with the introduction of the fifth generation cellular network (5G).

For the 5G cellular network, multiple usage scenarios are envisioned as shown in Fig. 1.1:

1. **Enhanced Mobile Broadband - eMBB:** This usage scenario deals with the ever increasing demand for higher wireless data rates, even

under though circumstances including high user mobility and large user density. – e.g. *Gbps internet, Virtual/Augmented Reality, 4K/3D video*

2. **Ultra-Reliable, Low Latency Communication - uRLLC:** Ultra high reliability should be combined with low latency to get always-available, quasi-immediate operation for deployment in critical applications. – e.g. *Autonomous driving, Telesurgery, Industry 4.0*
3. **Massive Machine Type Communications - mMTC:** Massive Internet of Things (IoT) deployment is the targeted application in this usage scenario. The network should be able to cope with a huge connection density while offering very low device cost and power consumption. Throughput and latency are typically less critical in these mMTC environments. – e.g. *Smart city, Smart home*

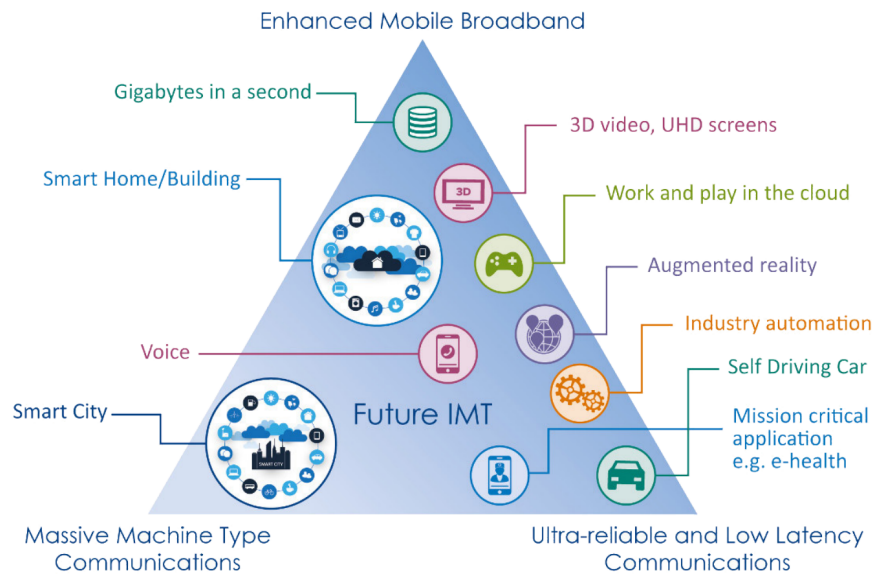


Figure 1.1: Usage scenarios of 5G [3, 4].

This dissertation is aimed at the eMBB use cases and this will therefore be described in more detail below. First the requirements for eMBB systems will be discussed and subsequently some of the methods used to achieve those high data rates will be covered.

The study provided by Ericsson in their mobility report [5] shows a steep increase of the total global mobile data over the past few years and the years to come (Fig. 1.2). At the end of 2013 the global wireless data traffic accounted for 2 EB (Exabyte, i.e.  $10^{18}$  bytes) per month and by the start of 2019 this has already increased to 29 EB per month. The total mobile data traffic is expected to keep on growing fast and reach 131 EB per month by the end of 2024 and by then 5G should carry around 35% of it. This is on the one hand caused by the increasing number of mobile users as the number of mobile subscriptions is expected to grow from 6 billion (2018) to 8.3 billion (2024). On the other hand, one can also expect the data usage per user to increase significantly. The main contributor is mobile video traffic, already accounting for 60% of the total mobile data traffic in 2018 (Fig. 1.3). By 2024, mobile video traffic should be responsible for about 74% of the total mobile data traffic.

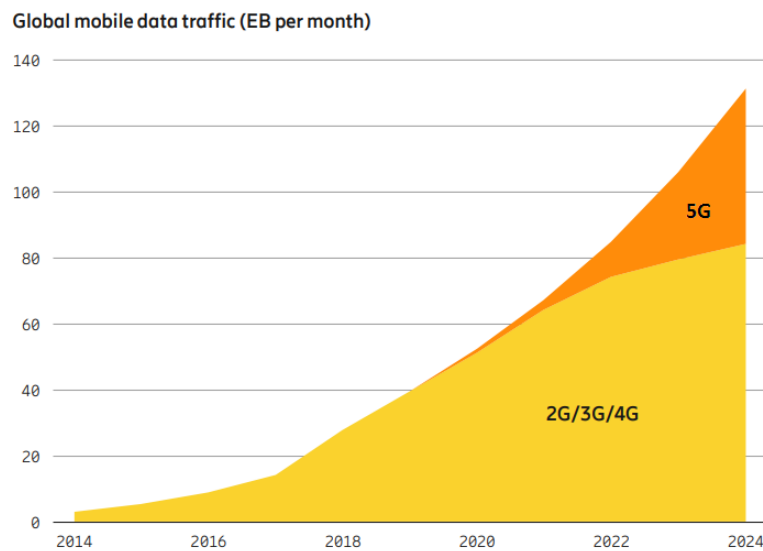


Figure 1.2: Global mobile data traffic 2014-2024 [5].

Before taking a look at how the infrastructure should change to meet these demands for mobile broadband, the expected performance requirements will be covered. As discussed before, 5G has to deal with different usage scenarios that focus on different subsets of criteria (e.g. mMTC typically does not require very high throughput and eMBB allows for a higher latency than uRLLC). The 5G requirements for eMBB systems are provided in table 1.1. In this table, downlink (DL) denotes the communication to-

wards the user while uplink (UL) denotes the communication originating from the user. The user experienced data rate describes the minimal expected data rate for 95% of the users in a dense urban test environment.

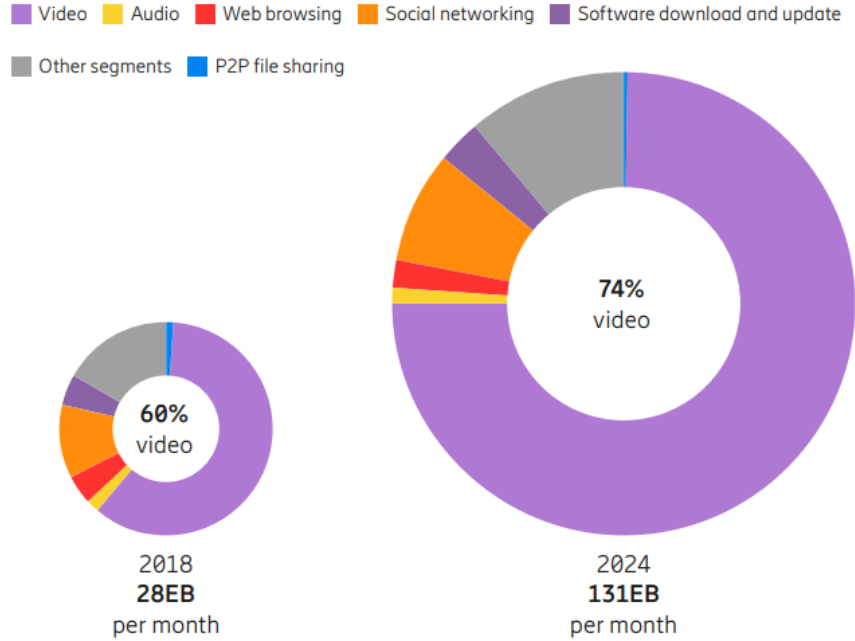


Figure 1.3: Mobile data traffic per application [5].

Performance criterium	Requirement
<b>Peak data rate</b>	> 20/10 Gbps (DL/UL)
<b>Peak spectral efficiency</b>	> 30/15 bps/Hz (DL/UL)
<b>User experienced data rate</b>	> 100/50 Mbps (DL/UL)
<b>Area traffic capacity</b>	> 10 Mbps/m <sup>2</sup> (indoor)
<b>User plane latency</b>	< 4 ms
<b>Control plane latency</b>	< 20 ms but preferably < 10 ms
<b>Mobility</b>	up to 500 km/h (rural)

Table 1.1: 5G Requirements for the eMBB usage scenario [6] – DL: Downlink; UL: Uplink.

Aiming for these specifications requires the implementation of a mix of different technologies, including but not limited to [7–9]:

1. **Small Cells:** A straightforward technique to improve the overall capacity of the network concerns densification. Reducing communication cell sizes allows the cell resources to be shared among fewer users. Additionally, this helps to lower the power consumption by lowering the average wireless distance which needs to be bridged. To keep this technique economically viable, however, low-cost cells are paramount.
2. **Millimeter Wave (mmWave):** Data rates can be improved by shifting towards higher frequencies, e.g. the mmWave range. These higher-frequency ranges offer much wider (consecutive) bandwidth and are significantly less congested than the sub-6 GHz band. The shift to mmWave enables the usage of antenna arrays because of the scaling of the individual elements to smaller dimensions. This scaling effect facilitates the implementation of massive Multiple Input, Multiple Output (MIMO) and beamforming for mmWave applications. Figure 1.4 provides a summary of the priority frequency bands for 5G per region and shows major interest for the 26/28 GHz bands. Tight integration of these new radio-access (NR) technologies with the existing sub-6 GHz bands remains key for improved coverage.

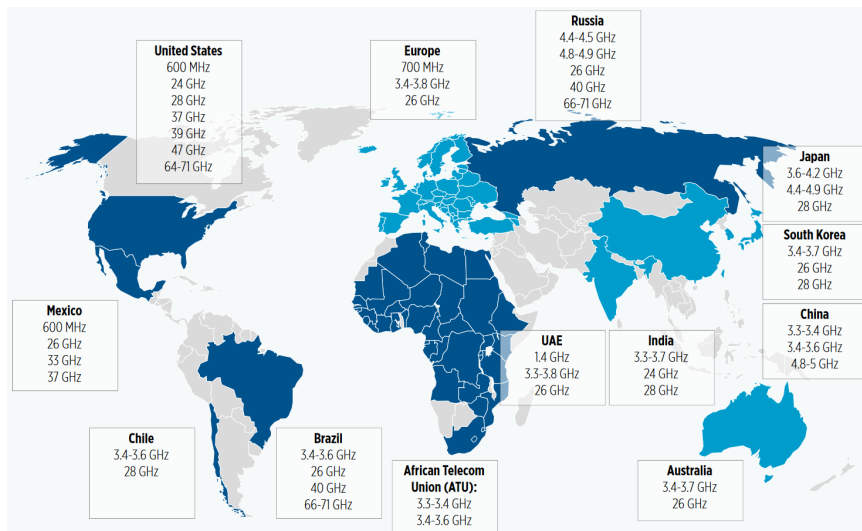


Figure 1.4: Priority frequency bands for 5G [10].

3. **Full Duplex:** Nowadays, typical communication schemes do not work in the same time-frequency resource block. Frequency Division

Duplexing (FDD) and Time Division Duplexing (TDD) respectively use different frequency bands or time slots for up- and downlink. In true full duplex operation the total spectral efficiency is heavily boosted by sending up- and downlink signals simultaneously in the same frequency band.

4. **Beamforming:** Communication by means of mmWave frequencies introduces increased path losses. Beamforming will be critical to improve energy efficiency by focusing the transmitted energy in the desired direction rather than having omnidirectional transmission. An added advantage is the reduction in interference allowing for spatial multiplexing of communication channels which significantly increases the system capacity.
5. **Massive MIMO:** Multi-user MIMO is used in 4G cellular networks. Massive MIMO is an extension of the MIMO technology to a much larger number of antennas. This is made possible by the miniaturization of the antenna elements due to the shift towards higher frequencies. MIMO can be used to boost the spectral efficiency by allowing multiple users to communicate in the same frequency-time resource block. Alternatively, MIMO can help to improve reliability by implementing transmit diversity. In such a transmit diversity scheme, two or more antennas transmit identical information to reduce fading effects in the wireless channel and consequently diminish the reduction of signal quality in the wireless channel.

## 1.2 Radio over Fiber

Densification of the cellular network will be one of the key enablers for enhanced mobile broadband. Miniaturization of the communication cells results in a huge increase in the required number of access point. To make such a densification of the network economically viable, centralized approaches are of paramount importance. Radio over Fiber (RoF) has been proposed as a possible transmission scheme to push most of the complexity to a Central Office (CO) that is being shared by multiple Remote Antenna Units (RAUs) as can be seen in Fig. 1.5 [11, 12]. The communication between the CO and the RAUs is based on optical fiber communication and when the signal arrives at the intended RAU, the signal is translated back to the electrical domain and transmitted over the wireless channel to the end users.

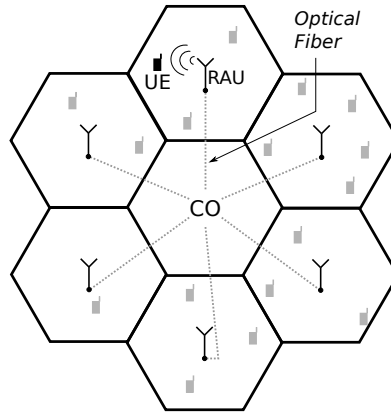


Figure 1.5: Centralized architecture with RoF fronthaul – RAU: Remote Antenna Unit; CO: Central Office; UE: User Equipment.

Potential implementations (Fig. 1.6) of the RoF scheme can be classified as [13, 14]:

1. **Digital Radio over Fiber (DRoF):** In a DRoF scheme, discrete power levels are transmitted over the optical fiber between CO and RAU. This offers reduced sensitivity to noise and non-linearities in the link. DRoF technologies, such as the Common Public Radio Interface (CPRI) [15], are commonly used in 4G Radio Access Networks (RANs). However, it results in complex, power-hungry RAUs and is therefore not scalable in terms of RAU density.
2. **Analog Radio over Fiber (ARoF):** DRoF schemes rely on the construction of the RF signal at the RAUs. In an ARoF architecture, the generation of the RF signal is moved to the CO. Hereby it enables the low-complexity, low-cost RAUs that are required to make small cell communication networks viable. The main challenge in an ARoF link is the high sensitivity of the performance to noise and non-linearities in the link.
3. **Sigma-Delta over Fiber (SDoF):** SDoF introduces a technique that uses oversampling at the CO and bandpass filtering at the RAU to benefit from the advantages of both digitized and analog RoF. Combining SDoF with digital up-conversion [16] results in low-complexity power-efficient RAUs while providing reduced sensitivity to noise and non-linearities. The main drawback of the SDoF implementation style is that it requires large oversampling rate sigma-delta modula-

tors to achieve high SNR. Furthermore, the ARoF allows for a more straightforward implementation of the uplink path in the RAU.

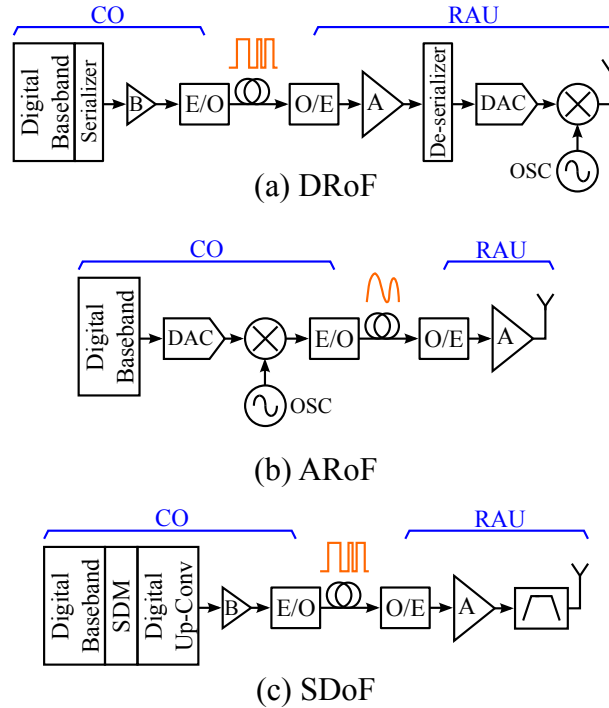


Figure 1.6: RoF implementation types: (a) Digitized Radio-over-Fiber (DRoF), (b) Analog Radio-over-Fiber (ARoF) and (c) Sigma-Delta modulated signal over Fiber (SDoF) – E/O: Electrical-to-Optical; O/E: Optical-to-Electrical; B: Binary Driver; A: Amplifier; DAC: Digital-to-Analog Converter; OSC: Oscillator; SDM: Sigma Delta Modulator [14].

### 1.3 Microwave Silicon Photonics

Microwave Photonics (MWP) is the domain that combines RF engineering and optoelectronics [17–21]. In a MWP link, optical components are used to implement some of the functionality required for microwave systems: the generation, processing, distribution and reception of microwave and mmWave signals (Fig. 1.7). Examples of RF functions that can be implemented in the optical domain include but are not limited to filtering, beamforming and analog-to-digital conversion.

Key benefits of this approach include low and frequency-independent loss, high processing bandwidth, immunity to electromagnetic interference, large reconfigurability, etc. Furthermore, MWP can provide functionality that is hard or even impossible to realize in the radio frequency domain. Nowadays, MWP systems typically make use of discrete optoelectronic devices resulting in bulky, expensive, power-hungry solutions. By integrating this MWP functionality on a chip, the overall cost, power consumption and size of the MWP system is heavily reduced and the reliability is improved.

The main drawbacks of pushing microwave functionality from the RF to the optical domain are the added loss, noise and distortion introduced by the required E/O and O/E conversion. However, as we will make use of a RoF scheme, these conversions are already present and therefore these drawbacks are less important in the choice of where the microwave functionality should be implemented.

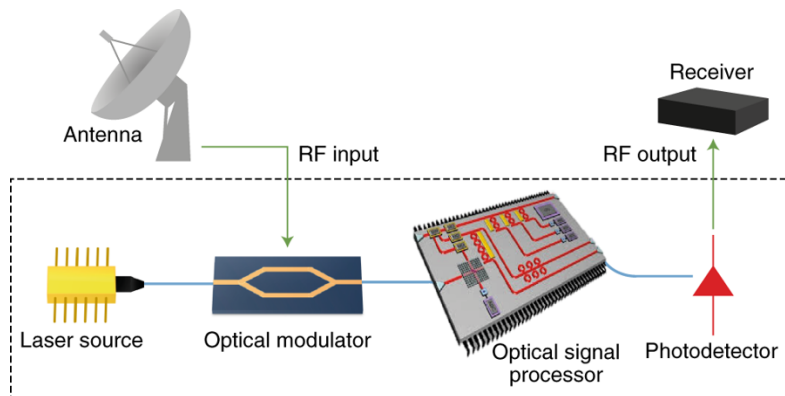


Figure 1.7: Microwave photonic link [21].

A multitude of material systems are available to implement the microwave functionalities on-chip: Silicon on Insulator (SOI), InP,  $\text{Si}_3\text{N}_4$ ,  $\text{LiNbO}_3$ , etc. Silicon photonics is a Complementary Metal-Oxide-Semiconductor (CMOS) compatible silicon-oriented technology [22, 23] and consequently leverages the years of effort put in the microelectronic industry and its available infrastructure. This allows for complex, high yield, low cost devices in large quantity. The silicon photonics technology platform relies on an SOI stack which offers a large index contrast to the photonic devices meaning that highly compact Photonic Integrated Circuits (PICs) can be made. Unfortunately, this large index contrast also results in relatively high scattering losses in the waveguide (typically 1 to 2 dB per cm) and the sidewall

roughness should be controlled tightly to prevent even more loss. Another important drawback of the silicon photonics platform is the absence of an efficient light source since silicon is an indirect bandgap material.

Finally, it should be noted that the choice for CMOS compatible photonic IC design allows for true monolithic co-integration of optical and electrical functionality. Key benefits of such an approach include easier packaging, improved reliability and reduced parasitics allowing for operation at higher speeds. An example of such a zero-change implementation in 32 and 45nm SOI CMOS is described in [24].

## 1.4 Outline of Dissertation

This dissertation covers the implementation of amplification and beam-forming functionalities for narrowband millimeter wave telecom applications in an ARoF fronthaul network. This work mainly focuses on optimizing the RAU where cost, power consumption and complexity will be key since the envisioned centralized, small cell approach will result in a vast amount of RAUs being served by a limited number of COs.

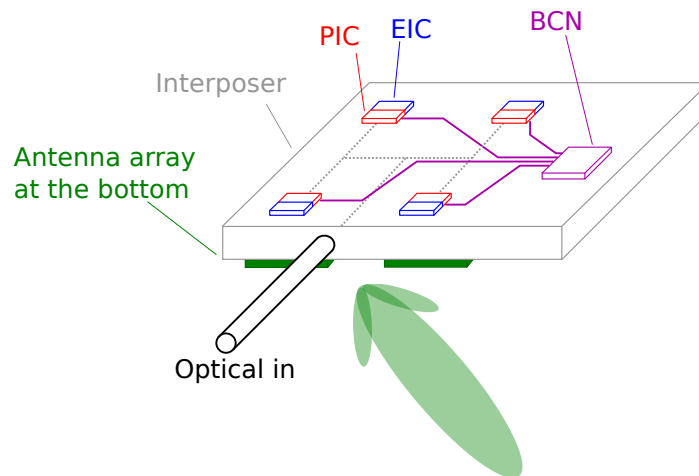


Figure 1.8: Remote antenna unit for a 2x2 antenna array – BCN: Beamforming Control Network; EIC: Electronic Integrated Circuit; PIC: Photonic Integrated Circuit.

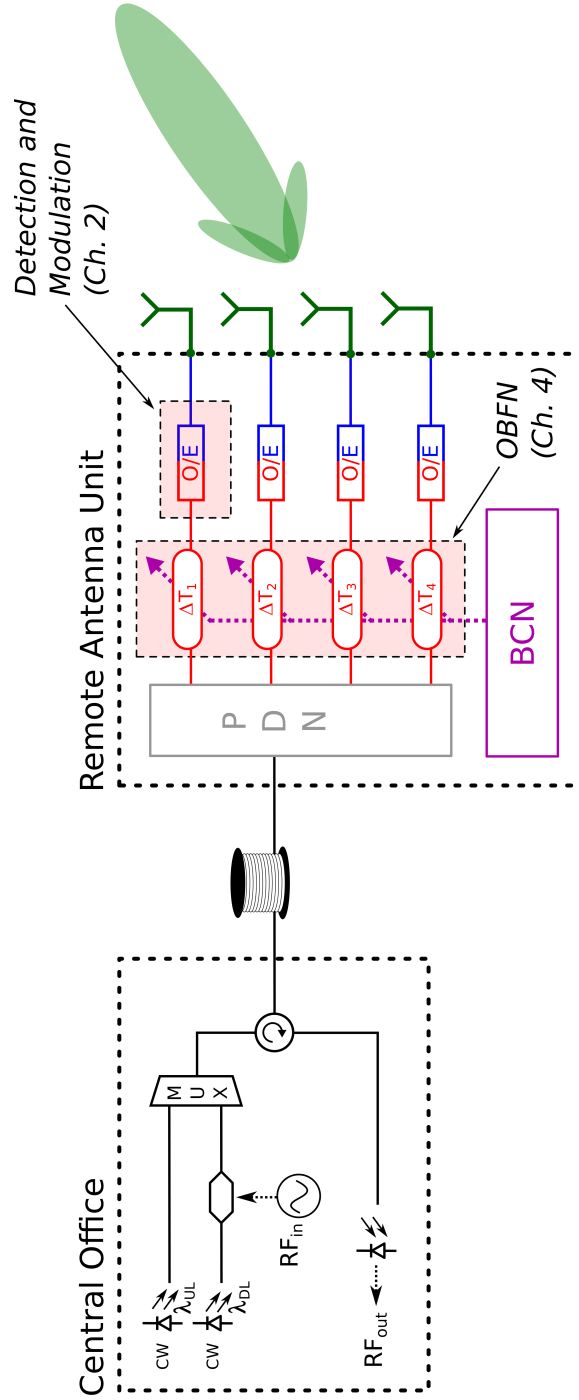


Figure 1.9: System architecture – CW: Continuous Wave; UL: Uplink; DL: Downlink; MUX: Multiplexer; PDN: Power Distribution Network; OBFN: Optical Beamforming Network.

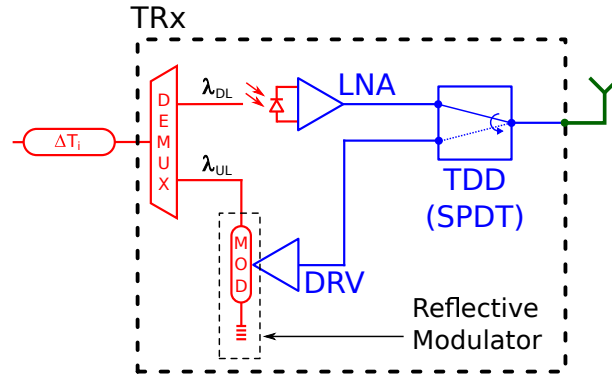


Figure 1.10: Antenna element – TRx: Transceiver; MOD: Modulator; LNA: Low Noise Amplifier; DRV: Driver; TDD: Time Division Duplexing; SPDT: Single Pole Double Throw switch.

A 3D overview of such a RAU is depicted in Fig. 1.8. An optical fiber (or fiber array) connects the RAU with the CO. When the signal arrives at the RAU, an interposer distributes the optical signal to the individual antenna elements. Subsequently, basic optical and electrical functionalities will be performed by the PIC and Electronic Integrated Circuit (EIC) respectively. In Fig. 1.8, a microcontroller is added to correctly set the beamforming parameters. Following the signal processing functionalities performed in the PIC and EIC, i.e. beamforming and amplification, the signal is passed on to the antennas and subsequently the wireless channel. The antenna array can for example be implemented on the backside of the interposer.

A more detailed schematic describing the different building blocks required for up- and downlink operation is shown in Fig. 1.9. Figure 1.10 shows the subcircuit describing the individual antenna elements that consist of two major parts: the beamforming functionality and the O/E conversion.

Chapter 2 explains the transceiver in Fig. 1.10. It starts by providing a power budget calculation and then discusses the benefits and challenges when adopting narrowband amplification schemes. Traditional optical receiver architectures rely on broadband Transimpedance Amplifiers (TIAs). Two techniques will be covered to enhance the photoreceivers for narrowband applications. Firstly, broadband TIAs can be boosted in a frequency band of interest by adopting series inductive peaking at the input of the TIA. Secondly, a photoreceiver concept will be discussed that takes the narrowband nature of the signal already into account during the design phase. To conclude chapter 2, a reflective modulator is discussed for the uplink path.

When the photodetector at the RAU does not offer sufficient linearity, for example to introduce centralized optical amplification, high linearity O/E conversion techniques should be considered (Chapter 3). Firstly, a Traveling Wave Photodetector (TWPD) will be described. This is a device that combines photocurrent from multiple photodetectors in a detector-array to construct a high-power, high-bandwidth photodetector. At the end of chapter 3, this technique will be compared with on-PIC LC matching of a photodetector-array which is a more narrowband approach.

Chapter 4 covers optical beamforming networks and discusses two potential implementations. First, True Time Delay (TTD) will be looked at, offering broadband beam steering. A second implementation that will be discussed relies on phase steering and offers a narrowband beamforming solution. Chapter 4 also discusses what the advantages and disadvantages of optical beamforming networks are compared to electrical schemes and why analog beamforming at the RAU is desired over centralized digital beamforming.

After discussing the main building blocks for amplification and beamforming in chapters 2,3 and 4 the focus in chapter 5 will be shifted to data transmission experiments using these previously developed devices. A conclusion of this dissertation and possible future work is subsequently provided in chapter 6.



## References

- [1] A. Gupta and R. K. Jha, “A Survey of 5G Network: Architecture and Emerging Technologies,” *IEEE Access*, vol. 3, pp. 1206–1232, July 2015.
- [2] Qualcomm, “The Evolution of Mobile Technologies,” June 2014. [Online]. Available: <https://www.qualcomm.com/media/documents/files/download-the-evolution-of-mobile-technologies-1g-to-2g-to-3g-to-4g-lte-qualcomm.pdf>
- [3] *Setting the Scene for 5G: Opportunities & Challenges*, ITU-R, 2018.
- [4] *IMT Vision – Framework and overall objectives of the future development of IMT for 2020 and beyond (M.2083-0)*, ITU-R, September 2015.
- [5] *Ericsson Mobility Report*, Ericsson, June 2019.
- [6] *Minimum requirements related to technical performance for IMT-2020 radio interface(s) (M.241-0)*, ITU-R, November 2018.
- [7] E. Dahlman (Ericsson), “5G: Wireless access of the future,” in *Optical Fiber Communications Conference and Exhibition (OFC)*, March 2017, th3A.1.
- [8] I. F. Akyildiz, S. Nie, S.-C. Lin, and M. Chandrasekaran, “5G roadmap: 10 key enabling technologies,” *Computer Networks*, vol. 106, pp. 17–48, September 2016.
- [9] J. G. Andrews, S. Buzzi, W. Choi, S. V. Hanly, A. Lozano, A. C. K. Soong, and J. C. Zhang, “What Will 5G Be?” *IEEE Journal on Selected Areas in Communications*, vol. 32, no. 6, pp. 1065–1082, June 2014.
- [10] *The WRC series: Study on Socio-Economic Benefits of 5G Services Provided in mmWave Bands*, GSMA, December 2018.

- 
- [11] V. A. Thomas, M. El-Hajjar, and L. Hanzo, “Performance Improvement and Cost Reduction Techniques for Radio Over Fiber Communications,” *IEEE Communication Surveys & Tutorials*, vol. 17, no. 2, pp. 627–670, Second Quarter 2015.
- [12] T. Kawanishi, A. Kanno, and H. Freire, “Wired and Wireless Links to Bridge Networks,” *IEEE Microwave Magazine*, vol. 19, no. 3, pp. 102–111, April 2018.
- [13] H. Li, “Wireless and Radio-over-Fiber Technologies for 5G Communication Systems,” Ph.D. dissertation, Ghent University, 2019.
- [14] C.-Y. Wu, H. Li, O. Caytan, J. Van Kerrebrouck, L. Breyne, J. Bauwelinck, P. Demeester, and G. Torfs, “Distributed Multi-User MIMO Transmission Using Real-Time Sigma-Delta-over-Fiber for Next Generation Fronthaul Interface,” *Journal of Lightwave Technology*, vol. 38, no. 4, pp. 705–713, February 2020.
- [15] “Common Public Radio Interface,” Accessed: August 2019. [Online]. Available: <http://www.cpri.info>
- [16] A. Frappé, A. Flament, B. Stefanelli, A. Kaiser, and A. Cathelin, “An All-Digital RF Signal Generator Using High-Speed  $\Delta\Sigma$  Modulators,” *IEEE Journal of Solid-State Circuits*, vol. 44, no. 10, pp. 2722–2732, October 2009.
- [17] J. Yao, “Microwave Photonics,” *Journal of Lightwave Technology*, vol. 27, no. 3, pp. 314–335, February 2009.
- [18] D. Marpaung, C. Roeloffzen, R. Heideman, A. Leinse, S. Sales, and J. Capmany, “Integrated microwave photonics,” *Laser & Photonics Reviews*, vol. 7, no. 4, pp. 506–538, July 2013.
- [19] S. Iezekiel, M. Burla, J. Klamkin, D. Marpaung, and J. Capmany, “RF Engineering Meets Optoelectronics,” *IEEE Microwave Magazine*, vol. 16, no. 8, pp. 28–45, July 2015.
- [20] J. Capmany, J. Mora, I. Gasulla, J. Sancho, J. Lloret, and S. Sales, “Microwave Photonic Signal Processing,” *Journal of Lightwave Technology*, vol. 31, no. 4, pp. 571–586, February 2013.
- [21] D. Marpaung, J. Yao, and J. Capmany, “Integrated microwave photonics,” *Nature Photonics*, vol. 13, pp. 80–90, February 2019.

- 
- [22] A. Rahim, T. Spuesens, R. Baets, and W. Bogaerts, “Open-Access Silicon Photonics: Current Status and Emerging Initiatives,” *Proceedings of the IEEE*, vol. 106, no. 12, pp. 2313–2330, December 2018.
- [23] B. Jalali and S. Fathpour, “Silicon Photonics,” *Journal of Lightwave Technology*, vol. 24, no. 12, pp. 4600–4615, December 2006.
- [24] V. Stojanovic, R. J. Ram, M. Popovic, S. Lin, S. Moazeni, M. Wade, C. Sun, L. Alloatti, A. Atabaki, F. Pavanello, N. Mehta, and P. Bhargava, “Monolithic silicon-photonics platforms in state-of-the-art CMOS SOI processes,” *Optics Express*, vol. 26, no. 10, pp. 13 106–13 121, May 2018.



# 2

## RF Amplification for Narrowband Communication

### 2.1 Detection and Modulation

The two main functionalities of the opto-electronic Remote Antenna Unit (RAU) are being covered in this dissertation. This chapter will describe the modulation and detection of the RF signal while the addition of beam-forming functionality will be discussed in chapter 4. The main focus of this chapter is on the downlink part of the RAU which sequentially consists of converting the signal from the optical to the electrical domain, amplifying the generated RF signal and transmitting it over to the wireless channel.

To find out the required amplification, this chapter will start by providing a power budget estimation of an Analog Radio over Fiber (ARoF) link (section 2.2). Subsequently, it will be discussed why narrowband amplification techniques are preferred for mobile networks (section 2.3). When a broadband device is used, resonant peaking can be adopted to boost the performance of the amplifier in the frequency band of interest (section 2.4). When a receiver is designed from scratch, one can adopt an LNA design methodology to get optimal Signal-to-Noise Ratio (SNR) in the targeted frequency band (section 2.5). To conclude this chapter a reflective modulator will be discussed (section 2.6), adding the uplink path to the RAU.

## 2.2 Power budget

### 2.2.1 Downlink with Beamforming

The link budget calculation for the downlink (Table 2.1, based on the link depicted in Fig. 2.1) can be subdivided in the contributions from the Central Office (CO), channel and RAU. The central office consists of a continuous wave laser, a modulator and an Erbium Doped Fiber Amplifier (EDFA). The latter will determine the launched power while the MZM will determine the modulation depth. Assume 10 dBm of optical power is launched into the fiber [1] with a modulation depth of 50%.

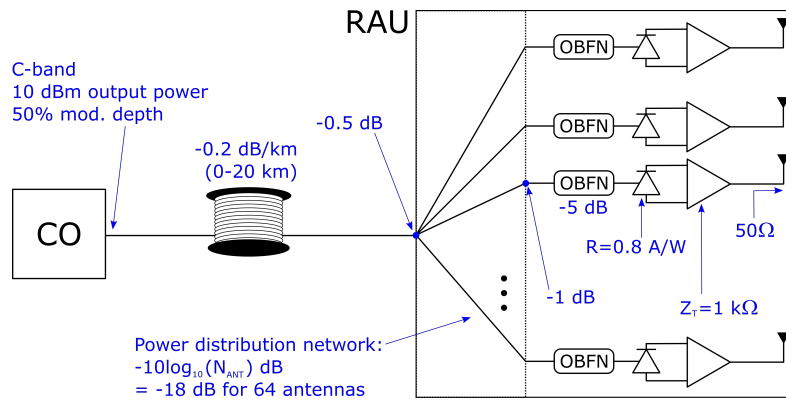


Figure 2.1: Downlink with beamforming: power budget calculation.

Component		Average	Modulation
Central Office		10 dBm	50 %
Fiber Loss	20 → 0 km	6 → 10 dBm	50 %
Coupling	-1.5 dB	4.5 → 8.5 dBm	50 %
PDN	-18 dB	-13.5 → -9.5 dBm	50 %
OBFN	-5 dB	-18.5 → -14.5 dBm	50 %
Photodetector	0.8 A/W	11.3 → 28.4 $\mu$ A	11.3 → 28.4 $\mu$ A <sub>p,p</sub>
RF Gain LNA	$Z_T = 1\text{k}\Omega$		11.3 → 28.4 mV <sub>p,p</sub>
	OFDM		-44 → -36 dBm
Array Gain	36 dBi		-8 → 0 dBm

Table 2.1: Power budget downlink, 8x8 antenna matrix.

Standard Single Mode Fiber (SSMF) adds an additional loss of about 0.2 dB per km for optical communication in C-band [2]. Average fiber lengths for

ARoF fronthaul are around 5 km and can reach up to 20 km [1, 3]. Therefore, the power penalty due to fiber attenuation can reach up to 4 dB. For the interposer we assume TriPleX [4] which results in about 0.5 dB coupling loss from the fiber to the interposer, almost no waveguide loss (less than 1 dB/m is possible) in the interposer itself, inherent splitting loss in the Power Distribution Network (PDN) and approximately 1.0 dB coupling loss from the interposer to the silicon Photonic Integrated Circuit (PIC). The inherent splitting loss  $IL_{PDN}$  can be calculated using equation 2.1 where  $N_{ant}$  describes the number of antenna elements. This equation shows a splitting ratio of -18 dB in an antenna array with 64 elements. Subsequently, the light passes through the Optical Beamforming Network (OBFN) for which we assume an insertion loss on the order of 5 dB, based on the insertion loss in the switchable optical delay line implementation in chapter 4.

$$IL_{PDN} = 10 \times \log_{10}(N_{ant}) \quad (2.1)$$

The photodetector used in this dissertation has a responsivity  $\mathcal{R}$  of 0.8 A/W at 1550 nm and because a modulation depth of 50 % ( $m=0.5$ ) was assumed we find a peak to peak RF current equal to the DC current. Consequently, we find required sensitivity levels of 11.3 to 28.4  $\mu A_{p,p}$  for a RAU with a 64 antenna matrix, as can be calculated from equations 2.2 and 2.3. The DC power incident on the photodetector shows that the linearity of the photodetector will be more than sufficient in this scheme.

$$I_{PD,avg} = \mathcal{R} \times 10^{P_{optical}/10} \quad (2.2)$$

$$I_{PD,pp} = 2m \times I_{PD,avg} \quad (2.3)$$

In this chapter, we will focus on the photoreceiver which is the first part of the receiver chain and should therefore introduce minimal noise. This photoreceiver combines the photodetection functionality and the initial low-noise, high-gain amplification. For the link budget calculations we assume a transimpedance of about 1 k $\Omega$  for this first amplifier. Consequently, the output voltage of the first amplification stage will be between 11.3 and 28.4 mV $_{p,p}$ , depending on the fiber length. Under the assumption that the link is used to transmit Orthogonal Frequency-Division Multiplexing (OFDM) signals with a Peak-to-Average Power Ratio (PAPR) of 12 dB [5], one can find rms voltage levels between 1.41 and 3.55 mV by calculating equation 2.4. Using these rms values and equation 2.5, one can see that the average power at the output of the first amplification stage is between -44 and -36 dBm, given a 50  $\Omega$  load impedance.

$$V_{rms} = \frac{V_{p,p}/2}{\sqrt{10^{PAPR/10}}} \quad (2.4)$$

$$P_{avg} = \frac{V_{rms}^2}{R_{load}} \quad (2.5)$$

A 64-element antenna array has a theoretical limit of 36 dB gain [6] over a single element, i.e.  $20 \times \log_{10}(64)$ . For simplicity sake, we assume isotropic radiation of the antenna and 100 % efficiency in the antenna. The Effective Isotropic Radiated Power (EIRP) of such a system (-8 to 0 dBm) is inadequate for deployment. Regulations maximize EIRP values to 75 dBm [7] while typical EIRP values for RAUs will be in the range of 60 to 65 dBm. Hence, additional power amplification will be required in between the low noise amplifier and the antenna for actual systems [8].

The inherent power decrease due to power splitting results in weak signals arriving at the photoreceiver. This problem becomes even worse when a larger antenna matrix is deployed. Therefore OBFNs will likely require optical amplification at the RAU. To improve the sensitivity of the photoreceiver and consequently relax required optical amplification at the RAU, the noise figure of the photoreceiver should be minimized.

Based on table 2.1, it can be seen that the beamforming gain is actually a null-operation for the link budget of the assumed ARoF link. Increasing the antenna count increases the beamforming gain at the same rate as it decreases the RF power generated by the individual photoreceivers (due to inherent splitting loss). In essence, changing the antenna count will shift the trade-off between required sensitivity and linearity. While it does not change the EIRP, increasing the antenna count will relax linearity requirements and it will allow for spatial diversity by enabling spatial selectivity. Furthermore, beamforming can help to reduce the overall power consumption of the system.

### 2.2.2 Downlink without Beamforming

An extra linearity specification is required to ensure that the constructed photoreceiver can also be used for our ARoF link experiments without beamforming functionality. The inherent power splitting ratio is not present and because no beamforming gain is available, a strong signal will need to be present at the input of the photoreceiver. Again assume maximally 10 dBm optical power arriving at the RAU and assume coupling from fiber to the silicon photonics IC via a grating coupler (3 to 5 dB insertion loss on

the iSiPP50G platform [9]). In that scenario about 6 dBm of optical power will be incident on a single photodetector. In chapter 3, techniques will be discussed to boost the power handling of the photodetector to provide high-linearity O/E conversion. Additionally, the linearity of the Low Noise Amplifier (LNA) should be taken into account. When an optical signal of 6 dBm and a modulation depth of 50 % is fed to a photodetector with a responsivity of 0.8 A/W, a  $3.2 \text{ mA}_{p,p}$  RF signal will be generated. Considering a transimpedance gain of approximately  $1 \text{ k}\Omega$ , this will result in  $3.2 \text{ V}_{p,p}$  at the output. In the LNA design, we therefore aim at an output referred 1-dB compression point of about 14 dBm. This also allows for a  $1 \text{ V}_{p,p}$  output signal with 10 dB back-off from the 1 dB compression level.

### 2.3 Narrowband Amplification

*The work in this section has in part been published in [10].*

Typical implementations of optical receivers in Radio over Fiber (RoF) links make use of a broadband Transimpedance Amplifier (TIA). The main topology (Fig. 2.2) used for designing a TIA is a shunt feedback amplifier. In this topology, a feedback resistor is placed between the input and output of an open loop amplifier [11]. In this way, high bandwidth can be combined with low noise behavior. At the input of the TIA a virtual ground is created. Consequently, the current generated in the photodetector will almost completely enter the TIA and will be converted to a voltage with amplification factor  $Z_T$ , the transimpedance gain. Such a TIA is usually designed to offer gain from DC to high frequencies with maximal gain flatness. Using a TIA for narrowband communication requires the TIA to have a bandwidth exceeding the carrier frequency of the narrowband signal while gain is only required in the part of the spectrum where the RF signal is present. Low pass amplification is important for digital communication in e.g. data centers, however, it is typically suboptimal for the narrowband schemes used in wireless communication because of unnecessary constraints imposed by the transimpedance limit [11]. In section 2.4, resonant inductive peaking at the input of a TIA is discussed to boost the performance of conventional broadband transimpedance amplifiers for narrowband communication. Such a resonant TIA relaxes the transimpedance limit and filters out-of-band noise but is only an intermediate solution as it still requires the design of a broadband TIA which is afterwards enhanced in the frequency range of interest.

Ideally, the narrowband nature of the transmitted data is already taken into account at the start of the design process resulting in a true narrowband

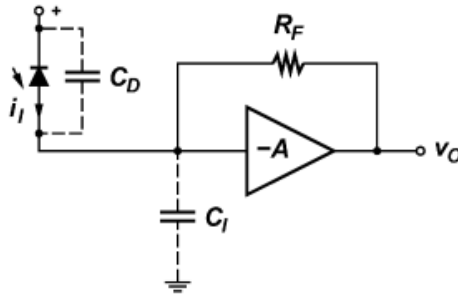


Figure 2.2: Shunt-feedback transimpedance amplifier [11].

design, as will be discussed in section 2.5. This true narrowband design is based on a dedicated LNA design to provide optimal power transfer from the RF signal generated in the photodetector to the desired load impedance in the frequency range of interest. This is in contrast to the broadband transimpedance amplifiers that provide suboptimal current-to-voltage conversion from DC up to the maximum frequency of interest [12]. This difference becomes even more important when higher RF carriers are envisioned. Increasing the requirement on the bandwidth of the TIA will require a lower resistance  $R_F$  in the feedback path. This results in lower transimpedance gain since the transimpedance limit (eq. 2.6, [11]) shows inverse proportionality with the required bandwidth squared. The factor  $GBW$  in eq. [11] denotes the gain-bandwidth product of the open loop amplifier while  $C_T$  denotes the total capacitance at the input node of the TIA. Furthermore, an increase in thermal noise contribution is to be expected when the feedback resistance  $R_F$  drops [13].

$$R_T \leq \frac{GBW}{2\pi C_T BW^2} \quad (2.6)$$

The narrowband LNA design methodology will allow for a more optimal trade-off between the minimization of noise and maximization of gain, especially at higher frequencies. An added benefit is the fact that parasitics can be resonated out (e.g. wirebond inductance) in a narrowband design while they deteriorate the performance in broadband amplifiers, making the LNA more high-frequency friendly than traditional TIA configurations. The main challenge of the LNA design is that a shift in passband is detrimental due to the resonant nature of the circuit. Therefore, a dedicated design is required which will depend on the targeted frequency band and adopted photodetector. Additionally, a good knowledge of parasitics present in the amplifier and in the photoreceiver assembly is paramount.

## 2.4 Resonant Transimpedance Amplifier

*The work in this section has in part been published in [14].*

### 2.4.1 Input Circuit Model

To explain the operation principle of the resonant TIA, a model needs to be constructed for the input circuitry. This model consists of two parts, namely, the photodetector and the interconnection. The photodetector itself can be modeled with a current source  $I_{PD}$ , a junction capacitance  $C_j$ , a shunt resistance  $R_{sh}$ , and a series resistance  $R_{s,p}$  [15]. The shunt resistance can typically be neglected, hence, its influence will be ignored for the remainder of chapter 2. Secondly, the interconnect parasitics connecting the Photodetector (PD) to the TIA are modeled as a series resistor-inductor impedance. In case of a broadband design methodology, the tolerated amount of inductance is limited (although a small inductance value might slightly increase the bandwidth without introducing peaking). For passband applications, however, the presence of the lead inductor can be utilized to our advantage to introduce high-Q peaking and favor the transfer of the desired frequency band by shaping the frequency dependent gain. In subsequent discussions, any series resistance introduced by the interconnections will be combined with the series resistance in the photodetector, i.e.  $R_s = R_{s,p} + R_{s,lead}$ . Furthermore, the influence of the shunt resistance  $R_{sh}$  of the photodetector shall be neglected.

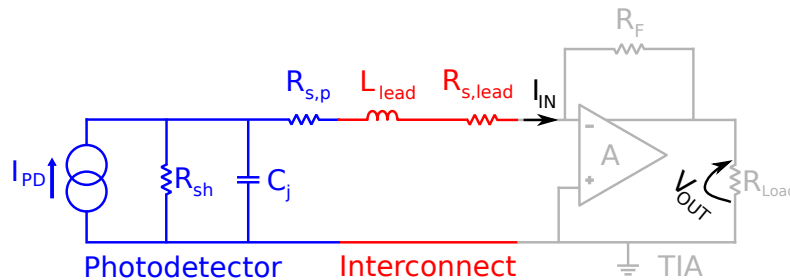


Figure 2.3: Transimpedance amplifier with detailed input circuit model.

### 2.4.2 Series Inductive Peaking

The analytic expressions for the resonant TIA will be derived starting from an ideal TIA. The loop gain should be sufficiently high at all frequencies of interest. Furthermore, the feedback resistance  $R_F$  is sized in such a way

that the input resistance  $R_{in}$  given in eq. 2.7 [13] is significantly smaller than the capacitive input impedance  $1/sC_{in}$  of the TIA. This is required to ensure that most of the current entering the TIA will couple to the output through the feedback resistance. The parameter  $A$  in eq. 2.7 denotes the open loop voltage gain of the amplifier.

$$R_{in} \approx \frac{R_F}{A + 1} \quad (2.7)$$

$$Z_T = \frac{V_{OUT}}{I_{PD}} = \frac{I_{IN}}{I_{PD}} \times \frac{V_{OUT}}{I_{IN}} = \frac{I_{IN}}{I_{PD}} \times -R_F \quad (2.8)$$

The transimpedance of the resonant receiver can be described by the product of two transfer functions (eq. 2.8). The first part is the frequency dependent input circuitry, which will perform gain shaping to favor the desired frequency band by adopting series inductive peaking. Secondly, a current-to-voltage conversion is realized through the feedback path of the TIA. To simplify further calculations, the broadband transimpedance operation is assumed to be frequency flat for all frequencies of interest due to a frequency independent open loop voltage gain  $A$  and  $1/\omega C_{in} \gg R_{in}$ .

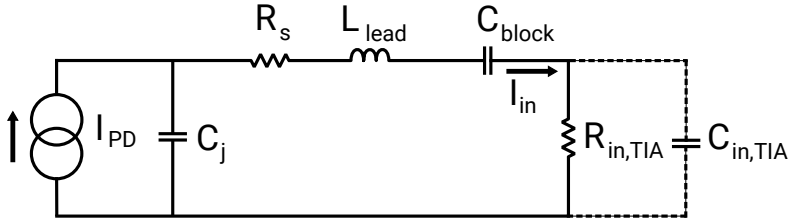


Figure 2.4: Input circuitry TIA with series inductive peaking [14].

The first term in equation 2.8, i.e. the frequency dependent gain shaping of the input, can be calculated based on the equivalent circuit depicted in Fig. 2.4. The equivalent network of the photodetector-wirebond combination is loaded with the input impedance of the TIA. When sizing the circuit correctly, it is possible to initially neglect the input capacitance for all frequencies of interest and approximate the input impedance of the broadband TIA by  $R_{in}$  described in eq. 2.7. As discussed before, this is required to make sure that most of the RF current  $I_{IN}$  flows through the feedback path. Biasing the TIA and PD independently will require the use of a series capacitor. Its value is typically chosen in such a way that it behaves as an RF short. In Figure 2.4, this DC-blocking capacitor was added explicitly to add extra tunability to the gain shaping by the input network.

The transfer function of the input network, given in equation 2.9, is easily obtained by observing that the circuit behaves as a current divider. When the capacitor  $C_{block}$  is realized as an ideal DC block, the resonance (i.e. peaking) frequency  $\omega_0$  of this second order low-pass transfer function will depend only on  $L_{lead}$  and  $C_j$ , as can be seen in eq. 2.10.  $L_{lead}$  can be increased by adding an explicit inductance  $L_{explicit}$  in series with the original lead inductance, giving rise to a decrease in resonance frequency (eq. 2.11). The disadvantage of using such a simple input circuit is that the product of  $L_{lead}$  and  $C_j$  will introduce an upper limit on the maximally achievable peaking frequency. This problem can be circumvented by using a finite value for  $C_{block}$  (eq. 2.12). The parameter  $\alpha (= \sqrt{1 + C_j/C_{block}})$  describes the factor by which the resonance frequency is increased when using a series capacitor with finite value  $C_{block}$ .

$$\frac{I_{IN}}{I_{PD}} = \frac{1}{(1 + \frac{C_j}{C_{block}}) + sC_j(R_{in} + R_s) + s^2L_{lead}C_j} \quad (2.9)$$

$$\omega_0(L_{explicit} = 0, C_{block} = \infty) = \frac{1}{\sqrt{L_{lead}C_j}} \quad (2.10)$$

$$\omega_0(C_{block} = \infty) = \frac{1}{\sqrt{(L_{lead} + L_{explicit})C_j}} \quad (2.11)$$

$$\omega_0 = \frac{\sqrt{1 + \frac{C_j}{C_{block}}}}{\sqrt{(L_{lead} + L_{explicit})C_j}} \triangleq \alpha \times \omega_0(C_{block} = \infty) \quad (2.12)$$

The peak height  $|I_{in}(\omega_0)/I_{in}(0)|$  is described by the Quality (Q)-factor which can be calculated with eq. 2.13 [16]. This value will have a major impact on the performance improvement of the system. Regarding the noise behavior, it is advisable to work with a high Q-factor peak as it will boost the useful band relative to the broadband noise. However, it should be stressed that a higher Q also results in a lower signal bandwidth. Hence the Q-factor should be within certain bandwidth-determined boundaries. Consequently, the required bandwidth shall pose a limit to how much noise improvement we can expect by using this method. The available 3 dB (peaking) bandwidth  $\Delta\omega$  is found to be inversely proportional to the Q-factor (eq. 2.14). Especially when the relative bandwidth is very small, we can expect large sensitivity improvements by adopting input series inductive peaking.

$$Q = \omega_0 \frac{L_{lead} + L_{explicit}}{R_{in} + R_s} = \frac{\alpha}{R_{in} + R_s} \sqrt{\frac{L_{lead} + L_{explicit}}{C_j}} \quad (2.13)$$

$$\frac{\Delta\omega}{\omega_0} \approx \frac{1}{Q} \quad (2.14)$$

The main advantages of adopting a resonant TIA approach is that it shapes the transfer function to favor gain in the spectral range of interest and the fact that it helps to boost the transimpedance gain, potentially over the transimpedance limit [11]. The first can also be obtained when an additional bandpass filter is used. Such a filter is passive and hence does not increase the transimpedance gain. The resonant TIA discussed in this section however boosts the transimpedance gain. To prove this, the transimpedance gain at the resonance frequency is given in eq. 2.15. The resonance frequency is to be designed to coincide with the RF carrier and it is clear that if a small relative bandwidth is targeted, the Q-factor can be high and the transimpedance gain can be boosted significantly at the carrier frequency.

$$Z_T(\omega_0) = -R_F \times Q \times \frac{1}{\alpha^2} \quad (2.15)$$

In [14], a proof-of-concept of such a resonant TIA with input series inductive peaking was demonstrated. The TIA uses off-the-shelf components and is based on a common emitter topology with shunt feedback between collector and base. For the proof-of-concept we realized a 4 GHz carrier. This resonant TIA was used for a 150 MBd, 64 Quadrature Amplitude Modulation (QAM) link showing an SNR of 35.8 dB with 3 tap equalization.

## 2.5 Narrowband Photoreceiver

*The work in this section has in part been published in [10, 17].*

### 2.5.1 0.1 $\mu\text{m}$ pHEMT GaAs Technology

While SiGe BiCMOS can be adopted to reach EIRP values in the 60 dBm range, high antenna counts are required (Fig. 2.5). To provide sufficiently high output power levels with lower antenna count, III-V materials should be adopted for the design of the amplifier [18, 19]. There exist several platforms (GaAs, InP, GaN, ...) offering distinct advantages and disadvantages. In this dissertation, GaAs was chosen since it offers high-frequency, moderately high-power amplification (Fig. 2.6) at a much lower cost than other III-V compounds. Additionally, the GaAs industry is mature, offers a high yield and reproducibility [20]. An added benefit is the availability of high-quality passives because of the high substrate resistivity.

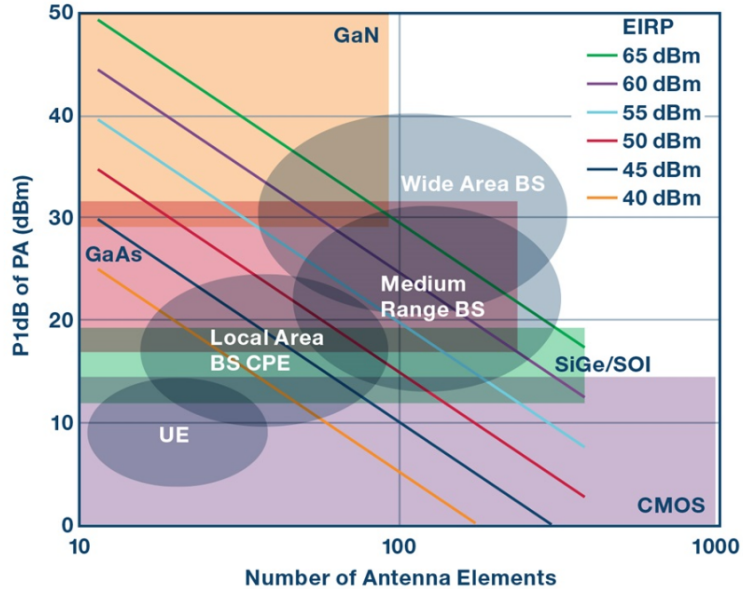


Figure 2.5: Technology fit for various millimeter wave radio form factors based on transmitter power [18].

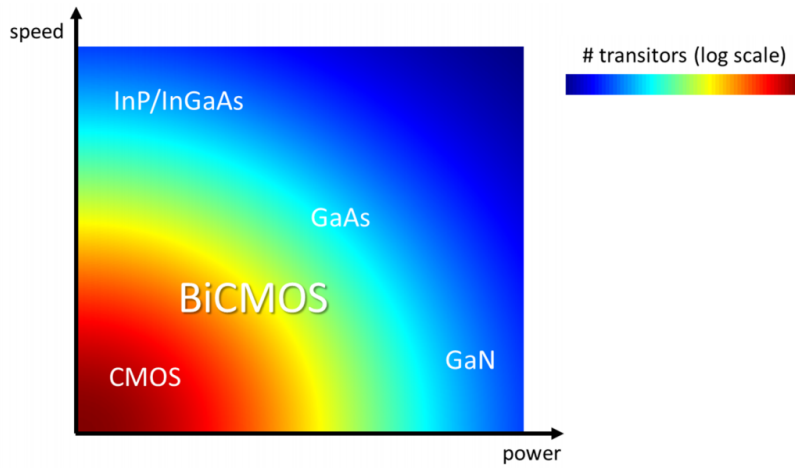


Figure 2.6: Technology landscape [21].

For the implementation of the RF amplifier, a  $0.1 \mu\text{m}$  Pseudomorphic High-Electron Mobility Transistor (pHEMT) GaAs technology platform with a transition frequency  $f_T$  of 130 GHz is used [22]. HEMT structures rely on heterojunctions (e.g. GaAs/InGaAs/AlGaAs) to construct a quantum well that forms the channel [20]. Since HEMT devices make use of non-doped channels (i.e. the quantum well), no collisions with the dopants occur and therefore a higher mobility and lower noise can be achieved. The pseudomorphic HEMT variant uses a thin layer to generate the heterojunction to make sure that the difference in lattice constant for the different materials does not introduce crystal defects.

## 2.5.2 Photoreceiver Design and Assembly

### 2.5.2.1 Input Circuitry

The devised narrowband photoreceiver comprises a Ge photodetector and a GaAs LNA as can be seen in Fig. 2.7. In this section, the design of a three stage LNA is discussed based on a readily available Ge-on-Si waveguide-integrated vertical pin photodetector from imec's iSiPP50G silicon photonics platform [9]. As a first step in the design process of the photoreceiver, a model of the input circuit needs to be derived. This equivalent model for the input circuit consists of two parts: the photodetector and the wirebonds interconnecting the photonic and electronic IC. The combined effect is depicted in Fig. 2.8. The photodetector can be approximated by a parallel combination of a current source  $I_{PD}$  and a junction capacitance  $C_j$ . Losses in the photodetector are modelled by adding a series resistance  $R_s$  to this parallel combination. This resistance is approximately independent of the photodetector voltage while the junction capacitance decreases with increasing reverse voltage. The photocurrent  $I_{PD}$  is proportional to the incident optical power with proportionality factor  $\mathcal{R}$ . The responsivity  $\mathcal{R}$  is  $0.8 \text{ A/W}$  at  $1550 \text{ nm}$  for the adopted photodetector and coupling to the chip is done by using a grating coupler which results in about 5 dB insertion loss. Furthermore it should be noted that all the results given in this chapter are for TE polarized light due to the polarization sensitive nature of the grating couplers.

For the adopted photodetector, the series resistance is  $45 \Omega$  and the junction capacitance changes between 71 and 47 fF for photodetector reverse voltages of 0 and 3 V respectively. The LNA was designed for a nominal reverse voltage of 1 V resulting in a 55 fF junction capacitance. A second part of the model is the wirebond inductance  $L_{wb}$ . This inductance is modelled by approximating the wirebond pair as a current loop consisting of two conductors of  $25 \mu\text{m}$  diameter spaced  $100 \mu\text{m}$  apart and having a

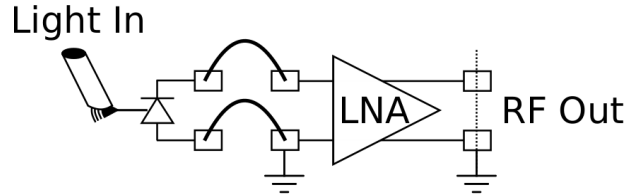


Figure 2.7: Schematic overview of the photoreceiver [10].

length of around  $600 \mu\text{m}$ . Assuming these dimensions, an inductance value of  $495 \text{ pH}$  is found [23]. Adopting these values results in a nominal source impedance  $Z_s$  of  $45-j12.9 \Omega$  at  $28.5 \text{ GHz}$ . To compensate for changes in the wirebond length, the reverse voltage of the photodetector can be adjusted to change the junction capacitance accordingly.

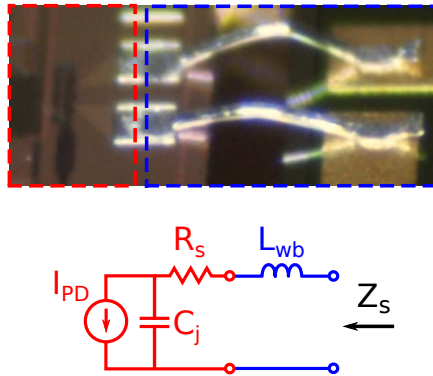


Figure 2.8: Input circuit seen by the LNA: PD-wirebond combination [10].

In the following subsections, the different stages of the LNA will be discussed briefly. A three stage amplifier is optimized for operation in the  $27.5\text{--}29.5 \text{ GHz}$  band. The source impedance  $Z_s$  is  $45-j12.9 \Omega$  at  $28.5 \text{ GHz}$ , and it is required to have an internal bias tee at the input of the LNA to enable independent biasing of the photodetector. The targeted load impedance is  $50 \Omega$  and should be DC blocked. The high frequency behavior of parasitics and passives were estimated using the 2.5 D solver ADS momentum. During the design of the photoreceiver, 5G wireless communication in the  $28 \text{ GHz}$  band was typically limited to  $27.5\text{--}29.5 \text{ GHz}$  and therefore it was mainly designed for optimal performance in the aforementioned spectral range. However, the band has been extended to  $24.25\text{--}29.5 \text{ GHz}$ , and therefore this work will also explore the performance of the receiver in the extended  $28 \text{ GHz}$  band in chapter 5.

### 2.5.2.2 LNA Design

**First Stage:** For the first stage, the trade-off between noise and gain matching is of paramount importance. Good noise matching is required to get a low noise behavior while high gain is required to minimize influence of noise induced by subsequent stages and to get good overall gain. While gain and noise characteristics are critical, stability should be preserved and good matching at in- and output is required to avoid ringing. To get good noise and gain matching while trading in excess output return loss for improved input return loss, the design strategy discussed in [24] was adopted. The final result of the first stage is depicted in Fig. 2.9, where the length of the transmission line segments are given in degrees at 28.5 GHz.

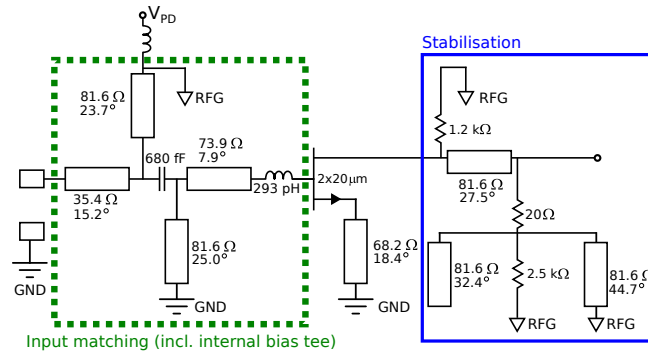


Figure 2.9: Amplifier stage 1 – RFG: RF ground [10].

Source degeneration is used to bring the optimal source impedances for noise and gain matching closer together and consequently get a better overall gain-noise performance. To ensure stability at the operation frequency, a shunt resistor is added at the drain. Subsequently, a parallel RLC network is added to extend this up to the transition frequency  $f_T$  of the transistor. The pHEMT uses a zero volt DC gate-source level to allow self-biasing of the gate. This technique reduces the complexity of the amplifier and is also adopted in the subsequent stages. The input matching network of the first stage contains a bias tee to enable biasing of the photodetector and to make sure that any DC current generated by the photodetector is not saturating the amplifier. An important component in the design of the discussed LNA is the RF Ground (RFG) which is an over-via-capacitor, i.e. a parallel plate capacitor on top of a via. By correctly dimensioning the capacitor it resonates with the via inductance such that the RFG acts as a ground at the operation frequency and as an open at DC. The global ground indicated by GND in Fig. 2.9 will on the contrary act as a ground at all frequencies.

**Second Stage:** The design of the second stage was done in a similar fashion as the first stage. The main difference concerns the fact that the source impedance follows from the output impedance of the first stage in combination with the interstage matching network. The final implementation of this second stage is shown in Fig. 2.10.

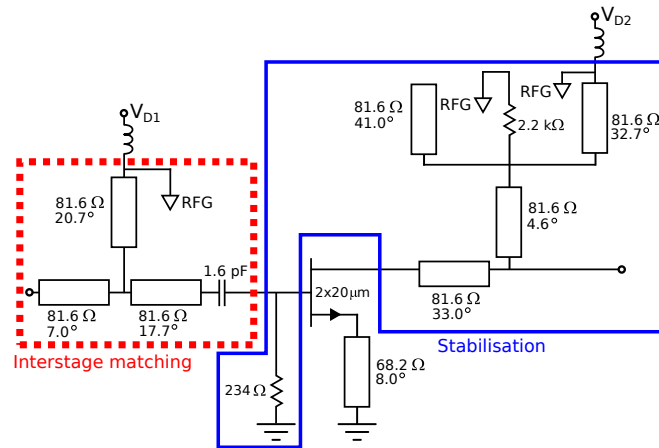


Figure 2.10: Amplifier stage 2 [10].

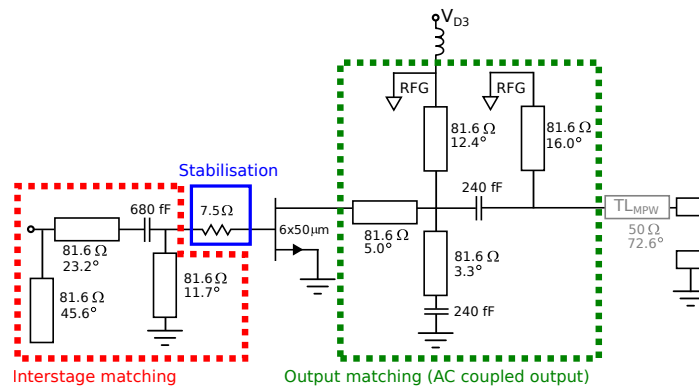


Figure 2.11: Amplifier stage 3 [10].

**Third Stage:** For the final stage, an identical design strategy as for the 2nd stage was followed. Unconditional stability is ensured by adding a 7.5 Ω resistor in series with the gate and the resulting schematic of the final

stage is depicted in Fig. 2.11. A  $50\ \Omega$  transmission line is present at the output of the LNA to ensure compatibility with predefined MultiProject Wafer (MPW) chip sizes. This transmission line segment, indicated by  $TL_{MPW}$ , is therefore not a functional part of the LNA.

**Unconditional Stability:** All three stages were designed to offer unconditional stability per individual stage up to the transition frequency  $f_T$  of the technology, i.e. 130 GHz. In the first stage, stabilization is located at the output rather than the input to avoid unnecessary noise degradation. In contrast, the stabilization resistance of the final stage is found at its input to avoid a drop in the available gain that would otherwise result from output stabilization.

### 2.5.2.3 Photoreceiver Assembly

The final design of the LNA is shown in Fig. 2.13 and consists of 3 amplification stages that can be biased independently. In practice, however, these DC lines will be connected to a single power supply  $V_D$  to minimize biasing complexity. The input of the amplifier is wirebonded to a Ge-on-Si photodetector and is connected to  $V_{PD}$  with an internal bias tee to counter inductance variations and source DC current generated by the photodetector. At the output, AC coupling is present and a  $50\ \Omega$  load is expected. The photoreceiver assembly is shown in Fig. 2.12 where the DC pads of the LNA are connected to Printed Circuit Board (PCB) traces with chip capacitors of 10 and 100 nF for additional decoupling.

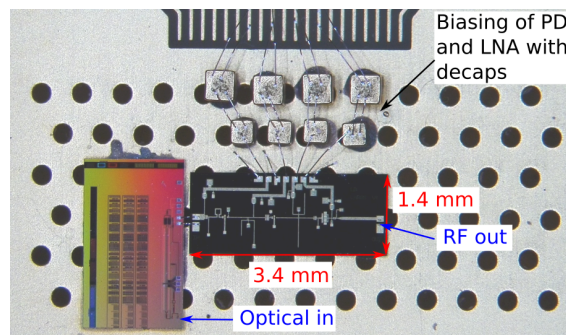


Figure 2.12: Narrowband photoreceiver assembly [10].

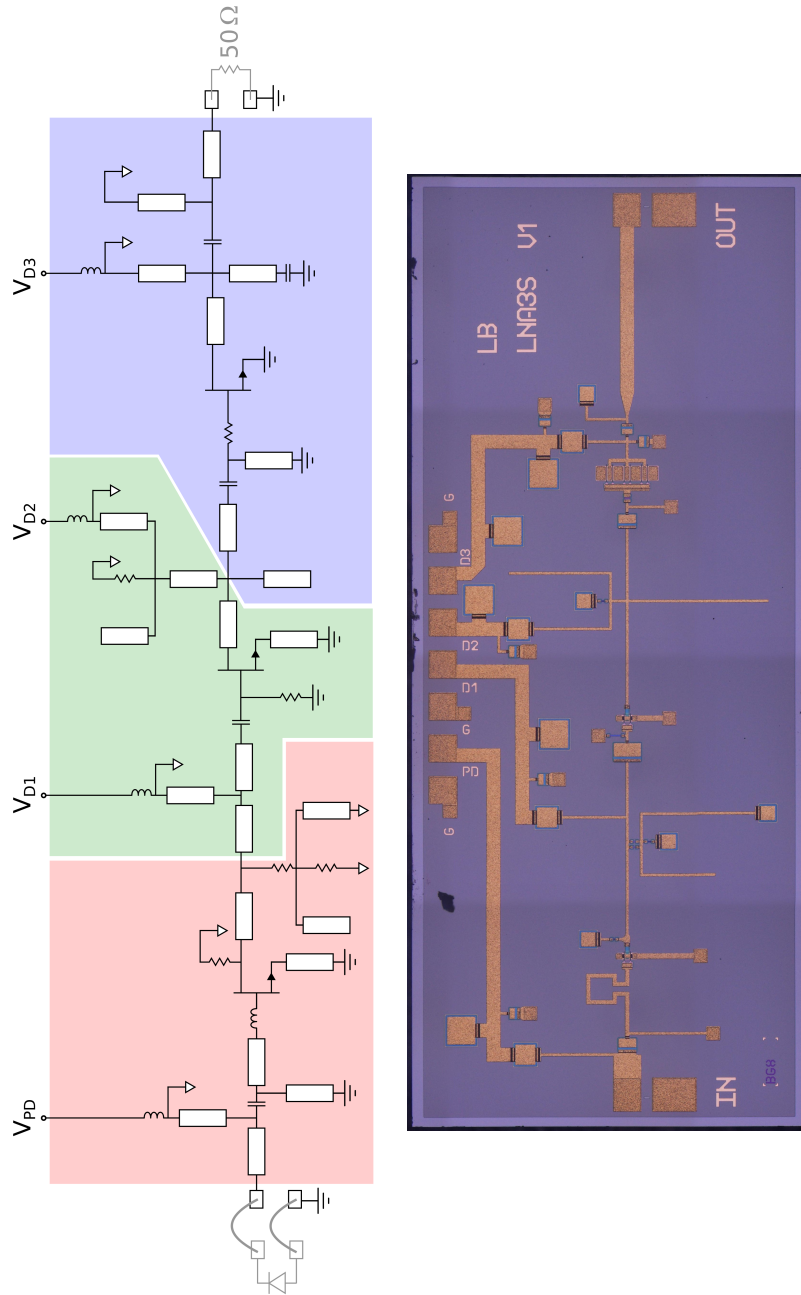


Figure 2.13: 3-stage mmWave LNA: (top) Schematic; (bottom) Microscope picture [10].

### 2.5.3 LNA Performance

*In this chapter, the photoreceiver is characterized as a standalone device. The data transmission experiments are presented in chapter 5.*

#### 2.5.3.1 Small Signal Behavior

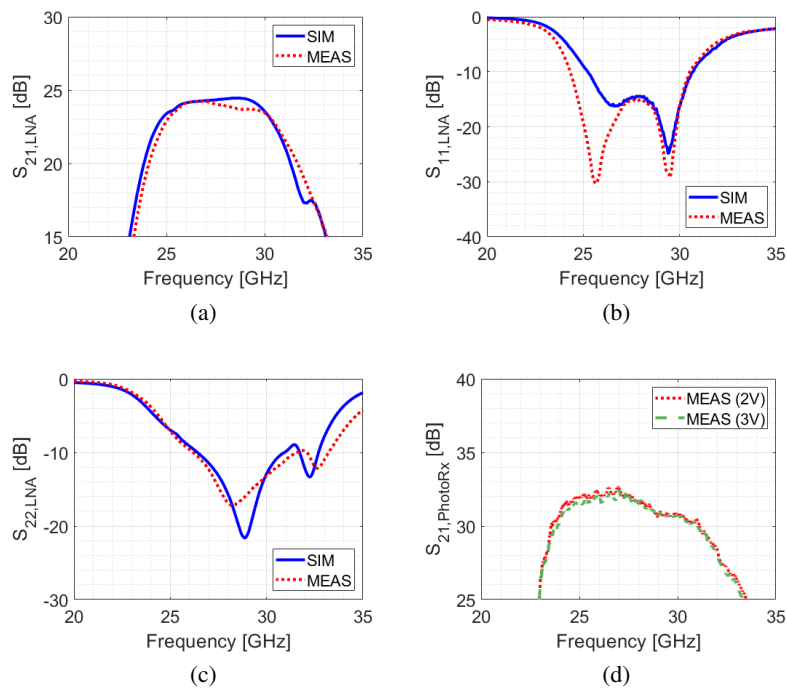


Figure 2.14: (a)-(c) LNA S-parameters: Simulations and measurements (d) Normalized opto-electrical response [10].

To determine the S-parameters of the LNA, a setup with a Vector Network Analyzer (VNA) and 2 probes was used after which the influence of the probes was compensated for using a Short-Open-Load-Thru (SOLT) calibration substrate. This provides the S-parameters of the Device Under Test (DUT) in a  $50\ \Omega$  environment. As the source is not  $50\ \Omega$ , these S-parameters give a distorted interpretation. To give a result that is easier to interpret, S-parameter transformations are performed [25] to display the S-parameters for the actual source impedance (Fig. 2.8). The adopted output reference impedance remains  $50\ \Omega$  as this is also the load for which the LNA was

designed. The results are compared with simulations in Fig. 2.14 (a)-(c) after the aforementioned source reference transformation to the photodiode-wirebond combination. Both the simulated and measured small signal behavior in Fig. 2.14 (a)-(c) are given for a 2 V supply. Simulations and measurements agree very well apart from the presence of an additional dip in the measured  $S_{11}$  of the LNA. In Fig. 2.15, the measured and simulated  $S_{11}$  are shown together with the conjugate match of the measured source impedance (Fig. 2.8) on a Smith chart with a  $50\ \Omega$  reference. The measured and simulated curves follow a similar shape but deviate slightly, resulting in the extra dip in S-parameters. This is probably caused by some small deviations in the input matching network.

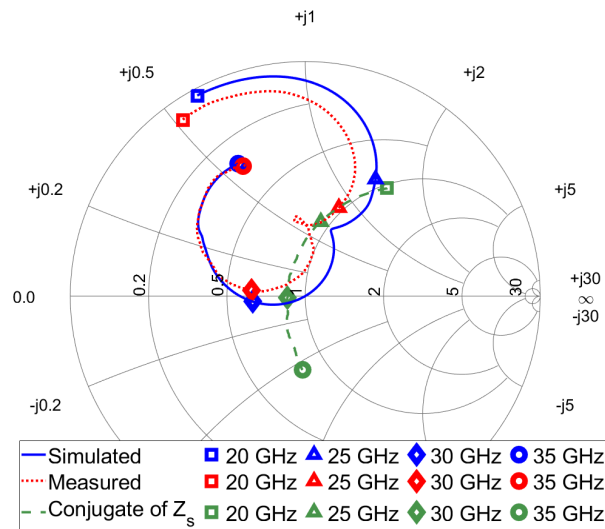


Figure 2.15:  $S_{11}$  of the LNA on the Smith chart for a  $50\ \Omega$  reference [10].

Figure 2.14(a) shows that the measured  $S_{21}$  ranges between 24.0 to 23.7 dB in the 27.5 to 29.5 GHz range, which corresponds with 884 to 788 V/A transimpedance gain from the current source  $I_{PD}$  to a  $50\ \Omega$  load. Taking into account the responsivity of the adopted photodetector (0.8 A/W at 1550 nm), a conversion gain of 707 to 630 V/W is obtained from the input of the photodetector to a  $50\ \Omega$  load. The external conversion gain from the fiber input to the output of the LNA is 224 to 199 V/W due to the 5 dB coupling loss caused by the grating coupler. This can be enhanced by making use of edge coupling to reduce the coupling loss to about 1.2 dB which would result in a conversion gain of 536 to 478 V/W. The measured 3-dB cut-off frequencies are situated at 24.4 and 31.2 GHz. Input and output re-

turn loss stay below -14.3 and -14.4 dB respectively in the 27.5 – 29.5 GHz range and the -10 dB return loss bandwidth covers 24.3 to 30.5 GHz at the input and 26.2 to 31.6 GHz at the output. In Fig. 2.14(d), the transfer characteristic of the entire photoreceiver is presented. A similarly shaped transfer function is obtained but with slightly shifted 3-dB frequencies (23.5 and 31.5 GHz). This slight change in 3 dB bandwidth can be attributed to the fact that the photoreceiver measurement includes the behavior of the actual wirebonds while the S-parameters shown in Fig. 2.14 (a)-(c) approximate the wirebond pair as a single inductor. Additionally, it can be seen in Fig. 2.14(d) that the change from a 2 V (*low power consumption setting*) to a 3 V supply (*high linearity setting*) has a negligible impact on the small-signal transfer function of the photoreceiver.

### 2.5.3.2 Linearity

Initial simulations showed an expected Output referred third order Intercept Point (OIP3) of 20.4 and 24.1 dBm at 28.5 GHz for respectively 2 and 3 V supplied to the drain of the three stages. The corresponding values for the Output referred 1-dB Compression Point (O1dBCP) are respectively 9.7 and 13.6 dBm. The simulated power consumption increases from 103 to 211 mW when increasing the drain supply from 2 to 3 V. DC testing of the LNA shows a higher power consumption than anticipated (respectively 160 mW and 303 mW) and it was found that this can be attributed to process variations on the threshold of the pHEMT transistors. Adjusting threshold levels in simulations to get corresponding DC behavior shows that an increase in linearity is expected. The newly obtained values are 21.8 dBm (2V) and 26.3 dBm (3V) for the OIP3 and 10.2 dBm (2V) and 13.9 dBm (3V) for the O1dBCP. Two tone OIP3 measurements result in measured levels of 22.2 dBm (2V) and 26.5 dBm (3V) at 28.5 GHz with 20 MHz tone spacing agreeing very well with the simulated values after threshold compensation.

$$PAE[\%] = 100 \times \frac{P_{out}^{rf} - P_{in}^{rf}}{P_{dc}} \quad (2.16)$$

Based on the simulations, the power added efficiency (PAE, eq. 2.16) was calculated for the photoreceiver for different input power levels and amplifier drain settings. When the LNA supply is 2V, the maximum PAE is 18.9%. Furthermore, the PAE at the 1 dB compression level is 8.9% for this low-power setting. When the LNA supply is 3V, the maximum PAE increases to 19.1%. Furthermore, the PAE at the 1 dB compression level increases to 10.7% for this high-linearity setting.

### 2.5.3.3 Noise

In this section the simulated noise performance of the LNA will be discussed (Fig. 2.16). When the three stages are biased with a 2 V supply, the expected Noise Figure (NF) ranges between 2.09 dB and 2.16 dB in the frequency range of interest (27.5 to 29.5 GHz). Increasing this supply to 3 V results in increased NF values ranging between 2.26 and 2.32 dB. The input-referred current noise results in a more straightforward interpretation of the sensitivity of the photoreceiver [13]. For the discussed LNA in the targeted frequency band, 2 V and 3 V drain supply results in respectively an input-referred Root Mean Square (RMS) current noise below 11.1 and 11.3 pA/ $\sqrt{\text{Hz}}$ . When the noise contribution of the series resistance of the photodetector is excluded, this drops to respectively 6.8 and 7.1 pA/ $\sqrt{\text{Hz}}$ .

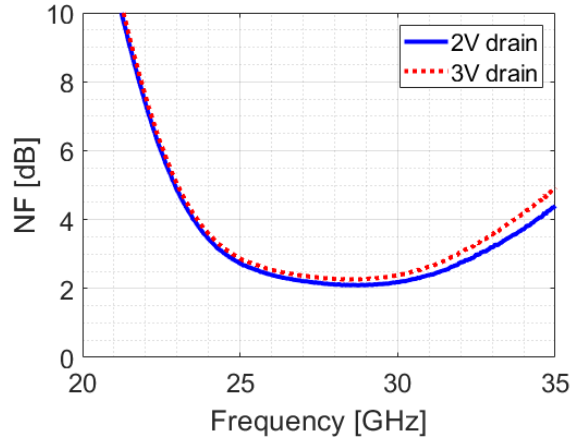


Figure 2.16: Simulated noise figure of the LNA for 2 and 3V supply [10].

A good measure to quantify the dynamic range of the receiver is the Spurious Free Dynamic Range (SFDR). The value of the SFDR can be calculated by using equation 2.17 [26] and describes the difference of power levels for which the fundamental and third order intermodulation exceed the noise floor.

$$\begin{aligned}
 SFDR &= \frac{2}{3} [OIP_3 - \text{Noise Floor}] \\
 &= \frac{2}{3} [OIP_3 + 174 - 10 \log_{10}(B) - S_{21} - NF]
 \end{aligned}
 \tag{2.17}$$

OIP3 is the output referred intercept point (in dBm), B is the bandwidth (in Hz),  $S_{21}$  is the gain of the LNA (in dB) and NF is the noise figure of the

LNA (in dB). Equation 2.17 assumes the input noise power of the LNA to be dominated by thermal noise, which equals  $-174 \text{ dBm} + 10 \times \log_{10}(B)$  at 290 Kelvin [27]. The resulting SFDR depends on the noise bandwidth and the LNA bias and is shown in Fig. 2.17. It is clear that the dynamic range is improved when increasing the bias from 2 to 3 Volt due to the increase in linearity.

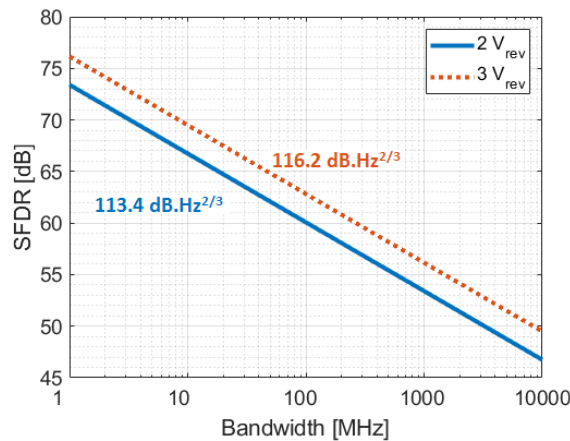


Figure 2.17: Spurious free dynamic range of the LNA.

#### 2.5.4 State of the art

A state of the art comparison is shown in table 2.2. It can be seen that the input referred current noise lies in between the values of [28] and [29, 30], respectively corresponding to photoreceivers for lower and higher operation frequencies. This is to be expected as the minimum noise figure increases toward higher frequencies [22] and because the passives become lossier at higher frequencies. The transimpedance is comparable to the state of the art apart from the photoreceiver discussed in [29], where multiple amplifier chips are cascaded rather than having a single EIC. Regarding the linearity and power consumption, it can be seen that the presented photoreceiver offers a high linearity while offering low power consumption.

To compare the results to state of the art silicon mmWave low noise amplifiers, table 2.3 is provided. This table clearly shows that the amplifier designed in this dissertation offers a higher linearity and often a higher gain and lower noise figure than silicon mmWave LNAs. However, this comes at the cost of a bulkier device that consumes significantly more power. It

should be noted that the size of the LNA discussed in this dissertation can be reduced as its dimensions are now limited by MPW predefined chip sizes. Nevertheless, even if the GaAs amplifier will be optimized for size, it will remain bulkier than the silicon based amplifiers.

	Technology	Passband, 3-dB	Gain
[10]	GaAs, 0.1 $\mu$ m pHEMT	23.5–31.5 GHz	$S_{21}$ =24 dB, $Z_T$ =884 $\Omega$
[10]	GaAs, 0.1 $\mu$ m pHEMT	23.5–31.5 GHz	$S_{21}$ =24 dB, $Z_T$ =884 $\Omega$
[28]	GaAs, 0.15 $\mu$ m pHEMT	8.9–9.6 GHz	$Z_T$ =1.6 k $\Omega$
[28]	GaAs, 0.15 $\mu$ m pHEMT	9.2–10.1 GHz	$Z_T$ =5.3 k $\Omega$
[31]	InP, 0.25 $\mu$ m HEMT	34–41 GHz	$S_{21}$ =23 dB, $Z_T$ =1.1 k $\Omega$
[29]	GaAs, 0.2 $\mu$ m pHEMT	40.4–41.4 GHz	$Z_T$ =35.5 k $\Omega$
[30]	GaAs, HEMT	49–59 GHz	$Z_T$ =750 $\Omega$
[32]	GaAs, 0.1 $\mu$ m pHEMT	91–98 GHz	$S_{21}$ =22 dB
[32]	InP, pHEMT	90–110 GHz	$S_{21}$ =20 dB

	Input ref. current noise	Linearity	DC Power
[10]	11.1 pA/ $\sqrt{Hz}$	OIP3=22.2 dBm	160 mW
[10]	11.3 pA/ $\sqrt{Hz}$	OIP3=26.5 dBm	303 mW
[28]	5.9 pA/ $\sqrt{Hz}$	—	—
[28]	5.7 pA/ $\sqrt{Hz}$	—	—
[31]	—	—	—
[29]	23 pA/ $\sqrt{Hz}$	—	432 mW
[30]	20 pA/ $\sqrt{Hz}$	OIP3=21 dBm	965 mW
[32]	—	$P_{sat}$ =9.5 dBm	219 mW
[32]	—	$P_{sat}$ =6 dBm	70 mW

Table 2.2: Photoreceiver state of the art –  $Z_T$ : Transimpedance; OIP3: Output Third-Order Intercept;  $P_{sat}$ : Output Saturation [10].

## 2.6 Narrowband Reflective EAM Driver

In a small-cell architecture, it would be advantageous if the laser can be omitted from the RAU to reduce the cost and power consumption [40–43]. The centralization of the light generation for the uplink path allows for sharing the laser between multiple cells and relaxes the stringent temperature

	Technology	$S_{21}$ dB	$f_{3dB}$ GHz	NF dB	$P_{DC}$ mW	Area mm <sup>2</sup>	OIP3 dBm
<b>This</b>	100nm, GaAs	24	23.5-31.5	2.1	303	4.76	26.5
<b>This</b>	100nm, GaAs	24	23.5-31.5	2.1	160	4.76	22.2
[33]	22nm, FDSOI	21.5	19-36	1.7	17.3	0.05	8.1
[34]	40nm, CMOS	27.1	26-32.7	3.3	31.4	0.26	14.5
[35]	65nm, CMOS	10.2	15.8-30.3	3.3	12.4	0.18	9.7
[36]	65nm, CMOS	17.9	17.5-26	3.3	5.6	0.51	12.9
[37]	130nm, SiGe	16.2	24-30	2.8	8.2	0.1	14.2 <sup>†</sup>
[38]	120nm, SiGe	23.5	29.5-36.2	2.9	11	0.09	4
[39]	180nm, SiGe	12	23-32	4.5	13	0.25	6

Table 2.3: Comparison to state of the art mmWave silicon low noise amplifiers –  $f_{3dB}$ : 3-dB bandwidth;  $P_{DC}$ : power consumption;

<sup>†</sup> calculated using  $OIP3 \approx P_{out,1dB} + 10dB$ .

control requirements at the RAUs. This research considered the usage of a reflective modulator at the RAU. In this way, laser light from the CO is used for the uplink path back to the CO by modulating the reflected light. In this section we construct a reflective Electro-Absorption Modulator (EAM) and combine it with a variant of the LNA used in the photoreceiver.

### 2.6.1 Reflective EAM Modulator

The modulator adopted in this dissertation is an EAM from the iSiPP50G platform. A first step in designing the dedicated driver for the EAM consists of knowing the input impedance of the modulator seen by the driver. A 495 pH wirebond inductance should again be assumed due to a similar electro-optical interface between EAM and driver as was the case in the photoreceiver in section 2.5. The resulting impedance of the EAM-wirebond combination is voltage dependent and shown in table 2.4 in function of reverse EAM bias.

Voltage	Input impedance
0V	47.6-j44.9 $\Omega$
1V	48.5-j63.1 $\Omega$
2V	49.9-j68.9 $\Omega$
3V	50.0-j73.7 $\Omega$

Table 2.4: Input impedance EAM-wirebond combination at 28.5 GHz.

Furthermore, to get an idea of the modulation characteristics of the EAM, the insertion loss of the modulator was measured in function of the reverse EAM bias. These static insertion loss curves are shown in Fig. 2.18 for different operation wavelengths. To get a combination of low insertion loss and large modulation depth the optimal wavelength range of operation will be between 1550 and 1570 nm.

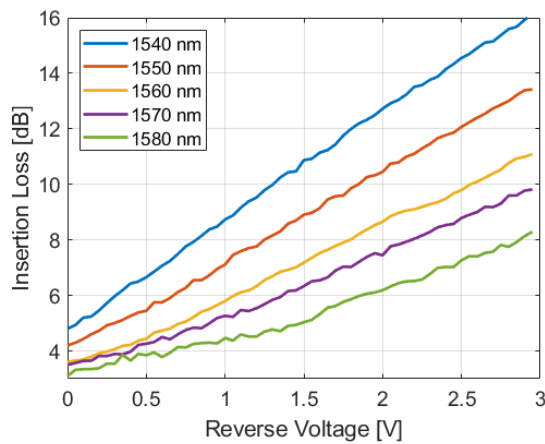


Figure 2.18: Static insertion loss of the standalone EAM.

Making a reflective variant of the EAM can be done easily by adding an on-chip mirror at the output of the modulator. In this dissertation, the mirror was constructed by using a 3 dB splitter where both outputs are interconnected. This can be done easily in silicon photonics due to the possibility to add bends with a small radius because of the high index contrast of the Silicon on Insulator (SOI) platform. Two variants of the reflective modulator were considered. First the EAM was positioned in front of the mirror (Fig. 2.19). In a second structure the EAM is placed in the mirror as shown in Fig. 2.20. In this dissertation, the second variant was chosen as this allows for a lower insertion loss of the reflective modulator due to single passage of the EAM.

*The combination of driver and reflective EAM in the mirror will from this point on be referred to as DEIM (Driver and EAM In Mirror) and is the device that is used for the system experiments.*

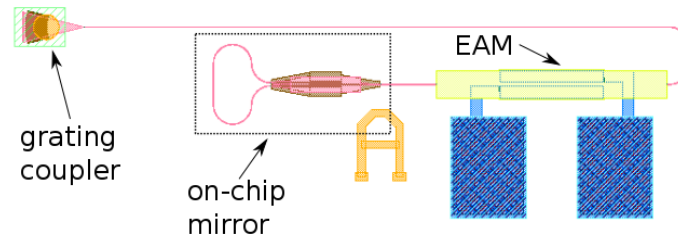


Figure 2.19: Reflective modulator: EAM in front of mirror.

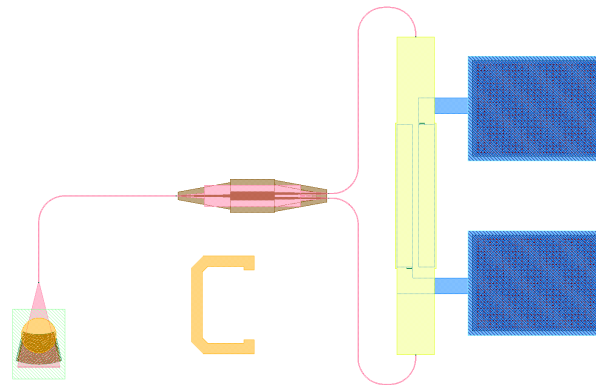


Figure 2.20: Reflective modulator: EAM in mirror.

### 2.6.2 Driver Design

The driver should operate in the same RF band as the photoreceiver. Consequently, design effort can be minimized by reusing the same core design as the LNA block. The amplifier in the photoreceiver cannot be re-used immediately as an EAM driver and therefore a second generation amplifier was designed based on the design of the original LNA. The detailed schematic of the EAM driver is shown in Fig. 2.22. The second generation amplifier differs from the first generation in the following ways:

- **Internal bias tee at the output:** To enable on-chip biasing of the EAM, an internal bias tee was added as part of the output matching network of the LNA.
- **New I/O impedance matching:** Since the source and load impedance connected to the amplifier will be different compared to the LNA in the photoreceiver, input and output matching networks were re-

designed. The new source impedance is  $50 \Omega$  while the new load impedance is based on the input impedance of the wirebond-EAM combination discussed in table 2.4:  $48.5-j63.1 \Omega$  at 1V reverse bias.

- **GSG pads:** To accommodate different probing schemes, the original GS pads were replaced with GSG pads.

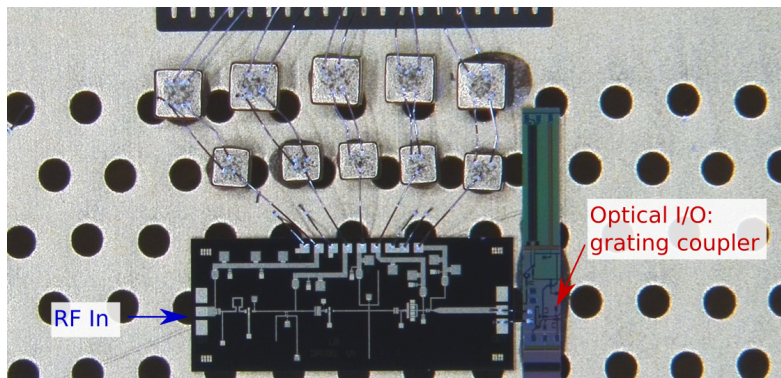


Figure 2.21: DEIM assembly.

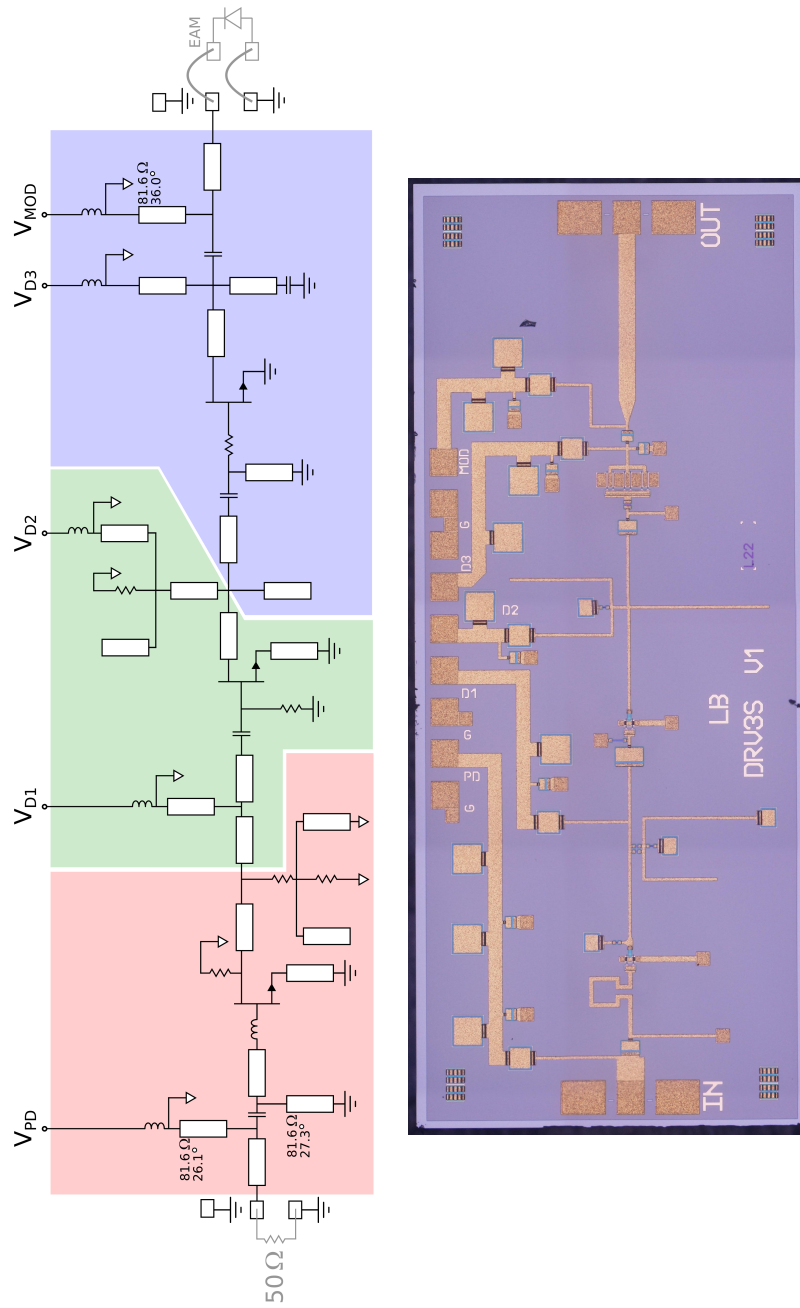


Figure 2.22: 3-stage mmWave EAM driver: (top) Schematic; (bottom) Microscope picture.

### 2.6.3 Driver Performance

In this chapter, the DEIM combination is characterized as a standalone device. The data transmission experiments are presented in chapter 5.

#### 2.6.3.1 Small Signal Behavior

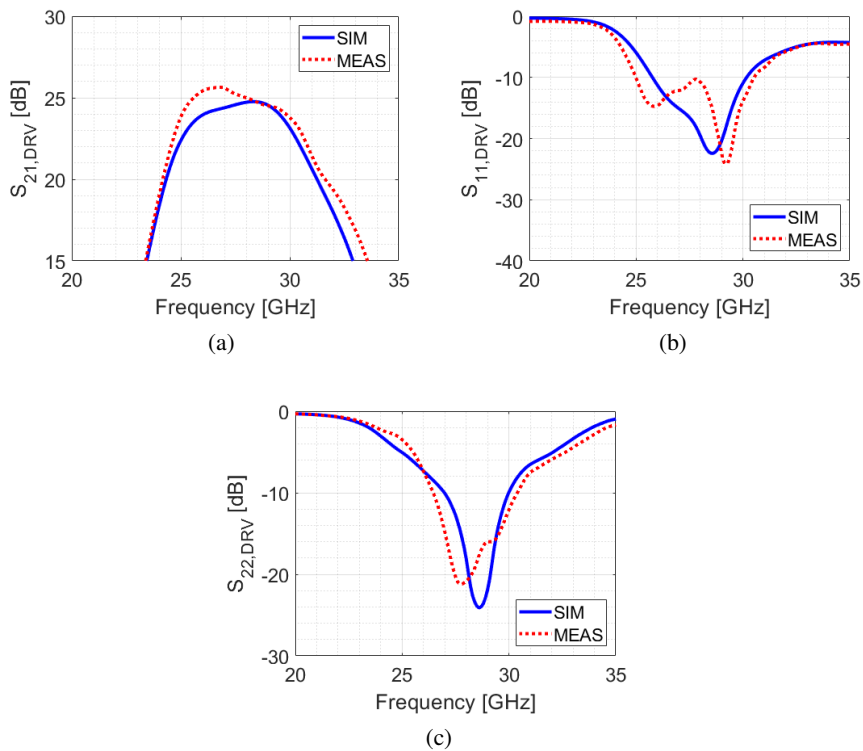


Figure 2.23: EAM driver S-parameters: Simulations and measurements.

The small signal behavior is determined in a similar way as for the LNA. First, the device is measured in a  $50 \Omega$  environment and subsequently the obtained S-parameters are transformed for the desired interface impedances:  $50 \Omega$  at the input, wirebond and EAM at the output. The resulting S-parameters are shown in Fig. 2.23 together with the simulated data for a 2V driver supply. There is again no noticeable difference for the small signal behavior of the driver when the driver supply is increased to 3V. When looking at the input reflection coefficient  $S_{11}$ , a similar remark as for the

LNA can be made. Figure 2.23(b) indicates a significant difference between the measured and simulated data. However, when the reflection coefficient is looked at on the Smith chart (Fig. 2.24) it is clear that measured and simulated  $S_{11}$  show a similar behavior.

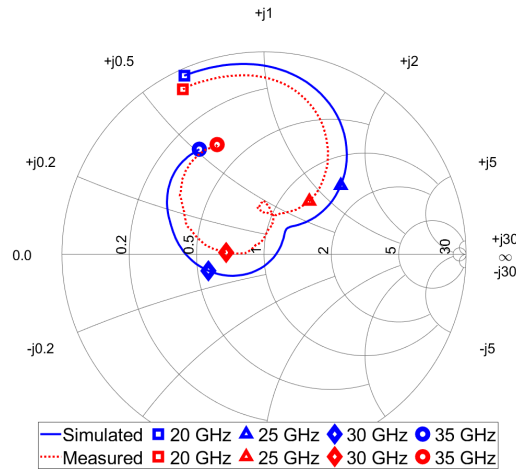


Figure 2.24:  $S_{11}$  of the driver shown on the Smith chart ( $50 \Omega$  reference).

Figure 2.23(a) shows that the measured  $S_{21}$  ranges from 25.2 to 24.3 dB in the 27.5 to 29.5 GHz range. The measured 3-dB cut-off frequencies are situated at 24.7 and 30.6 GHz. Input and output return loss stay below -10.3 and -15.2 dB respectively in the 27.5 – 29.5 GHz range and the -10 dB return loss bandwidth covers 25.0 to 30.5 GHz at the input and 26.5 to 30.4 GHz at the output.

Subsequently, the transfer function of the Driver and EAM In Mirror (DEIM) transmitter was measured as part of an ARoF link (Fig. 2.25). The laser generates a Continuous Wave (CW) tone which enters the PIC via a grating coupler and this tone is modulated at the EAM by the RF signal present at the output of the driver. Since the EAM is reflective, the modulated light comes back through the same grating coupler and is separated from the CW laser light by the use of an optical circulator. Next, an EDFA-VOA pair is used to enable setting the output power to an arbitrary value. In this way, we can isolate the effect of the light modulation from the variations on the strength of the optical signal. Finally, a high speed detector is used to convert back to the electrical domain. The receiver used for this experiment is the XPDV3120R 70 GHz photodetector which ensures that

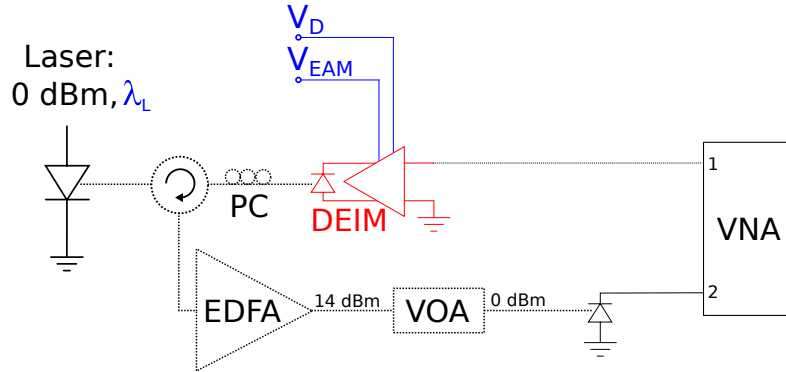


Figure 2.25: Setup for  $S_{21}$  characterization of the DEIM – PC: Polarization Controller; EDFA: Erbium Doped Fiber Amplifier; VOA: Variable Optical Attenuator; ESA: Electrical Spectrum Analyzer.

frequency dependent effects of the link can be attributed to the transmitter and in this way the  $S_{21,DEIM}$  of the transmitter can be characterized. Before discussing the results, it should be mentioned that the measurements were performed under the presence of index matching gel between the fiber tip and the grating coupler. If such a gel is not present the flat glass-air interface of the fiber tip will result in reflections with optical power levels of a similar order of magnitude as the modulated light. This would result in interference effects that fluctuate heavily and thus result in unreliable link measurements. When such an index matching gel is present, the fiber angle used for probing the grating coupler should be changed accordingly.

Measurements of the  $S_{21,DEIM}$  at different wavelengths are shown in Fig. 2.26. Altering the EAM bias will not only change its E/O behavior but will also change the output matching of the driver and therefore the EAM bias is fixed in Fig. 2.26. Since an EDFA-VOA combination was used to set the optical power incident on the photodetector, these differences are due to changes in modulation depth. It is clear that the modulation depth decreases when increasing the operation wavelength from 1550 to 1570 nm. This is due to the reduced slope in the electro-optic transfer function (Fig. 2.18). Nevertheless, the normalized transfer function appears to be independent of the wavelength for the measured wavelength range. Unfortunately, a decrease in bandwidth can be seen compared to the standalone driver. Whereas the 3-dB bandwidth of the driver ranges between 24.7 and 30.6 GHz, the DEIM transmitter results in a 3-dB bandwidth between 24.4 and 29.5 GHz. This bandwidth reduction might be caused by an increased

wirebond inductance and/or bandwidth limitations in the electro-optic conversion of the modulator. To conclude this discussion on the small signal behavior of the transmitter, it can be seen that even without additional electrical amplification a link gain of close to 0 dB can be achieved when 0 dBm optical power is incident on a photodetector.

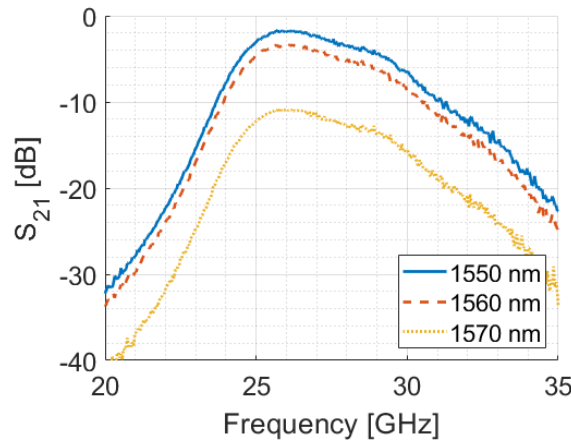


Figure 2.26: Transfer function DEIM transmitter (2V driver supply, 1V EAM bias).

### 2.6.3.2 Linearity

For the LNA in the photoreceiver, it was discussed that the device shows increased linearity and power consumption over the simulated values due to process variations on the threshold of the pHEMT transistors. Threshold voltages for the driver are closer to the nominal values resulting in respectively 124 and 247 mW power consumption for 2V and 3V drain supply. The standalone driver shows an OIP3 of 20.6 dBm at 2V drain and 24.8 dBm at 3V drain, measured in a 50  $\Omega$  environment. When the driver supply is 2V, the maximum PAE (eq. 2.16) is 20.0%. Furthermore, the PAE at the 1 dB compression level is 9.7% for this low-power setting. When the driver supply is 3V, the maximum PAE increases to 20.1%. Furthermore, the PAE at the 1 dB compression level increases to 11.6% for this high-linearity setting.

Unfortunately, the linearity of the transmitter will in practice be determined by the EAM. Consequently, the input referred 1dB compression point was measured for the DEIM transmitter by using the ARoF setup shown in Fig.

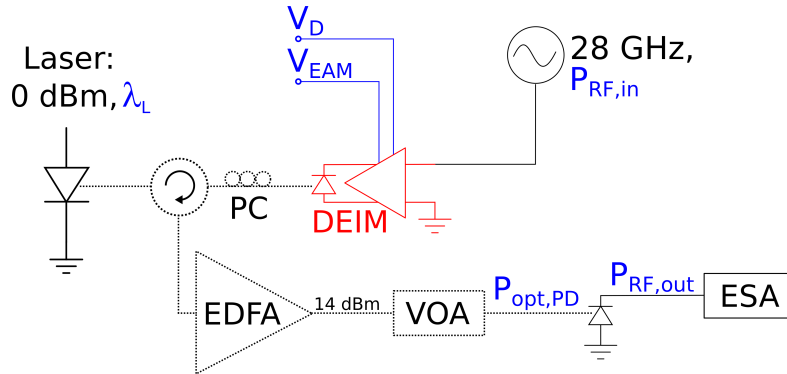


Figure 2.27: Setup for 1dB compression measurement of the transmitter – PC: Polarization Controller; EDFA: Erbium Doped Fiber Amplifier; VOA: Variable Optical Attenuator; ESA: Electrical Spectrum Analyzer.

2.27. Table 2.5 shows the input referred 1dB compression point of  $P_{RF,in}$  for different wavelengths and different EAM bias levels while using a 3V drain supply for the driver and with the optical power incident on the photodetector  $P_{opt,PD}$  equal to 0 dBm. Further experiments show that the input referred 1 dB compression point does not shift by changing the received optical power to e.g. -5 dBm, which indicates that the link linearity in the measurement setup is not limited by the receiver. Additionally, it was verified that reducing the driver supply to 2V does not noticeably influence the linearity. Consequently, the EAM rather than the driver is limiting the linearity of the transmitter. Based on table 2.5, we can conclude that the linearity in the wavelength range of interest improves for increasing reverse bias of the EAM. However, stronger reverse biasing also increases insertion loss and results in increased reflections at the output of the driver due to changes in the load impedance.

	$\lambda_L = 1550 \text{ nm}$	$\lambda_L = 1560 \text{ nm}$	$\lambda_L = 1570 \text{ nm}$
$V_{EAM} = 0.5V$	-26 dBm	-25 dBm	-23 dBm
$V_{EAM} = 1V$	-24 dBm	-24 dBm	-22 dBm
$V_{EAM} = 2V$	-20 dBm	-23 dBm	-20 dBm
$V_{EAM} = 3V$	-18 dBm	-21 dBm	-16 dBm

Table 2.5: DEIM transmitter input referred 1dB compression point – 28 GHz;  $V_D = 3V$ ;  $P_{opt,PD} = 0 \text{ dBm}$

### 2.6.3.3 Noise

Since the amplification part of the driver circuit is unaltered relative to the photoreceiver, a similar value for the noise figure is to be expected. Simulated noise figure values can be found in Fig. 2.28 where the noise figure is found to range between 2.03 and 2.15 dB for a 2 V drain supply and between 2.17 and 2.26 dB for a 3 V drain supply when looking at the 27.5 to 29.5 GHz frequency range. Differences between the simulated noise figures of the LNA and driver are small and can be attributed to losses in the input matching network which differs for both amplifiers.

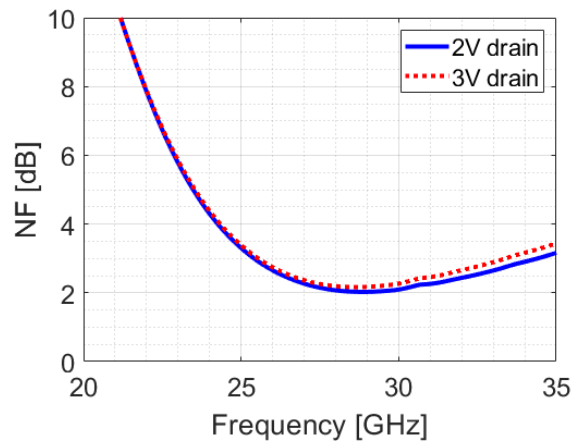


Figure 2.28: Simulated noise figure of the driver for 2 and 3V drain supply.

## 2.7 Conclusion

Good signal quality requires a strong signal and low noise in the link. Since the wireless path results in significant path loss, especially at mmWave frequencies, further amplification is required. Furthermore, this amplification should introduce a minimal amount of noise to make sure that no significant SNR degradation occurs. In this chapter, electrical amplification is looked at.

Traditional optical receiver schemes rely on TIAs to amplify the output signal of the photodetector. In this dissertation, the narrowband nature of wireless communication schemes is taken into account to optimize the performance of the devices. In a first solution, a TIA with input series inductive

peaking is used to relax the transimpedance limit and consequently achieve a higher transimpedance gain in a narrow frequency range. Secondly, a photoreceiver was designed where the narrowband nature was taken into account from the start. The devised photoreceiver comprises a Ge-on-Si photodetector and co-designed GaAs low noise amplifier offering 24 dB gain, corresponding to 224V/W external conversion gain, over a 3-dB bandwidth between 23.5 and 31.5 GHz. The associated noise figure is 2.1 dB and an output referred third order intercept point up to 26.5 dBm can be obtained with a power consumption of 303 mW.

Subsequently, the uplink was looked at. To avoid the need for lasers in the remote antenna units, a reflective EAM was devised. Narrowband amplification was introduced by redesigning the GaAs LNA from the aforementioned photoreceiver to enable the modulator driving in the 28 GHz frequency range. Main differences with the LNA of the photoreceiver are the redesign of the input and output matching network and additionally the introduction of an internal bias tee at the output of the driver to enable biasing of the EAM. The devised EAM driver offers 25.2 dB gain, over a 3-dB bandwidth between 24.4 and 29.5 GHz, and a noise figure of 2.0 dB. The linearity of the driver-EAM combination depends heavily on the operation wavelength and EAM bias. Since the EAM is the limiting factor in the linearity of the transmitter, the drain supply of the driver can be set to 2V without loss of linearity resulting in 124 mW power consumption.



## References

- [1] 5G-PHOS, *Deliverable D2.1 Initial Report on Use Cases, System Requirements, KPIs and Network Architecture*, May 2018.
- [2] G. P. Agrawal, *Fiber-Optic Communication Systems*, 1st ed. Wiley, 2005.
- [3] G. Kalfas, C. Vagionas, A. Antonopoulos, E. Kartsakli, A. Mesodiakaki, S. Papaioannou, P. Maniotis, J. S. Vardakas, C. Verikoukis, and N. Pleros, "Next Generation Fiber-Wireless Fronthaul for 5G mmWave Networks," *IEEE Communications Magazine*, vol. 57, no. 3, pp. 138–144, March 2019.
- [4] C. G. H. Roeloffzen, M. Hoekman, E. J. Klein *et al.*, "Low-Loss Si<sub>3</sub>N<sub>4</sub> TriPLeX Optical Waveguides: Technology and Applications Overview," *IEEE Journal of Selected Topics in Quantum Electronics*, vol. 24, no. 4, July/August 2018.
- [5] Y. A. Al-Jawhar, K. N. Ramli, A. Mustapha, S. A. Mostafa, N. S. Mohd Shah, and M. A. Taher, "Reducing PAPR With Low Complexity for 4G and 5G Waveform Designs," *IEEE Access*, vol. 7, pp. 97 673–97 688, July 2019.
- [6] X. Gu, D. Liu, C. Baks, O. Tageman, B. Sadhu, J. Hallin, L. Rexberg, and A. Valdes-Garcia, "A Multilayer Organic Package with 64 Dual-Polarized Antennas for 28GHz 5G Communication," in *IEEE MTT-S International Microwave Symposium (IMS)*, 2017.
- [7] 3GPP, *TR 38.815: New Frequency Range for NR (24.25 - 29.5 GHz) - Release 15*, v. 15.0.0, 2018.
- [8] Y. Huo, X. Dong, and A. W. Xu, "5G Cellular User Equipment: From Theory to Practical Hardware Design," *IEEE Access*, vol. 5, pp. 13 992–14 010, July 2017.
- [9] M. Pantouvaki, S. A. Srinivasan, Y. Ban, P. De Heyn, P. Verheyen, G. Lepage, H. Chen, J. De Coster, N. Golshani, S. Balakrishnan,

- P. Absil, and J. Van Campenhout, “Active Components for 50 Gb/s NRZ-OOK Optical Interconnects in a Silicon Photonics Platform,” *Journal of Lightwave Technology*, vol. 35, no. 4, pp. 631–638, February 2017.
- [10] L. Bogaert, H. Li, K. Van Gasse, J. Van Kerrebrouck, J. Bauwelinck, G. Roelkens, and G. Torfs, “36 Gb/s Narrowband Photoreceiver for mmWave Analog Radio-over-Fiber [Early Access],” *Journal of Lightwave Technology*, 10.1109/JLT.2020.2968149.
- [11] E. Säckinger, “The Transimpedance Limit,” *IEEE Transactions on Circuits and Systems – I: Regular Papers*, vol. 57, no. 8, pp. 1848–1856, August 2010.
- [12] A. Leven, V. Hurm, R. Reuter, and J. Rosenzweig, “Design of Narrow-Band Photoreceivers by Means of the Photodiode Intrinsic Conductance,” *IEEE Transactions on Microwave Theory and Techniques*, vol. 49, no. 10, pp. 1908–1913, October 2001.
- [13] E. Säckinger, *Broadband Circuits for Optical Fiber Communication*, 4th ed. Wiley, 2010.
- [14] L. Bogaert, J. V. Kerrebrouck, A. Abbasi, J. Lambrecht, G. Torfs, X. Yin, G. Roelkens, and J. Bauwelinck, “Resonant optical receiver design by series inductive peaking for sub-6 GHz RoF,” *Microwave and Optical Technology Letters*, vol. 59, no. 9, pp. 2279–2284, June 2017.
- [15] V. J. Urick, K. J. Williams, and J. D. McKinney, *Fundamentals of Microwave Photonics*, 1st ed. Wiley, 2015.
- [16] A. Agarwal and J. H. Lang, *Foundations of Analog and Digital Electronic Circuits*, 1st ed. Elsevier, 2005.
- [17] L. Bogaert, H. Li, K. Van Gasse, J. Van Kerrebrouck, J. Bauwelinck, G. Roelkens, and G. Torfs, “Narrowband photoreceiver for analog radio-over-fiber in the 24.25-29.5 GHz band,” in *45th European Conference on Optical Communication (ECOC)*, 2019, M.2.C.2.
- [18] T. Cameron, “Bits to beams – rf technology evolution for 5g mmwave radios,” *Microwave Journal*, November 2018.
- [19] T. Cameron (Analog Devices), *RF Technology for the 5G Millimeter Wave Radio*, May 2016.

- [20] G. Ghione, *Semiconductor Devices for High-Speed Optoelectronics*, 1st ed. Cambridge University Press, 2009.
- [21] B. Debaillie, A. Visweswaran, T. Maiwald, K. Schneider, A. Karakuzulu, D. Ferling, and K. Aufinger, "Can the rf radio foster the 140 ghz spectrum?" in *European Microwave Week (EuMW)*, 2019, WS-01.09.
- [22] C. Teyssandier, H. Stieglauer, E. Byk, A. Couturier, P. Fellon, M. Camiade, H. Blanck, and D. Floriot, "0.1 $\mu$ m gaas pHEMT technology and associated modelling for millimeter wave low noise amplifiers," in *7th European Microwave Integrated Circuit Conference (EuMIC)*, October 2012, pp. 171–174.
- [23] C. S. Walker, *Capacitance, Inductance and Crosstalk Analysis*, 1st ed. Artech House, 1990.
- [24] D. D. Henkes, "A design tool for improving the input match of low noise amplifiers," *High Frequency Electronics*, vol. 6, no. 2, pp. 54–64, February 2007.
- [25] K. Kurokawa, "Power waves and the scattering matrix," *IEEE Transactions on Microwave Theory and Techniques*, vol. 13, no. 2, pp. 194–202, March 1965.
- [26] L. Besser and R. Gilmore, *Practical RF Circuit Design for Modern Wireless Systems – Volume I: Passive Circuits and Systems*, 1st ed. Artech House, 2003.
- [27] C. H. Cox III, *Analog Optical Links: Theory and Practice*, 1st ed. Cambridge University Press, 2004.
- [28] A. Leven, V. Hurm, R. Reuter, and J. Rosenzweig, "Design of Narrow-Band Photoreceivers by Means of the Photodiode Intrinsic Conductance," *IEEE Transactions on Microwave Theory and Techniques*, vol. 49, no. 10, pp. 1908–1913, October 2001.
- [29] A. Miras-Legros, E. Legros, L. Giraudet, G. Wanlin, S. Vuye, and C. Joly, "Very high gain, high sensitivity, 40 ghz narrowband photoreceiver for clock recovery," *Electronics Letters*, vol. 34, no. 3, pp. 297–299, February 1998.
- [30] S. Fedderwitz, C. C. Leonhardt, J. Honecker, P. Müller, and A. G. Steffan, "A high linear and high power photoreceiver suitable for analog applications," in *IEEE Photonics Conference*, September 2012, pp. 308–309.

- [31] A. Umbach, T. Engel, H.-G. Bach, S. van Waasen, E. Dröge, A. Strittmatter, W. Ebert, W. Passenberg, R. Steingrüber, W. Schlaak, G. G. Mekonnen, G. Unterbörsch, and D. Bimberg, “Technology of InP-Based 1.55- $\mu\text{m}$  Ultrafast OEMMIC’s: 40-Gbit/s Broad-Band and 38/60-GHz Narrow-Band Photoreceivers,” *IEEE Journal of Quantum Electronics*, vol. 35, no. 7, pp. 1024–1031, July 1999.
- [32] T. Umezawa, K. Kashima, A. Kanno, A. Matsumoto, K. Akahane, N. Yamamoto, and T. Kawanishi, “100-ghz fiber-fed optical-to-radio converter for radio- and power-over-fiber transmission,” *IEEE Journal of Selected Topics in Quantum Electronics*, vol. 23, no. 3, May 2017.
- [33] B. Cui and J. R. Long, “A 1.7-db minimum nf, 22–32-ghz low-noise feedback amplifier with multistage noise matching in 22-nm fd-soi cmos,” *IEEE Journal of Solid-State Circuits*, vol. 55, no. 5, pp. 1239–1248, May 2020.
- [34] M. Elkholy, S. Shakib, J. Dunworth, V. Aparin, and K. Entesari, “A wideband variable gain lna with high oip3 for 5g using 40-nm bulk cmos,” *IEEE Microwave and Wireless Components Letters*, vol. 28, no. 1, pp. 64–66, January 2018.
- [35] P. Qin and Q. Xue, “Compact wideband lna with gain and input matching bandwidth extensions by transformer,” *IEEE Microwave and Wireless Components Letters*, vol. 27, no. 7, pp. 657–659, July 2017.
- [36] M.-H. Tsai, S. S. H. Hsu, F.-L. Hsueh, C.-P. Jou, and T.-J. Yeh, “A 17.5–26 ghz low-noise amplifier with over 8 kv esd protection in 65 nm cmos,” *IEEE Microwave and Wireless Components Letters*, vol. 22, no. 9, pp. 483–485, September 2012.
- [37] A. A. Nawaz, J. D. Albrecht, and A. C. Ulusoy, “A ka/v band-switchable lna with 2.8/3.4 db noise figure,” *IEEE Microwave and Wireless Components Letters*, vol. 29, no. 10, pp. 662–664, October 2019.
- [38] B.-W. Min and G. M. Rebeiz, “Ka-band sige hbt low noise amplifier design for simultaneous noise and input power matching,” *IEEE Microwave and Wireless Components Letters*, vol. 17, no. 12, pp. 891–893, December 2007.
- [39] M. El-Nozahi, E. Sanchez-Sinencio, and K. Entesari, “A millimeter-wave (23–32 ghz) wideband bicmos low-noise amplifier,” *IEEE Journal of Solid-State Circuits*, vol. 45, no. 2, pp. 289–299, February 2010.

- 
- [40] A. Stohr, T. Kuri, K. Kitayama, R. Heinzelmann, and D. Jager, "Full-duplex 60 ghz fibre optic transmission," *Electronics Letters*, vol. 35, no. 19, pp. 1653–1655, September 1999.
- [41] B. Zhu, S. Pan, D. Zhu, and J. Yao, "Wavelength reuse in a bidirectional radio-over-fiber link based on cross-gain and cross-polarization modulation in a semiconductor optical amplifier," *Optics Letters*, vol. 38, no. 18, pp. 3496–3498, September 2013.
- [42] Z. Tang and S. Pan, "A full-duplex radio-over-fiber link based on a dual-polarization mach–zehnder modulator," *IEEE Photonics Technology Letters*, vol. 28, no. 8, pp. 852–855, April 2016.
- [43] Z. Jia, J. Yu, and G. Chang, "A full-duplex radio-over-fiber system with 2.5gbit/s data symmetric delivery over 40km smf-28," in *European Conference on Optical Communications (ECOC)*, 2006, Tu1.6.3.



# 3

## High Linearity Optoelectronic Conversion

### 3.1 Optical Amplification

Amplification of the RF signal is required to overcome the large path losses caused by the Analog Radio over Fiber (ARoF) and wireless link. In chapter 2, the signal is boosted by amplifying the electrical signal at the Remote Antenna Unit (RAU) in between the photodetector and the antenna.

Centralization will be important to keep next-generation wireless architectures cost-effective and therefore shared optical amplification (Fig. 3.1) at the Central Office (CO) is considered in chapter 3 as this enables further reduction of the cost and complexity at the RAU. A comparison of the system performance for optical and electrical amplification architectures is provided in section 3.2. One of the main challenges of adopting an optical amplification scheme is the introduction of more stringent requirements on the linearity of the optical components. In this chapter, we will focus on improving the linearity of the Photodetectors (PDs).

Chapter 3 starts by describing the adopted standalone Ge-on-Si photodetector in section 3.3. Subsequently, two solutions for improving the linearity of the photodetector are covered. First, traveling wave photodiodes are discussed in section 3.4. Such a Traveling Wave Photodetector (TWPD) is based on a transmission line design and provides broadband linearity im-

provements. For narrowband communication, impedance matching can be used as an alternative. This scenario is covered in section 3.5.

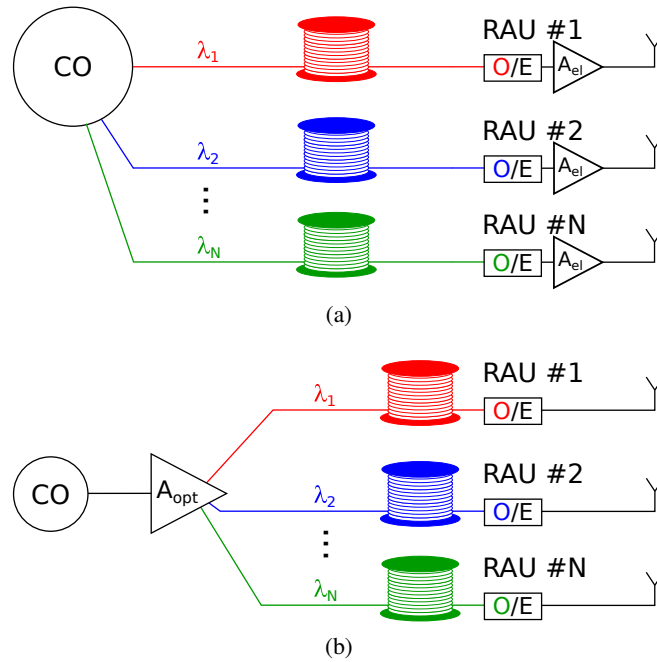


Figure 3.1: Amplification implemented as (a) Electrical amplification at RAU (b) Optical amplification at CO.

## 3.2 Impact on system performance: optical versus electrical amplification

### 3.2.1 Gain

When a photodetector is operating in its linear regime, the generated output current will scale linearly with the incoming optical power. Consequently, the electrical power at the output of the photodetector scales quadratically with the incoming optical power. Hence, it is clear that to provide an equivalent electrical amplification of  $x$  dB, the optical amplifier only needs to provide  $x/2$  dB. When the Low Noise Amplifier (LNA) designed in chapter 2 is taken as an example (24 dB gain), one can see that to push this amplification to the optical domain, an optical amplifier with 12 dB gain is

required. This is easily achieved, both with an Erbium Doped Fiber Amplifier (EDFA) as well as a semiconductor optical amplifier (SOA).

### 3.2.2 Cost and Power Consumption

A quantitative comparison of cost and power consumption will depend heavily on the exact implementation choices. However, it is clear that for electrical amplification at the remote antenna unit, these values will scale linearly with the number of RAUs in the system. Centralized optical amplification, on the other hand, has the benefit of enabling shared amplification functionality for multiple RAUs. Consequently, the cost and power consumption remains nearly independent of the number of RAUs with the added benefit of an architecture which allows for more centralized maintenance.

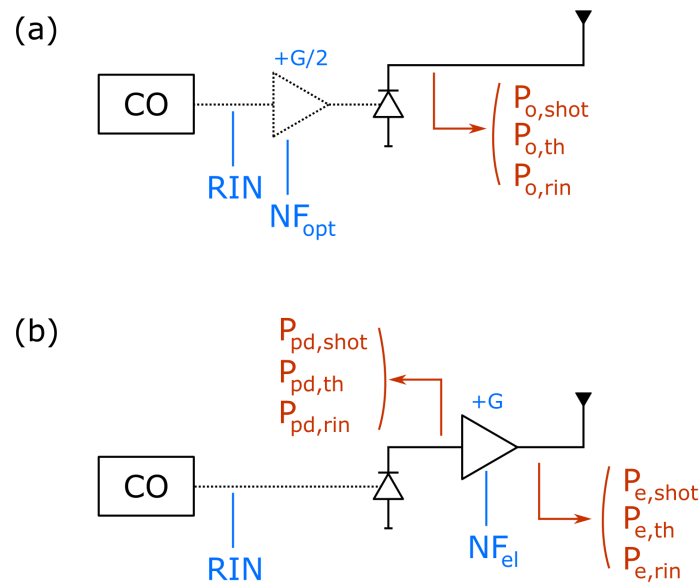


Figure 3.2: Schematic representation of the different noise contributions: (a) optical amplification; (b) electrical amplification.

### 3.2.3 Noise

Four important noise contributions should be considered when comparing the two architectures: shot noise, thermal noise, relative intensity noise and amplifier induced noise [1]. Amplifier induced noise sources differ between

optical and electrical amplification schemes in the sense that the electrical amplifier noise can be seen as a penalty compared to the thermal noise contribution while the optical amplifier noise can be seen as a penalty to the shot noise contribution, and they will therefore be treated accordingly. In figure 3.2, a schematic representation of the different noise contributions is shown. It should be noted that to obtain the same link gain, the equivalent optical gain in dB should only be half the electrical gain in dB, as explained before.

### 3.2.3.1 Thermal Noise

The thermal noise power (eq. 3.1, [1]) at the output of the photodetector is independent of the presence of an optical amplifier. In equation 3.1,  $k_B$  denotes the boltzman constant and T is the absolute temperature expressed in Kelvin. In the electrical amplification scheme, thermal noise at the output of the photodetector is subsequently amplified. Furthermore, this electrical amplification is not ideal and introduces an additional noise penalty  $NF_{el}$ . Hence, the electrical amplification scheme ultimately results in a larger thermal noise contribution (equations 3.2 and 3.3).

$$P_{pd,th}[dBm] = 10 \times \log_{10}(k_B T \Delta f \times 1000) \quad (3.1)$$

$$P_{o,th}[dBm] = P_{pd,th}[dBm] \quad (3.2)$$

$$\begin{aligned} P_{e,th}[dBm] &= P_{pd,th}[dBm] + G[dB] + NF_{el}[dB] \\ &> P_{o,th} \end{aligned} \quad (3.3)$$

### 3.2.3.2 Shot Noise

Shot noise (eq. 3.4, [1]) on the other hand depends on the presence of optical amplification. Firstly, because the shot noise power depends on the DC current generated by the photodetector and secondly because the noise penalty of an optical amplifier is referred to shot noise limited links. In equation 3.4,  $q$  denotes the elementary charge,  $R_s$  the resistive part of the photodetector impedance and  $I_D$  the DC current generated by the photodetector in the absence of optical amplification. The Noise Figure (NF) of an optical amplifier has a theoretical lower boundary of 3 dB and is in practice typically 5 dB for EDFAs and 8 dB for SOAs. While the relative comparison between shot noise in electrical and optical amplification schemes

depends on the values of  $G$  and  $NF_{opt}$ , this contribution will in general be lower for the optical amplification scheme (equations 3.5 and 3.6).

$$P_{pd,shot}[dBm] = 10 \times \log_{10}(2qI_D R_s \Delta f \times 1000) \quad (3.4)$$

$$P_{o,shot}[dBm] = P_{pd,shot} + G[dB]/2 + NF_{opt}[dB] \quad (3.5)$$

$$P_{e,shot}[dBm] = P_{pd,shot} + G[dB] \quad (3.6)$$

### 3.2.3.3 Relative Intensity Noise

Relative intensity noise power (eq. 3.7, [1]) scales linearly with the RIN of the laser in the central office and quadratically with the DC current  $I_D$  generated by the photodetector. Therefore, this contribution will end up to be equal for optical and electrical amplification schemes (equations 3.8 and 3.9).

$$P_{pd,rin}[dBm] = 10 \times \log_{10}(RIN \times I_D^2 R_s \Delta f \times 1000) \quad (3.7)$$

$$P_{o,rin}[dBm] = P_{pd,rin} + G[dB] \quad (3.8)$$

$$\begin{aligned} P_{e,rin}[dBm] &= P_{pd,rin}[dBm] + G[dB] \\ &= P_{o,rin} \end{aligned} \quad (3.9)$$

### 3.2.4 Linearity

To be able to implement the amplification in the optical domain, the linearity in three optical components is critical: photodetector, optical amplifier and fiber. The third aspect (i.e. non-linearities in the fiber) is important when the optical amplification is centralized. It can be found that stimulated Brillouin scattering (SBS, [2]) severely limits the launch power, even at relatively short fiber lengths. For typical fiber lengths of a few kilometres this effect limits power levels in Standard Single Mode Fiber (SSMF) to about 10 dBm.

When the goal is to replace the photoreceiver discussed in chapter 2 by an equivalent optical amplification architecture, it is required to end up with a photodetector that offers the same power handling as the photoreceiver. Consequently, the requirements on the linearity of the photodetector will

be significantly higher in the optical amplification scheme than in the electrical amplification scheme. Since the Output referred third order Intercept Point (OIP3) of the photoreceiver devised in this dissertation lies between 22.2 and 26.5 dBm, this results in the need for photodetector structures with similar power handling capabilities. The design of such high-linearity photodetectors will be the focus of this chapter.

Finally, also the optical amplifier needs to be able to handle such high power levels linearly. The photoreceiver has a maximum 1 dB compression point of 13.9 dBm, and this translates to a peak-to-peak current of 62.7 mA<sub>pp</sub> when assuming no electrical amplification is present and a 50 Ω load is targeted. For a responsivity of 0.8 A/W and a modulation depth of 50%, the maximum optical power level incident on the photodetector is 117.6 mW. Hence, the optical amplifier needs to be capable to deliver optical powers of about 20.7 dBm and in the presence of optical losses (e.g. grating couplers and/or fiber), insertion loss will add directly to the linearity requirements of the optical amplifier. Hence, the need for high-linearity components might limit the practicality of optical amplification architectures.

### 3.2.5 Conclusion

Optical amplification enables a reduction in noise and offers the possibility to share resources when the amplification is centralized. The latter can give rise to potential cost and power consumption savings. Unfortunately, the main challenge in deploying such a centralized optical amplification scheme concerns the need for high-linearity optical components (optical amplifier, detector and fiber). In this chapter the focus is directed to the design and testing of such high-linearity photodetectors.

## 3.3 Fundamentals of a Germanium Photodetector

The traveling wave photodetector and resonantly matched photodetector discussed in sections 3.4 and 3.5 are designed in the iSiPP platform of imec (Fig. 3.3). This is a silicon photonics platform that leverages the efforts put into the CMOS industry, as discussed in section 1.3. Compatibility with standardized CMOS manufacturing is obtained by making use of monolithically integrated Germanium PDs rather than heterogeneously integrated III-V photodetectors [3].

The photodetector used in this chapter is a Germanium on Silicon vertical p+(Ge)-i(Ge)-n+(Si) photodetector optimized for C-band operation (Fig. 3.4). This device offers a responsivity of 0.8 A/W, a 3dB bandwidth over 50 GHz and a dark current around 80 nA under a 2V reverse bias. Lateral

pin PDs with contact plugs to the Silicon layer have the potential to offer a better trade-off between bandwidth and responsivity while resulting in a lower dark current [4], but were not yet available in the Process Design Kit (PDK) at the time of the TWPD design.

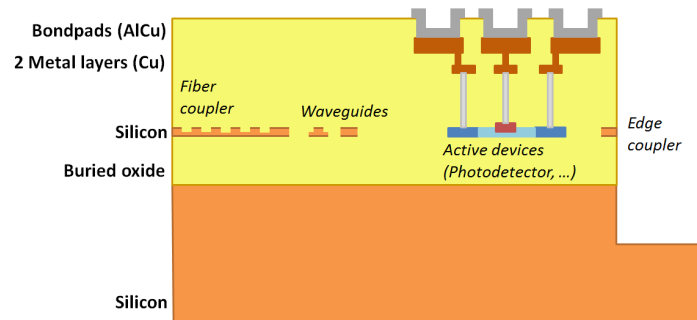


Figure 3.3: Stack of the iSiPP50G platform [5, 6].

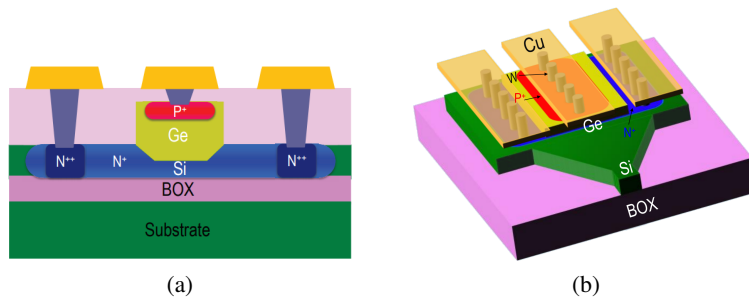


Figure 3.4: Vertical PIN Ge-on-Si photodetector (a) Cross-section view (b) 3D view [7].

### 3.3.1 Small Signal Behavior

The target of improving the power handling capabilities of the Optoelectronic (O/E) conversion process can be divided in two separate conditions. On the one hand, the detector should be able to generate as much power as possible. On the other hand, it is important to get an optimal power transfer from the detector to the load. In the TWPD the latter is taken into account in the transmission line design while the resonantly matched photodetector incorporates an LC matching network to get impedance matching around

the RF carrier frequency. To this end a good knowledge of the electrical behavior of the photodetector is required.

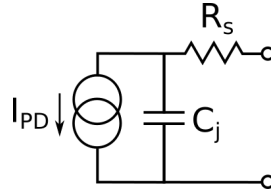


Figure 3.5: Simple pin photodetector model [8].

A simple equivalent model to describe the photodetector (Fig. 3.5) consists of a parallel combination of a current source  $I_{PD}$  and a junction capacitance  $C_j$ . Losses of the photodetector are modelled by adding a resistance  $R_s$  in series with this parallel combination. The value of  $R_s$  will be independent of the applied voltage while  $C_j$  tends to decrease when increasing the reverse bias of the photodetector. The current generated by the photodetector is proportional to the incident optical power  $P_{opt,in}$  as can be seen in Eq. 3.10. In this equation  $\mathcal{R}$  denotes the responsivity and is 0.8 A/W for the given photodetector at 1550 nm.

$$I_{PD} = \mathcal{R} \times P_{opt,in} \quad (3.10)$$

The simple model suffices to design narrowband devices but it becomes inadequate in a broadband structure like the TWPD. Figure 3.6 shows that a simple RC network does not succeed in describing the electrical behavior of the photodetector over the entire frequency range. Closer inspection of the reflection coefficient (Fig. 3.6) shows the presence of an additional RC low-pass filtering with cut-off at 2.7 GHz. The extra resistance at higher frequencies is probably caused by leakage through the substrate which has a relatively low resistivity (about 10  $\Omega$ .cm). Consequently, the simple model should be expanded with an additional series RC tank describing the coupling to the lossy substrate. A last addition to the model is the metal pad capacitance  $C_m$ . These changes result in a model relying more on the physics in the VPIN Ge photodetector (Fig. 3.7), as described in [7].

To conclude the discussion on the small signal behavior, a fit was done for different reverse bias levels. A series inductance  $L_{lead}$  was added to the model in Fig. 3.7(b), to take into account the finite trace length between the bondpads and the standalone photodetector. The component values can be found in table 3.1, where only the junction capacitance  $C_j$  is voltage dependent and decreases with increasing reverse bias. In Fig. 3.8 it is

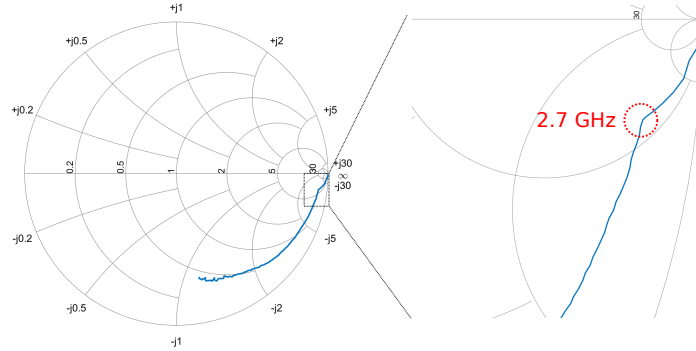


Figure 3.6: Measured output impedance of the Ge photodetector (2V reverse bias, 10 MHz to 50 GHz).

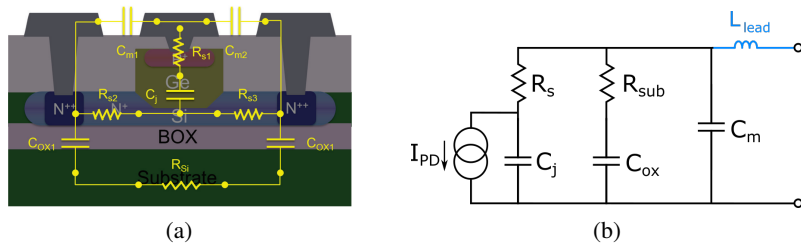


Figure 3.7: (a) Physical interpretation VPIN Ge PD (b) Equivalent circuit model of the VPIN Ge PD with lead inductance [7].

shown that the fitting quality is very good when the improved model is used to describe the small signal behavior of the photodetector.

### 3.3.2 Linearity

The responsivity  $\mathcal{R}$  defined in eq. 3.10 remains independent of the incident optical power as long as the photodetector is in its linear region. This is a necessary condition to enable the shift of the amplification from the electrical to the optical domain without distorting the transmitted data. Further in this chapter, different techniques will be looked at to improve the linearity of the overall O/E conversion. Two boundary conditions in this research are the requirement of having a high speed device and the desire to work with Complementary Metal-Oxide-Semiconductor (CMOS) compatible materials and processes. The former condition can be relaxed to having enough gain in the targeted RF band as will become clear in section 3.5.

	0 V	0.5 V	1 V	1.5 V	2 V	2.5 V	3 V
$C_j$ [fF]	53	46.5	42.5	40	38	37	36
$R_s$ [Ohm]				30			
$R_{sub}$ [Ohm]				1350			
$C_{ox}$ [fF]				80			
$C_m$ [fF]				10			
$L_{lead}$ [pH]				40			

Table 3.1: GPDCTE\_SVP INCF CWT\_2K\_15K2\_600: Equivalent model values in function of the reverse bias.

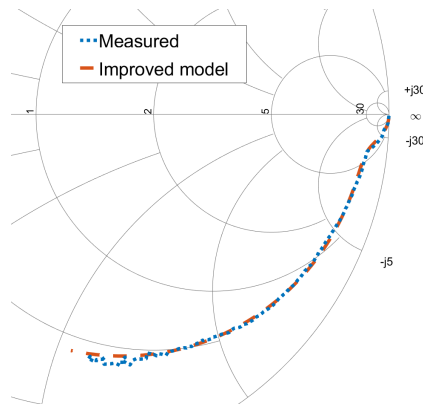


Figure 3.8: Quality of fitting on the standalone Ge VPIN PD using the improved model (2V reverse bias, 10 MHz to 50 GHz).

Photodetectors can on the one hand be classified based on the materials used: III-V compounds like InP versus group IV materials like Ge. On the other hand, this classification can be done based on the architecture of the stack: PIN, Uni-Traveling-Carrier (UTC), etc. PIN photodetectors use a simple layer stack of p-type and n-type material with an intrinsic layer in between. Consequently, both the electrons and holes will contribute to the photogenerated current. In a UTC PD, the material stack is designed in such a way that the holes are blocked which makes sure that only the electrons act as active carriers [9]. Electrons typically have a higher mobility than holes and the UTC PDs are therefore in general significantly faster than PIN-PDs. Not only the increase in speed is an advantage of the UTC structures but also the power handling is superior for UTC PDs. The two main causes of saturation effects in PDs are thermal failure and velocity modulation by space charge effects. The velocity mismatch between carri-

ers results in a charge imbalance within the depletion region [10, 11]. The build-up of this space charge region opposes the external bias. When the photocurrent increases, energy bands will bend and the drift velocity of the photogenerated carriers will drop. This effect is less visible in UTC PDs, at lower frequencies and for larger external bias. Larger external bias voltages will however increase the risk of electrical breakdown and shorten the lifetime due to Joule heating [12].

UTC photodetectors are commonly implemented with III-V compounds where they benefit from superior bandwidth and power handling capabilities due to the large difference between electron and hole velocity in those materials [3]. The story is significantly different for group IV materials where the difference between hole and electron velocity is small and where bandgap engineering capabilities are limited. Ge-on-Si UTC photodiodes do exist but their advantages are limited while the fabrication process becomes more complex, which increases the cost. To target the need for CMOS compatible devices which are as low-cost, reliable and compact as possible the designs in this dissertation rely on Ge PIN photodetectors from the iSiPP PDK.

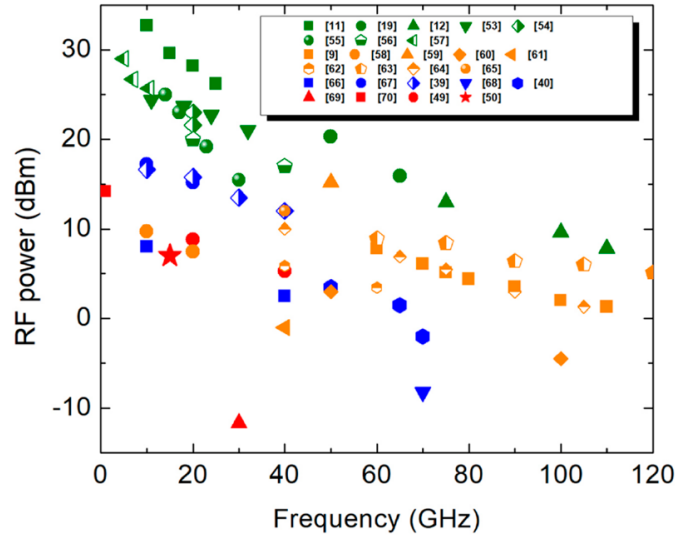


Figure 3.9: State of the art photodetector linearity [13] – Green: normal-incidence PDs on native InP substrate; Orange: waveguide PDs on native InP substrate; Blue: Integrated III-V-on-Si waveguide PDs; Red: integrated Ge-on-Si waveguide PDs.

An extensive state of the art study of the linearity for different photodetector topologies is performed by *Sun and Beling* in [13] and is shown in Fig. 3.9. A couple of conclusions can be drawn from this study. First of all, it is clear that the power handling decreases for increasing RF frequency. Secondly, the highest linearity detectors use normal incidence and are designed on native InP with special care for uniform illumination and good thermal dissipation. The other data points offer lower linearities since waveguide coupling of the photodetector is used. Non-uniform coupling to the active region causes localized space charge effects and thus lower power handling capabilities. A final conclusion that can be drawn from Fig. 3.9 is that III-V detectors typically offer higher saturation levels than Ge-on-Si photodetectors.

Nowadays, significant research interest is dedicated to improving the power handling capabilities of Ge-on-Si waveguide photodetectors as these are key building blocks for integrated microwave photonics circuits. While these Ge-on-Si waveguide detectors have a high bandwidth, the linearity might be too limited for microwave photonic systems. A straightforward way to boost the overall linearity of the detector is by using a detector-array rather than a single detector [14–16]. An alternative way to boost the power handling is achieved by redesigning the feeding structure to achieve a more uniform illumination of the absorption region [17–19].

To conclude, it should be noted that UTC photodetectors offer a larger saturation current - bandwidth product (SCBP) than Ge-on-Si photodetectors. However, Ge-on-Si photodetectors do benefit from CMOS-compatibility resulting in, amongst others, a lower cost and the potential to easily co-integrate with complex optical functionality on a single chip (e.g. integrated microwave photonics). In this chapter, solutions are therefore looked at to bring the linearity of Ge-on-Si based detectors closer to the values obtained with UTC photodetectors. Nevertheless, if maximal SCBP is of utmost importance, UTC photodetectors are still the way to go.

### 3.4 Traveling Wave Photodiode

*The work in this section has in part been published in [20] and [21]. Both are based on a first design of the TWPD, to conclude section 3.4 a second iteration TWPD will be briefly discussed.*

The linearity of a high-speed PD is typically inadequate to allow for high RF output power. To improve the power handling capabilities one can opt to

use different materials and detector principles (e.g. III-V UTC photodetectors integrated on silicon) or more complex photodetector configurations. While UTC photodetectors are often being used as high-power, high-speed photodetectors, they are not CMOS compatible because of their complex layer stack based on III-V materials (typically InGaAs-InP). To make optimal use of the benefits of silicon photonics, a high-power variant of the existing Si-integrated Ge PIN photodetector needs to be constructed without altering the technology stack of the iSiPP platform or requiring heterogeneous integration. A way to improve the power handling capability of the optoelectronic conversion is to increase the number of photodetectors per RAU. The power handled per individual PD drops proportional with the amount of PDs, enhancing the power limit of the RAU significantly. However, in the electrical domain the RF signals will need to be recombined constructively.

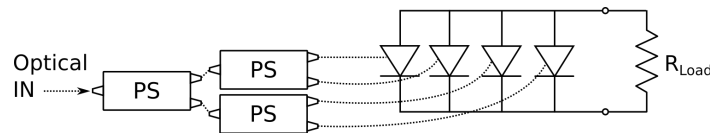


Figure 3.10: Lumped parallel photodetector configuration – PS: Power Splitter;  $R_{Load}$ : Load Resistor [21].

Combining multiple PDs in a lumped parallel fashion, as shown in Fig. 3.10, results in improved power handling but gravely deteriorates the bandwidth of the PD because of the increased capacitance forming a low pass RF filter. Adopting a traveling wave configuration to recombine the electrical signals originating from the individual PDs allows for high-speed, high-linearity opto-electronic conversion [22]. The underlying idea is that the PD parasitics are embedded in a transmission line design and therefore do not result in RC filtering.

### 3.4.1 Proposed Architecture

#### 3.4.1.1 Photodetector

In this dissertation, the iSiPP silicon photonics platform of imec is used to realize the traveling wave photodetector structure. The germanium photodiodes available on the platform have a responsivity of 0.8 A/W and a bandwidth of more than 50 GHz. However, their power handling capabilities are limited. While the standard mode of operation for the Ge photodiode on the iSiPP platform is to use a single optical input waveguide, one

of the features available in the platform is that the Ge PDs can be optically fed from two sides. This immediately allows for a linearity improvement by increasing the optical input power for which compression occurs in the opto-electronic conversion. By adding a splitter in front of the PD, the linearity can be improved at the cost of a slight increase in insertion loss (due to the excess loss of the splitter, which is specified to be below 0.2 dB). This enhanced power handling capability is caused by the increased portion of the absorption layer that is used for the opto-electronic conversion [14].

### 3.4.1.2 Star Coupler

The star coupler which was added to the final design has been presented in [23]. It adds an integrated 16-way power splitter to a fiber grating coupler from the iSiPP technology platform (Fig. 3.11). Consequently, the incoming light is split immediately over 16 channels and two-photon absorption resulting in non-linear losses is limited because the optical power present in the on-chip waveguides is significantly lowered. For the implemented TWPD, the balanced variant of the star coupler is being used as this provides a power imbalance of only 1.11 dB between the different channels. In [23], up to 275 mW - or equivalently 24.4 dBm - of optical input power was injected in the star coupler without significant non-linear losses.

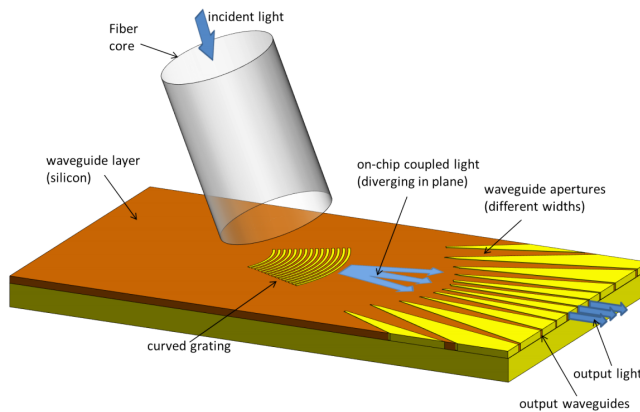


Figure 3.11: Star coupler [23].

### 3.4.1.3 Schematic Overview

In Fig. 3.12, the proposed high-power handling photodetector architecture is depicted together with a 16-PD implementation on the iSiPP silicon pho-

tonics platform. The design consists of three major parts. Firstly, a TWPD is used to allow for high-linearity, high-speed opto-electronic conversion. As discussed before, each PD will be dual fed to enhance the linearity of each Ge PD individually. Secondly, the goal is to recombine the RF signal from the individual Ge PDs constructively in the load. This will be accomplished by matching the optical and electrical delay using optical delay lines. Electrical signals originating from PDs closer to the load experience a smaller delay because of a shorter propagation distance along the transmission line. Hence, this should be compensated for in the optical domain to make sure that the different portions of the signal arising from the different PDs arrive simultaneously at the load. Lastly, incident power needs to be distributed among the PDs. Typical implementations use power splitting trees based on multiple 3 dB splitters [14]. In this dissertation, a monolithically integrated star coupler is used instead. This allows for improving the power handling capabilities of the passive waveguide circuit, which is limited by two-photon absorption [23]. The presence of a star coupler instead of a power splitting tree will become even more important when the number of photodiodes in a traveling wave photodiode is increased to further improve the linearity of the optoelectronic conversion and eventually enable a passive Downlink Remote Antenna Unit (DL-RAU). In the design shown in Fig. 3.12, the transmission line is terminated by a dummy load. This dummy load should ideally be equal to the impedance of the loaded transmission line and will absorb the backward propagating waves in the TWPD. Without the presence of such a dummy load, backward propagating waves will reflect at the position of the dummy load. Consequently, the backward propagating waves will couple with the forward propagating waves in the absence of such a dummy load. Those interference effects will be cancelled by the dummy load resulting in a higher bandwidth at the cost of an inherent 6 dB loss.

### 3.4.2 Design Procedure

The TWPD aims to maximize the amount of power provided to the load impedance  $R_{Load}$  while maintaining the high-speed capabilities of the original standalone photodetector. To get an optimal power transfer from the TWPD to the load, three criteria need to be fulfilled [14]. Firstly, delays in the optical and electrical domain should be matched. This is done by adding optical delay lines. Secondly, the characteristic impedance of the loaded transmission line should be sized in such a way that no reflections occur at the interface between the TWPD and the load. A final important part of the TWPD design is the presence of a termination resistor  $R_{Term}$  at

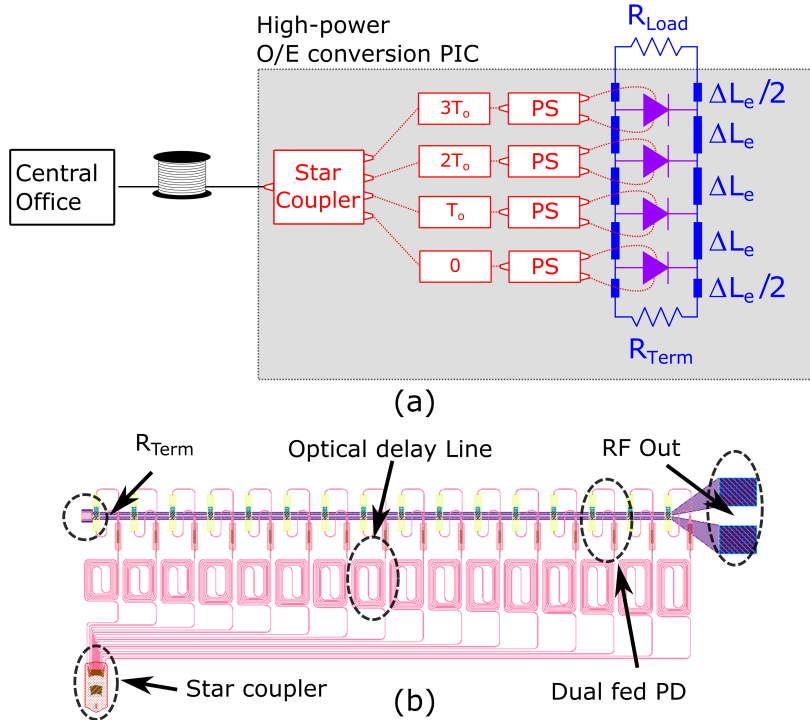


Figure 3.12: Germanium traveling wave photodetector structure: (a) schematic; (b) layout of the fabricated device – PS: Power Splitter;  $T_o$ : Optical Delay;  $\Delta L_e$ : transmission line segment length [21].

the opposite side of the TWPD. This termination absorbs backwards propagating waves. If  $R_{Term}$  is omitted, backwards propagating waves will couple to the forward direction resulting in interference and an associated bandwidth reduction.

A first step in the design of the TWPD consists of constructing a suitable distributed model for the transmission line periodically loaded with discrete photodetectors. The adopted model is shown in Fig. 3.13.  $L_{TL}$ ,  $C_{TL}$ ,  $R_{TL}$  and  $G_{TL}$  are the per unit length parameters of the unloaded transmission line while  $C_j$ ,  $R_s$ ,  $R_{sub}$ ,  $C_{ox}$  and  $C_m$  are part of the photodetector model (Fig. 3.7, table 3.1). At the time of designing the TWPD, the available model for the PD was the simple variant shown in Fig. 3.5 where the junction capacitance  $C_j$  and series resistance  $R_s$  were determined to have nominal values of respectively 35 fF and 35  $\Omega$  at 2V reverse bias.

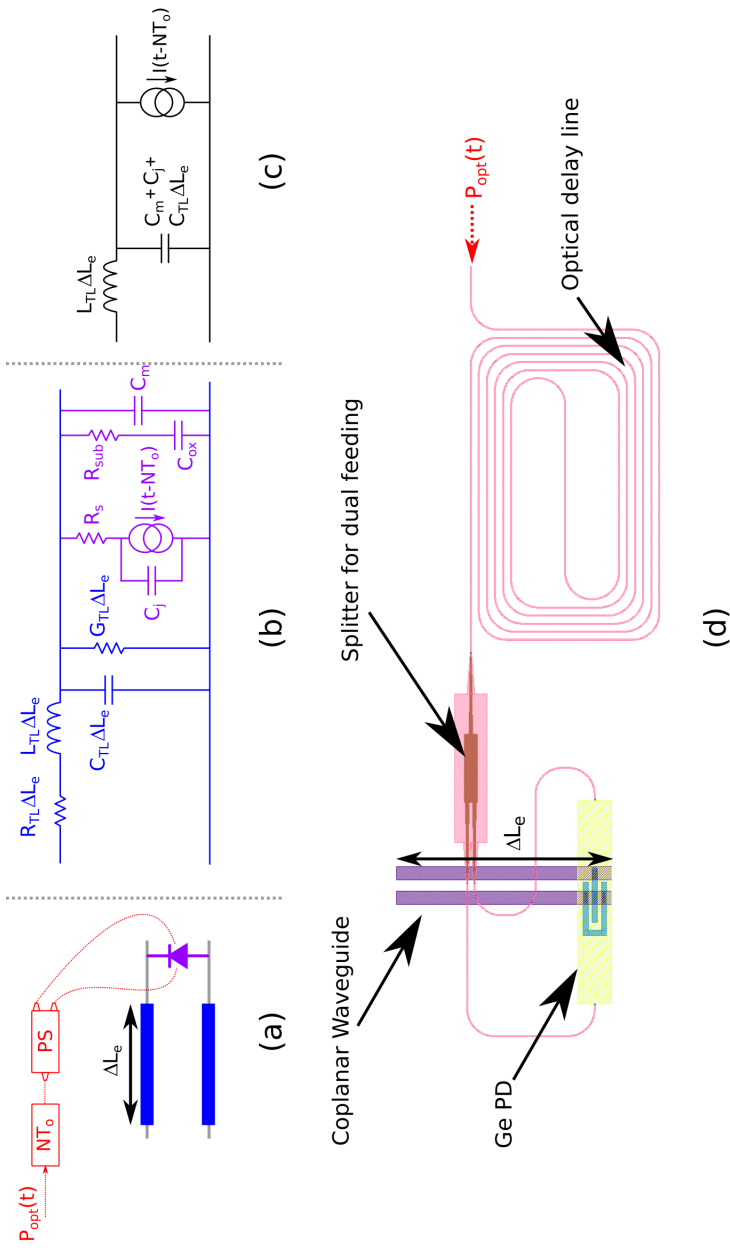


Figure 3.13: TWPDP model for a single photodetector-loaded transmission line segment (a) one segment; (b) its equivalent model; (c) a lossless equivalent model; (d) the layout of one fabricated segment [21].

Some initial values for sizing the transmission line can be easily derived when losses are ignored. Based on Fig. 3.13(c) it is possible to derive design guidelines [22] for impedance matching and delay matching and those guidelines are respectively given in Eqs. 3.11 and 3.12.

$$R_{Term} = R_{Load} = \sqrt{\frac{L_{TL} \times \Delta L_e}{C_{TL} \times \Delta L_e + C_j + C_m}} \quad (3.11)$$

$$T_o = \frac{\Delta L_e}{v_e} = \frac{\Delta L_o}{v_{o,g}} \quad (3.12)$$

The delay matching criterion takes into account the spacing between consecutive PDs ( $\Delta L_e$ ), the velocity of the RF signal  $v_e$ , the optical delay length  $\Delta L_o$ , and the group velocity of the optical signal  $v_{o,g}$ . The velocity of the electrical and optical signal can be found from Eqs. 3.13 and 3.14. In equation 3.14,  $c$  denotes the speed of light and  $n_g$  is the group index which is 4.26 at 1550 nm for the 450 nm wide waveguides used in the delay lines.

$$\frac{1}{v_e} = \sqrt{L_{TL} \times \left( C_{TL} + \frac{C_j + C_m}{\Delta L_e} \right)} \quad (3.13)$$

$$v_{o,g} = \frac{c}{n_g} = \frac{c}{4.26} \quad (3.14)$$

The TWPD was designed on the iSiPP platform starting from Eq. 3.11, with a target load impedance of 50  $\Omega$ . As discussed before, the adopted photodetector model consists of  $C_j = 35$  fF,  $R_s = 35$   $\Omega$  and  $C_m = 0$  fF. Taking into account these parameters and the requirements on minimal trace width (imposed by design rules and the heating of the traces) and minimal trace spacing (imposed by design rules), a coplanar waveguide was designed. The final design is shown in Fig. 3.13(d), and consists of a signal-ground topology with trace widths of 5  $\mu\text{m}$  and a gap of 4.2  $\mu\text{m}$ . This coplanar waveguide was periodically loaded with Ge photodetectors. Finally, delay matching is ensured by the addition of optical delay lines based on Eq. 3.12.

The designed TWPD segment is depicted in Fig. 3.13(d) and the entire TWPD is shown in Fig. 3.12(b). The total size of the 16-PD traveling wave photodiode is 1415  $\mu\text{m}$  by 469  $\mu\text{m}$ . Measurements on the fabricated device show a 35.4  $\Omega$  characteristic impedance for the loaded TWPD. This number was verified by re-simulating the device with the fabricated dimensions. The deviation relative to the targeted 50  $\Omega$  can be attributed to the fact that  $\Delta L_e$  was chosen too small (80  $\mu\text{m}$  instead of the desired 190  $\mu\text{m}$ ).

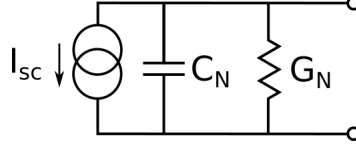


Figure 3.14: Norton equivalent of the photodetector.

Until now, losses were ignored in the photodetector and transmission line. Adding losses has two important consequences: there will be an inherent low-pass filtering of the photocurrent and the RF signal will experience attenuation during the transmission from photodetector to load. To describe the influence of the losses, the simple photodetector model (Fig. 3.5) should be converted to its Norton equivalent (Fig. 3.14). The short circuit current  $I_{sc}$  of the photodetector (Eq. 3.15) shows an inherent low pass filtering with a 3 dB bandwidth of 129 GHz for the adopted PD. The values of the capacitance  $C_N$  and conductance  $G_N$  of the Norton equivalent are respectively provided in equations 3.16 and 3.17. When staying well below the 3 dB frequency, the denominator stays close to 1.

$$I_{sc} = \frac{I_{PD}}{1 + j\omega R_s C_j} \quad (3.15)$$

$$C_N = \frac{C_j}{1 + \omega^2 C_j^2 R_s^2} \approx C_j \quad (3.16)$$

$$G_N = \frac{\omega^2 C_j^2 R_s}{1 + \omega^2 C_j^2 R_s^2} \approx \omega^2 C_j^2 R_s \quad (3.17)$$

To find the losses of the transmission line [24], equation 3.18 is used where  $\alpha$  combines the losses caused by the finite conductivity of the metal traces (first term) and the finite substrate leakage (second term, mainly due to  $G_N$ ). Evaluation of equation 3.18 for the designed TWPD at 30 GHz shows around 1.2 dB/mm loss caused by the finite trace conductivity and 2.8 dB/mm loss due to the finite series resistance of the photodetector. The large transmission line losses at high frequencies will also be visible in the transfer function of the TWPD where the contribution of the photodetectors located far away from the load will be small.

$$\alpha = \frac{R}{2Z_0} + \frac{GZ_0}{2} \approx \frac{R}{2Z_0} + \frac{\omega^2 C_j^2 R_s Z_0}{2} \quad (3.18)$$

### 3.4.3 Frequency Dependent Behavior

Five structures are compared in this dissertation, all of which rely on the same waveguide integrated Ge-on-Si photodetector. The first two structures are standalone photodetectors: one of them feeds the active region from one side while the other uses a dual feed approach. While dual-fed detectors offer increased power handling, it will not affect the small signal characteristics of the device. Furthermore, a parallel combination with 16 photodetectors was fabricated as shown in Fig. 3.15. Finally, two traveling wave photodetectors were devised based on Fig. 3.12. The two TWPD variants differ in the value of  $R_{Term}$  where one of them uses a matched termination ( $R_{Term} = 50 \Omega$ ) while the other omits the termination.

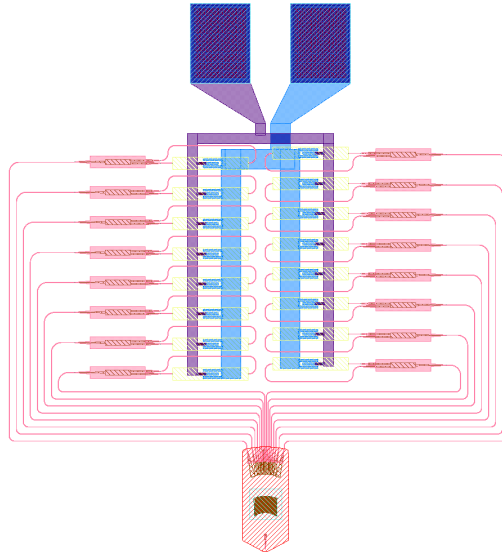


Figure 3.15: Parallel 16-photodetector reference design.

#### 3.4.3.1 Output Impedance

The output impedance was measured with the *N5247A PNA-X* after calibration with a *CS-8 SOL calibration kit*. The impedance of the standalone photodetector has been discussed in section 3.3. It was shown that the junction capacitance decreases with increasing reverse bias resulting in an increased bandwidth at stronger reverse biasing. Additionally, it was mentioned that substrate leakage should not be neglected.

Adding multiple of those photodetectors in parallel will make the device even more capacitive, which can be easily understood when looking at the Norton equivalent of the simple PD model (Fig. 3.14). The output impedance for the device in Fig. 3.15 is shown in Fig. 3.16 for a 2V reverse bias. This parallel combination of 16 photodiodes shows strong capacitive behavior and becomes inductive starting from 20 GHz due to the parasitic inductance in the interconnections.

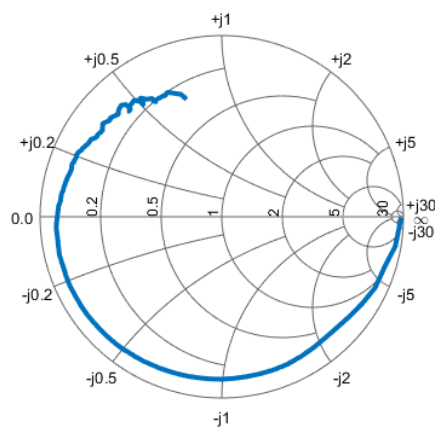


Figure 3.16: Output impedance of the parallel combination of 16 PDs (2V reverse bias, 10 MHz to 50 GHz).

To overcome this speed-linearity trade-off, TWPDs were designed. In a traveling wave architecture the junction capacitance is absorbed in the transmission line design. As previously mentioned, the realized characteristic impedance is  $35.4 \Omega$  and thus the S-parameters depicted in Fig. 3.17 and Fig. 3.18 are given for a reference impedance of  $35.4 \Omega$ . It is clear that the dummy terminated TWPD results in a matched transmission line (Fig. 3.17) while the variant without dummy termination acts as a lossy open transmission line (Fig. 3.18). Furthermore, figure 3.17 shows that the DC output impedance of the dummy terminated transmission line increases with increasing reverse bias. This is caused by self-heating of the dummy termination. While the nominal resistance of this PDK component is  $50 \Omega$ , any applied bias will increase the effective resistance value as can be seen in Fig. 3.19. Finally, because of the lossy nature of the transmission line at higher frequencies, the two structures tend to resemble each other at higher frequencies. This will also be visible when comparing the  $S_{21}$  transfer characteristics of both TWPD variants.

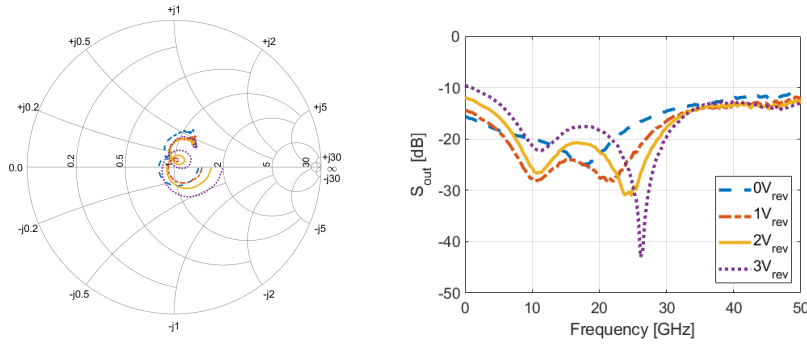


Figure 3.17: Output impedance of the 16-PD TWPD with dummy termination (2V reverse bias, 10 MHz to 50 GHz,  $35.4 \Omega$  reference).

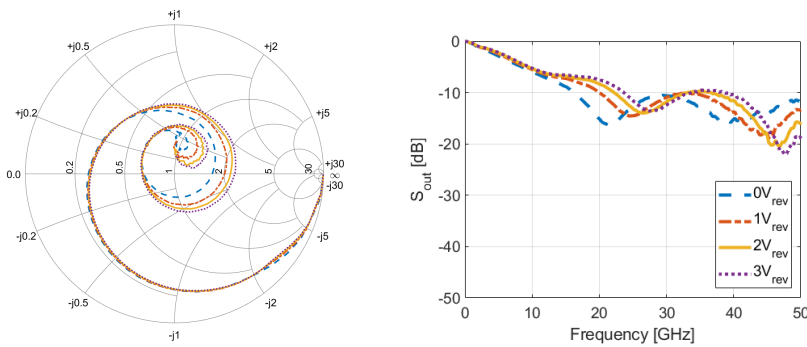


Figure 3.18: Output impedance of the 16-PD TWPD with open termination (2V reverse bias, 10 MHz to 50 GHz,  $35.4 \Omega$  reference).

### 3.4.3.2 Transfer Characteristics

The output power for the different detectors is shown in Fig. 3.20 under the assumption that each photodetector generates exactly 2 mA peak-to-peak current. This is done to get an idea about the combined effect of power saturation and bandwidth limitations. These simulations are performed with the fabricated dimensions, i.e. the TWPDs have a characteristic impedance of  $35.4 \Omega$ . It is clear that the bandwidth of the photodetector drops heavily when multiple are placed in parallel. Adopting a traveling wave configuration can help to increase the bandwidth when a matched dummy termination is present. However, the dummy termination sinks half the current, resulting in an intrinsic 6 dB power drop.

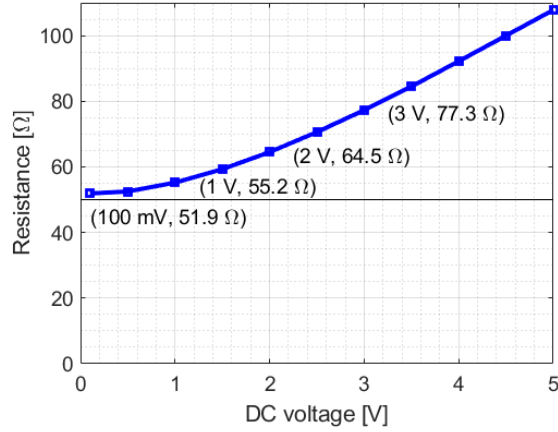


Figure 3.19: Effective resistance value of the  $50 \Omega$  termination resistance as a function of the applied DC voltage.

When the dummy termination is omitted, interference effects are clearly visible. For the fabricated device, the dummy termination differs from the characteristic impedance of the loaded transmission line and therefore we can even see these interference effects in the dummy terminated TWPd. Furthermore, Fig. 3.20 indicates that at higher frequencies there is little to no difference between the TWPd with and without termination resistor. This can be attributed to the lossy nature of the transmission line attenuating back-traveling reflections that interfere with the forward traveling wave operation, consequently resulting in damped interference effects at higher frequencies. It appears that the transmission line losses are mainly caused by the high series resistance  $R_s$  of the photodetector (eq. 3.18), which is  $35 \Omega$  for the adopted photodetector and should be as close to zero as possible for an ideal TWPd. When this series resistor is omitted in simulations, interference peaks and dips are clearly visible even at higher frequencies.

When a multi-PD structure is used, the low frequency current sunk into the load is expected to scale with the number of PDs and therefore the available power at the load is following a quadratic scaling with the PD count if the current per photodetector remains the same. Since the implemented multi-PD structures consist of 16 photodetectors, the low frequency output power should increase with 24 dB when the current per photodetector is kept constant. Additionally, since a termination resistor absorbs the backwards propagating waves in a transmission line, a 6 dB drop at low frequencies is expected when adding a termination to the TWPd. In practice,

however, additional substrate losses will reduce the power gain. These substrate losses are modeled by  $R_{sub}$  in Fig. 3.13 and are found to be close to  $1350 \Omega$  for the given photodetector. For the unterminated TWPD, they reduce the ideal power gain by 4.1 dB, resulting in 19.9 dB gain compared to the standalone PD. The terminated TWPD suffers 2.1 dB power loss due to the presence of substrate losses. This results in a 15.9 dB power gain compared to the standalone PD rather than the 18 dB gain that would be achieved in the absence of any substrate losses.

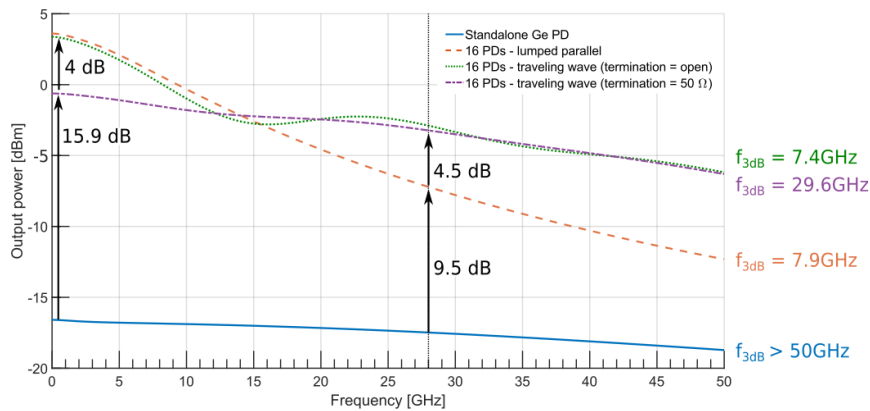


Figure 3.20: Simulated output power in a  $50 \Omega$  load for the different photodiode structures when each PD individually generates 2 mA peak-to-peak current (2V reverse voltage) [21].

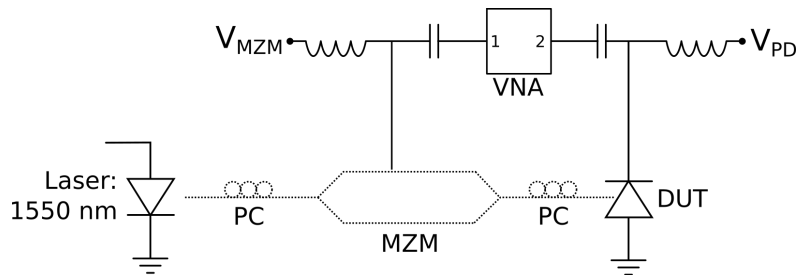


Figure 3.21: Setup used for bandwidth measurements – PC: Polarization Controller; MZM: Mach Zehnder Modulator; DUT: Device Under Test; VNA: Vector Network Analyzer [21].

The frequency dependence of the receiver structures was measured as part of a back-to-back ARoF link (Fig. 3.21) at a wavelength of 1550 nm where the Mach Zehnder Modulator (MZM) was biased at its quadrature point. To compensate for the frequency dependent effects in the MZM, a high-bandwidth reference PD was used for calibration. Subsequent measurements with the actual Device Under Tests (DUTs) were then normalized with respect to the  $S_{21}$  obtained with the high-speed detector.

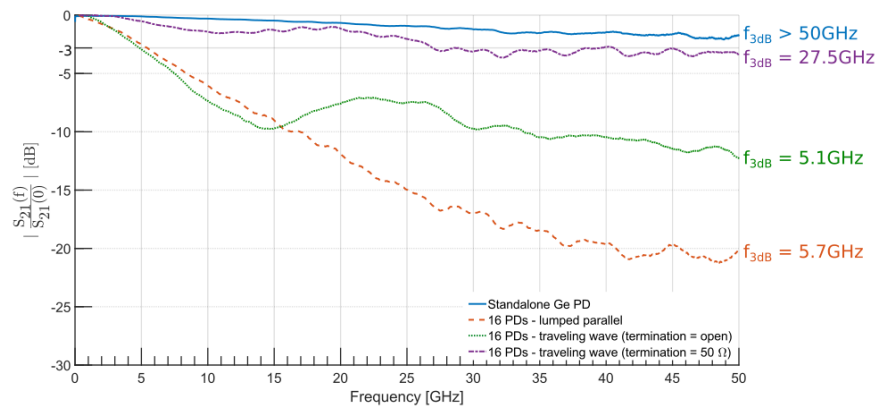


Figure 3.22: Normalized measured  $S_{21}$  after calibration of the MZM response [21].

Measured  $S_{21}$  curves for the different devices are given in Fig. 3.22 under a 2 V reverse bias. Unlike Fig. 3.20, the curves are normalized relative to their low frequency value to disregard the differences in coupling losses to the DUT, which depends heavily on the exact alignment. Figure 3.22 shows the high-bandwidth potential of the TWPD structure with dummy termination, while interference notches and peaks are present for the TWPD where the termination resistor is omitted. The obtained results (Fig. 3.22) resemble the simulated data (Fig. 3.20) well, but the bandwidth is slightly less for the measured devices compared to the values obtained in simulations. This can in part be attributed to an underestimation of the junction capacitance  $C_j$  of the photodetector.

### 3.4.4 Linearity

#### 3.4.4.1 DC Linearity

The first linearity measurement that was performed concerns the conversion from Continuous Wave (CW) optical power (at 1550 nm) to DC electrical

current by the DUT. The setup used for this measurement is described in Fig. 3.23 and the obtained results are provided in table 3.2. Figure 3.24 shows the influence of the reverse voltage on the linearity of the standalone dual fed PD. The measurements in table 3.2 are all performed at a 2V reverse bias. Important to notice when observing the results is that dual feeding provides a higher linearity compare to single feeding and that multi-PD solutions offer a substantial increase in power handling capabilities.

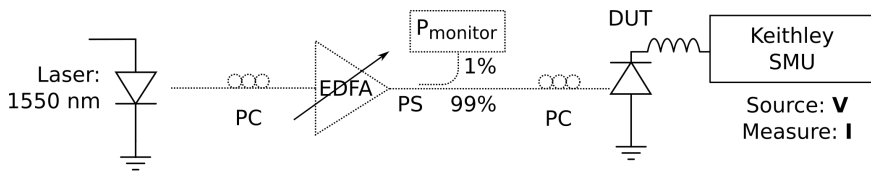


Figure 3.23: Setup used for DC linearity measurements – EDFA: Erbium Doped Fiber Amplifier; SMU: source measure unit [21].

# of PDs	Configuration	Extra features	DC Linearity
1	N/A	Single fed	8 mA
1	N/A	Dual fed	13.9 mA
16	Lumped parallel	Dual fed	> 137.4 mA
16	TWPD	$R_{term} = \text{open}$ , Dual fed	> 103 mA
16	TWPD	$R_{term} = 50 \Omega$ , Dual fed	> 91.8 mA

Table 3.2: Linearity: DC 1dB compression point [21].

Lower boundaries are provided for the multi-PD solutions since these structures are still linear at maximum available power. Up to 28 dBm of optical power can be delivered to the Photonic Integrated Circuit (PIC) by the booster EDFA that was used during the measurements. The available power at the photodetectors is reduced even further due to coupling losses from the fiber probe to the output of the on-chip grating coupler [23], which is typically 3 to 7 dB depending on the exact coupling conditions. Hence, the maximum total power coupled to the PD-array is between 125 mW and 316 mW which will give rise to a photocurrent between 100 mA and 253 mA ( $\mathcal{R} \approx 0.8 \text{ A/W}$ ). This maximum available power range does not yet take into account any excess losses: the optical losses caused by the MMIs needed for the dual fed operation (less than 0.2 dB per MMI), the waveguide losses in the optical delay lines (approximately 0.26 to 0.41 dB for the different delay lengths) and the resistive losses in the transmission line.

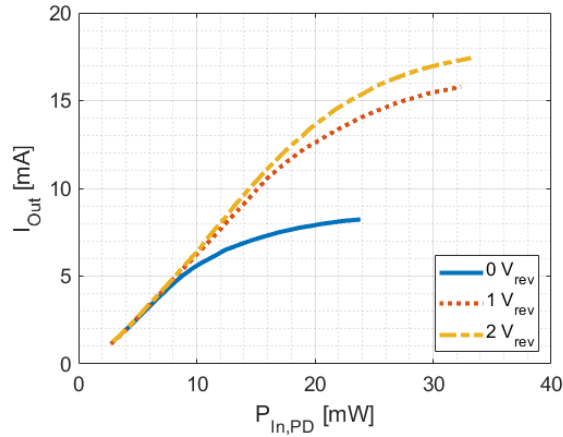


Figure 3.24: Linearity of the dual fed standalone photodetector in function of the reverse voltage.

For the TWPD with termination resistor, the output current consists of two contributions, as discussed in Fig. 3.25. In the absence of light at the input of the device, the structure produces an output current which is proportional to the applied reverse bias voltage (dark current). Secondly, a current proportional to the optical input power is generated in the photodetector (with proportionality factor  $\mathcal{R}$ , the responsivity). The former contribution is subtracted from the measured current to examine the linearity of the opto-electronic conversion. The value provided in table 3.2 only considers this opto-electronic contribution. For the 16-PD arrays we expect approximately a 16-fold increase in maximum linear output current, namely 222.4 mA. Unlike for the RF behavior, no coupling to the substrate occurs because of blockage by the buried oxide and hence no drop compared to this 16-fold increase is introduced by the  $R_{sub}$ . Contrary to the RF measurements, the current was quantified with a low-ohmic load (a Keithley source meter) and therefore the termination impedance does not sink half the current. In the RF measurements, the Electrical Spectrum Analyzer (ESA) is a  $50 \Omega$  load and hence, for those measurements, the presence of the termination impedance does not only alter the bandwidth but also the output power.

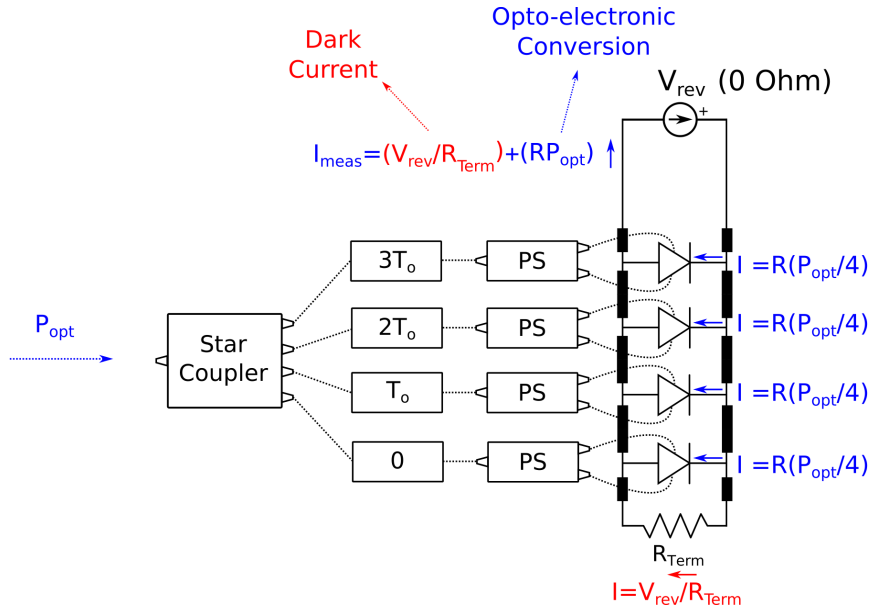


Figure 3.25: Current contributions in a terminated TWPD –  $P_{opt}$ : Optical input power;  $\mathcal{R}$ : responsivity [21].

#### 3.4.4.2 RF Linearity

In section 3.3 it was mentioned that the power handling capabilities are frequency dependent and decrease with increasing frequency. For fifth generation wireless networks, the 28 GHz band is particularly interesting. Hence, the RF power limit at 28 GHz will now be discussed. To assess in detail the linearity of the multi-PD structures, Third Order Intercept point (TOI) measurements were performed since these measurements are not limited by the maximum available power on-chip. In order to make sure that the measured non-linearities are caused by the DUT, the two-wavelength measurement setup discussed in [25] was implemented.

The adopted setup can be seen in Fig. 3.26. This setup consists of two transmitters working at different wavelengths. It is important that both operate at wavelengths spaced far enough from each to make sure that beat notes between the two cannot be received by the PD. On the other hand, the wavelengths should be close enough to the center wavelength such that the optical components (e.g. star coupler) still work as expected. In our setup, CW lasers at 1548 and 1552 nm are used. Both lasers are externally modulated with a sine wave: the 1548 and 1552 nm lasers are respectively modulated with a 27.999 GHz and 28.001 GHz sine by a  $LiNbO_3$  MZM

biased at its quadrature point and driven at 34% modulation depth. The modulated signals coming from both transmitters are subsequently combined, amplified with an EDFA and finally sent to the DUT.

In the DUT, the two tones are generated and these give rise to intermodulation products that are caused by the receiver rather than the whole link. Only the ESA and DUT produce third order intermodulation products at 27.997 and 28.003 GHz in this scenario. Non-linearities induced by the ESA can be neglected when the internal attenuation in the ESA is set sufficiently high.

The optical components might generate beat products but the two optical frequencies are separated by approximately 500 GHz (i.e. a spacing of 4 nm at 1550 nm) and therefore those optical non-linearities will not distort the obtained results. The modulator can generate a signal at twice the fundamental frequency and this can cause overlapping beat products by mixing with the fundamental tone of the other transmitter. However, since the MZM is biased at its quadrature point, only odd order harmonics will be introduced and the output spectrum of the MZM will be reasonably free of even order harmonics. This will help to minimize intermodulation products caused by the second harmonic generated in one MZM and the fundamental tone generated in the other MZM. Consequently, the third-order intermodulation product of the DUT will be more accurately determined [25] than with a single transmitter setup.

The results of the TOI measurements (at 28 GHz) are provided in table 3.3. One can see a 7 dB increase in power handling capabilities when dual feeding the PD. Additionally, it is clear that multi-PD structures are capable of handling higher powers. Adding multiple photodetectors in parallel results in RC low pass filtering as discussed before. Taking into account the frequency dependent current-to-power conversion, displayed in Fig. 3.20, of the parallel combination of 16 PDs, an improvement of approximately 9.5 dB over the dual fed, standalone germanium photodetector is expected. This value agrees reasonably well with the measured linearity improvement, namely 10.6 dB. For the TWPD with and without dummy termination improvements of respectively 14.2 dB and 14.6 dB are to be expected over the standalone, dual fed Ge PD. The measured improvements in linearity are respectively 15.8 dB and 13.2 dB.

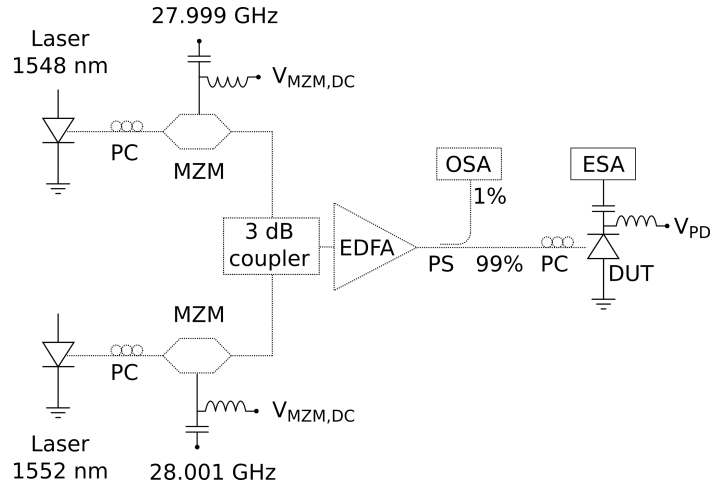


Figure 3.26: Setup used for TOI linearity measurements – OSA: Optical Spectrum Analyzer; ESA: Electrical Spectrum Analyzer [21].

# of PDs	Configuration	Extra features	TOI at 28 GHz
1	N/A	Single fed	-1.79 dBm
1	N/A	Dual fed	5.22 dBm
16	Lumped parallel	Dual fed	15.83 dBm
16	TWPD	$R_{term} = \text{open}$ , Dual fed	18.43 dBm
16	TWPD	$R_{term} = 50 \Omega$ , Dual fed	20.98 dBm

Table 3.3: Output referred third order intercept point at 28 GHz [21].

### 3.4.5 Second Iteration TWPD

*The main focus in this second generation device was on solving the impedance issues, i.e. error in characteristic impedance of the transmission line and self-heating in the termination. Linearity measurements are therefore not included in this section. Furthermore, a decrease in linearity is to be expected due to the lower PD count as well the replacement of the star coupler by a regular power splitting tree.*

To conclude section 3.4, a second iteration of the design will be discussed. Figure 3.27 shows a high power beamforming cell serving 2 antenna elements and it includes a 3 dB splitter at the input, a 4 bit True Time Delay (TTD) cell explained in more detail in chapter 4, and a 8-PD TWPD. The layout of the second generation traveling wave photodetector is shown

in more detail in figure 3.28. Four main differences compared to the first version should be noted. Firstly, the transmission line was redesigned to obtain a  $50 \Omega$  characteristic impedance and during this redesign traces of the transmission line were made wider to reduce conductor losses. Secondly, the termination was replaced by bondpads to enable the use of an off-chip resistor for reduced voltage dependencies of the resistance. Thirdly, the power distribution network uses a power splitting tree rather than a star coupler. Adding a tunable delay cell in front of the TWPD results in a long waveguide section before power distribution occurs which prevents the star coupler from offering low on-chip optical powers. Finally, the pitch of the power splitting tree outputs ( $\Delta L_{ps}$ ) was chosen in such a way that together with the PD pitch ( $\Delta L_e$ ) velocity matching between electrical and optical signals is achieved without the need for spiral optical delay lines.

The final dimensions of the second generation TWPD are:  $\Delta L_e = 221.5 \mu\text{m}$ ,  $\Delta L_{ps} = 30 \mu\text{m}$ , signal and ground trace width =  $15 \mu\text{m}$ , gap between ground and signal trace =  $4.15 \mu\text{m}$ . Standalone variants of the open TWPD and on-chip dummy terminated TWPD are available for characterization. The output impedance of the dummy terminated and open variants of the second generation TWPD are respectively shown in Fig. 3.29 and Fig. 3.30. It is clear that the dummy terminated TWPD shows broadband matching. To conclude this section, the  $S_{21}$  curves of both structures are given in figure 3.31. Similar remarks can be made as for the first generation TWPD: the dummy terminated TWPD shows a high bandwidth while the open TWPD suffers from interference effects. This graph shows normalized transfer functions so the inherent 6 dB loss induced by the termination should be taken into account when comparing output power levels for both detectors.

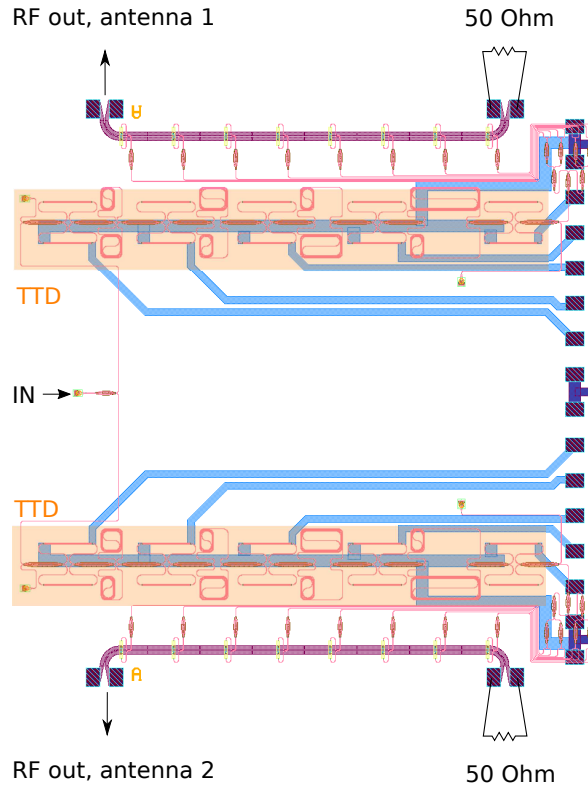


Figure 3.27: High power beamforming cell for 2 antenna elements.

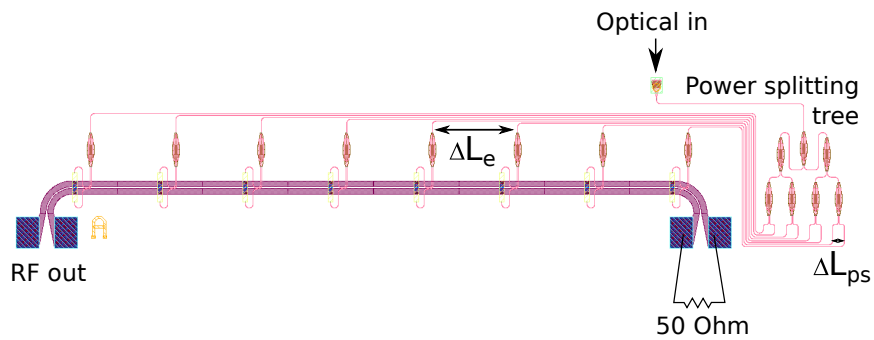


Figure 3.28: Second generation TWPD.

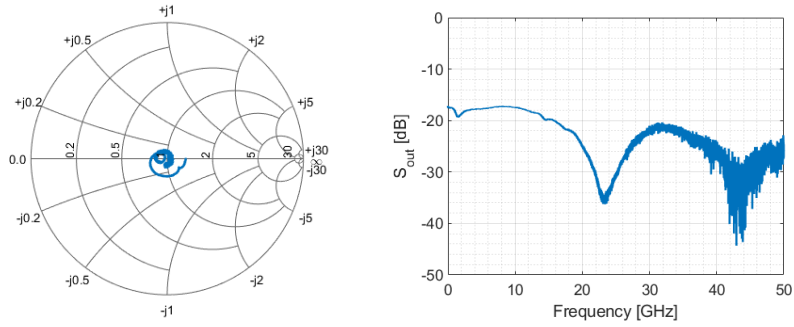


Figure 3.29: Output impedance of the 2nd generation 8-PD TWPD with dummy termination (2V reverse bias, 10 MHz to 50 GHz, 50 Ω reference).

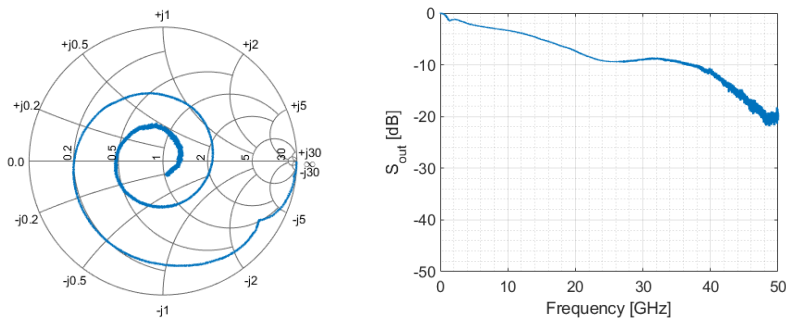


Figure 3.30: Output impedance of the 2nd generation 8-PD TWPD with open termination (2V reverse bias, 10 MHz to 50 GHz, 50 Ω reference).

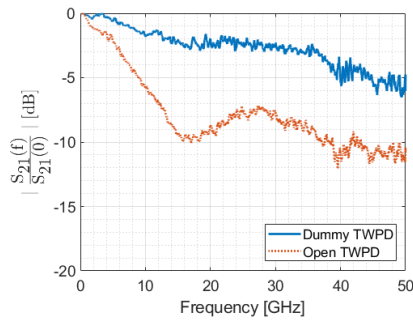


Figure 3.31: Measured  $S_{21}$  of the 2nd generation 8-PD TWPDs after calibrating out the MZM response (2V reverse bias).

### 3.5 Narrowband Matching of a Photodiode

*The work in this section has in part been published in [26].*

Taking the narrowband context of this dissertation into account, it is clear that the broadband property of the TWPD is not required since we only need to maximize power handling around the RF frequency. Maximization of the power transfer from the PD(-array) to the load translates in the requirement of having a conjugate match around the carrier frequency.

In this dissertation, a first order LC matching network is adopted to implement the narrowband impedance matching of the PD(-array). A low pass configuration is preferred as this allows for external biasing of the photodetector. For narrowband applications, the photodetector can be described by the simple equivalent model shown in Fig. 3.5. Hence, Fig. 3.32 can be used to describe the behavior of the matching network. The impedance seen at the output of the LC matched photodetector is given in equation 3.19 and the inductance  $L_M$  and capacitance  $C_M$  should be sized in such a way that the output impedance is conjugately matched to the load ( $50 \Omega$  in this section) at the carrier frequency (30 GHz in this section).

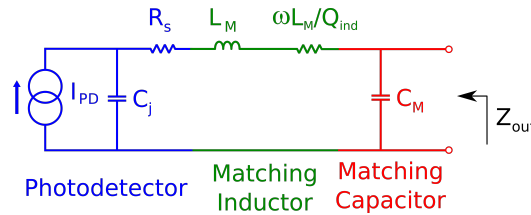


Figure 3.32: Equivalent network of the LC matched photodetector [26].

$$Z_{out} = \frac{1}{j\omega C_M} \parallel \left[ \left( j\omega L_M + \frac{\omega L_M}{Q_{ind}} \right) + R_s + \frac{1}{j\omega C_j} \right] \quad (3.19)$$

#### 3.5.1 A Comparison with the Broadband TWPD Approach

To compare broadband and narrowband solutions, the overall responsivity of different PD architectures will be discussed below. This comparison relies on the simple photodetector model from Fig. 3.5 with a  $35 \Omega$  series resistance and a 35 fF junction capacitance. Table 3.4 shows the current transfer from the total internally generated photocurrent  $I_{PD}$  to the output current sunk into a  $50 \Omega$  load at 30 GHz. For this discussion, the power distribution network is assumed to be lossless and is assumed to provide

uniform distribution to the different PDs. Since on-chip inductors typically show high losses, the performance characteristics of the LC matched circuits are not only given for ideal passives ( $Q = \infty$ ), but also for narrowband matching with lossy inductors (e.g.  $Q = 10$ ).

# of PDs	TWPD ( $R_{term} = \infty$ )	TWPD ( $R_{term} = 50 \Omega$ )	Lumped Parallel
1	0.90	0.48	0.87
2	0.76	0.46	0.75
4	0.48	0.45	0.54
8	0.45	0.43	0.33
16	0.38	0.37	0.18

# of PDs	LC Matched ( $Q = \infty$ )			LC Matched ( $Q = 10$ )		
	$R_{DUT}$	$L_M$ [pH]	$C_M$ [fF]	$R_{DUT}$	$L_M$ [pH]	$C_M$ [fF]
1	1.81	925.7	69.5	–	–	–
2	1.28	528.6	144.6	1.02	534.0	95.7
4	0.91	301.8	230.4	0.70	322.2	163.5
8	0.64	175.5	342.6	0.47	198.3	241.1
16	0.45	104.5	496.1	0.31	126.8	334.3

Table 3.4: Responsivity comparison for broadband and narrowband solutions:  $\frac{I_{out}}{I_{PD}}$  into a  $50 \Omega$  load at 30 GHz.

First of all, the lumped parallel variant clearly suffers from bandwidth degradation due to increased RC filtering for high PD count. Adopting a traveling wave configuration improves the bandwidth and here we have the aforementioned choice of whether to add a dummy termination or not. The dummy termination improves the bandwidth but sinks away half the current. For higher PD counts the transmission line becomes rather long and lossy and the distant PDs will have a minor contribution. This results in the fact that both types of traveling wave photodetectors will become comparable at higher frequencies when the PD count is high.

Introducing LC matched circuits into the comparison, it should first of all be mentioned that values larger than 1 can be observed in table 3.4 which is the result from peaking in the resonant matching network. Increasing the number of photodetectors respectively decreases and increases the values for  $L_M$  and  $C_M$ . When the inductors are assumed to be quite lossy (e.g. a Q-factor of 10), the overall responsivity drops and the required values for

the passives change. For the single PD device, inductors with a Q-factor of 10 will give rise to the fact that no solution can be found for eq. 3.19 to get perfect conjugate matching to  $50 \Omega$  with the matching network discussed in Fig. 3.32. Finally, it should be noted that ideal LC matching results in halving of the maximum available power every time the PD count doubles since the total equivalent Norton resistance is halved. This can be seen in table 3.4 by a decrease in output current with a factor  $\sqrt{2}$  every time the PD count doubles.

For narrowband applications, resonant matching gives a significant boost to the output power but this will depend on the availability of high Q-factor inductors. Added benefits of the narrowband design are the reduced surface area and the fact that velocity matching is in principle no longer needed (for a reasonable amount of PDs). For this dissertation, resonant designs with single photodetectors and 4-PD arrays were constructed (fig. 3.33).

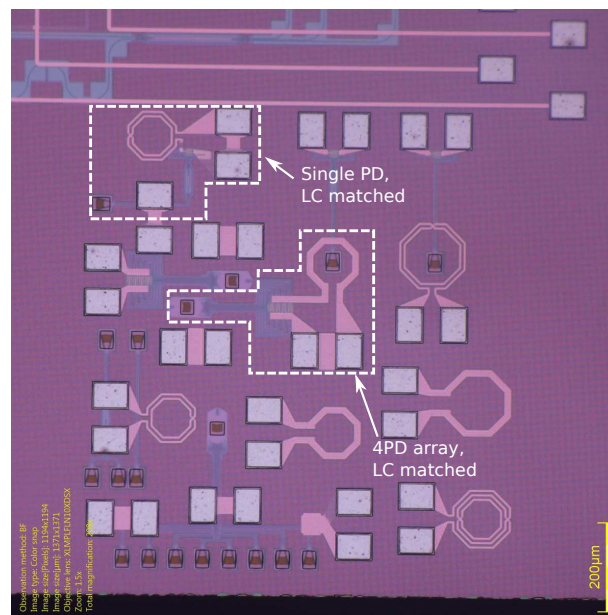


Figure 3.33: Structures for narrowband matching and testing of RF passives on iSiPP.

### 3.5.2 RF Passives on a Silicon Photonics Platform

Passive RF components are bulky and it is therefore advantageous to move them to the PIC where the cost per surface area is substantially lower [27].

In this section, the commercial iSiPP silicon photonics platform from imec (Fig. 3.3) is being used to demonstrate a monolithically integrated matching network. The stack of this technology platform includes two metal layers and therefore allows for the introduction of RF passives on the PIC. While resistors can easily be constructed on the iSiPP platform, only inductors and capacitors are looked at to allow for lossless matching.

### 3.5.2.1 Capacitors

The Back End of Line (BEOL) of the iSiPP silicon photonics platform includes two metal layers (Cu) separated by an oxide ( $SiO_2$ ). Consequently, parallel plate Metal-Insulator-Metal (MIM) capacitors are readily available in iSiPP. The capacitance value [28] can be approximated by using equation 3.20 where  $\epsilon_0$ ,  $\epsilon_r$  and  $t$  are fixed (respectively the permittivity of vacuum, the relative permittivity and the thickness of the oxide) and where the parallel plate overlap area  $A$  can be adjusted to size the capacitance. The second term in the approximation is a correction term to roughly include the fringe effects (with  $P$  the perimeter of the parallel plates). For the iSiPP technology platform, the formula approximation in equation 3.20 can be used. Measured values are approximately 10 to 15 percent lower than what is expected from this approximation. This can be attributed to an overestimation of the relative permittivity of the  $SiO_2$  or an underestimation of the oxide thickness. Secondly, the capacitors are to be used in high-speed systems. Consequently, the Self-Resonant Frequency (SRF) should be sufficiently high. This is done by placing the parallel plate capacitor in between the bondpads to minimize the lead length and therefore maximize the SRF.

$$C = \frac{\epsilon_0 \epsilon_r A}{t} + \epsilon_0 \epsilon_r P \quad (3.20)$$

$$\stackrel{\text{iSiPP}}{\approx} 69 \text{ aF} \times A [\mu\text{m}^2] + 34 \text{ aF} \times P [\mu\text{m}]$$

### 3.5.2.2 Inductors

A second important building block in lossless matching networks are spiral inductors [28]. The presence of a second metal layer allows for multi-turn spiral inductors largely extending the range of feasible inductances. The design parameters for such spiral inductors are the trace width, the spacing between turns, the radius of the inner turn and the number of turns. Minimizing the number of turns is desirable for high-speed applications to minimize the inter-winding capacitance and consequently maximize the SRF. Secondly, it is beneficial to implement the inductors on the top metal layer

to minimize capacitive coupling to the substrate. The bottom metal layer is only being used to avoid crossings in multi-turn inductors. Inductors are quite predictable as they are defined by their geometry rather than the technology stack and they are modelled by a series inductance-resistance combination where the losses are described using a Q-factor. The Q-factor represents the frequency dependent ratio of the imaginary and real part of the inductor impedance. While a Silicon on Insulator (SOI) platform has the potential to enable the design of high-Q inductors, the substrate resistivity in the iSiPP platform is quite low (about  $10 \Omega \cdot \text{cm}$ ) resulting in spiral inductors with a Q-factor comparable to regular CMOS (i.e. with a Q-factor on the order of 10). Local removal of the substrate may thus enhance the performance of the RF passives on the iSiPP platform [29].

### 3.5.3 Design and Results for an LC-Matched Single Photodetector

While the method shown above helps to get a first idea of values for the inductor and capacitor, required values deviate and an iterative process is to be used. This is because the Q-factor will depend on the inductance value and because there are some added parasitics (e.g. inductance caused by finite trace length). To get the final design, the 2.5D Method of Moments (MOM) solver of ADS was used starting from the values given in table 3.4. The final design for a single photodetector is shown in Fig. 3.34 and its size is  $355 \mu\text{m}$  by  $234 \mu\text{m}$ .

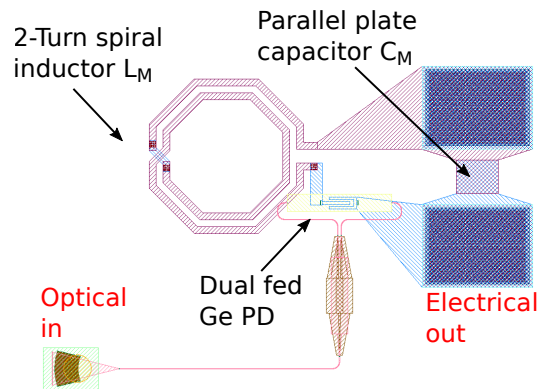


Figure 3.34: Layout of the implemented LC matched single-PD [26].

The performance of the matching network can be evaluated by looking at the output reflection coefficient  $S_{out}$ , which is shown in Fig. 3.35. It can

be seen that by changing the reverse biasing of the photodetector the frequency of optimal matching can be tuned over a wide range. Higher reverse voltages result in matching at higher frequencies due to the reduction in junction capacitance  $C_j$  of the photodetector. By tuning the photodetector reverse bias between 0 and 3V, a reflection coefficient lower than -20 dB is obtained over the frequency range between 24.3 and 30.4 GHz. Simulations and measurements are compared in Fig. 3.36 and the discrepancies can be explained by process tolerances and the fact that a simple photodetector model was used which does not include low-frequency effects.

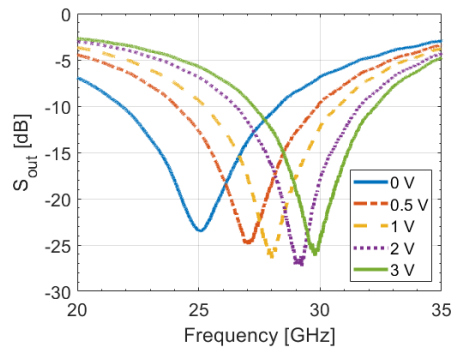


Figure 3.35: Reflection coefficient at the output of the LC matched Ge photodetector as a function of the reverse bias [26].

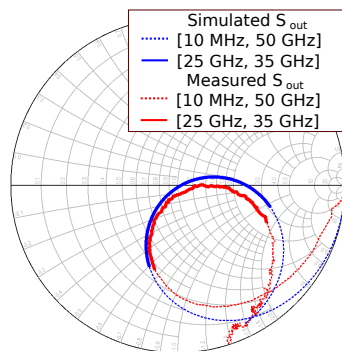


Figure 3.36: Comparison between the measured  $S_{out}$  at 3V and the simulated  $S_{out}$  (single PD) [26].

### 3.5.4 Design and Results for an LC-Matched 4-PD Array

The same procedure was repeated to match a 4-element detector array to a  $50 \Omega$  load at 30 GHz. The final layout of this design is shown in Fig. 3.37. The output impedance is shown in Fig. 3.38 and a comparison to the simulations is displayed in Fig. 3.39. In the design, a star coupler was used to preserve the high linearity obtained from adopting a multi-PD structure. A multi-detector structure results in a higher output capacitance and a lower output resistance resulting in a smaller matching inductance  $L_M$  and larger matching capacitance  $C_M$ . This is visible in the sense that a one-turn spiral inductor suffices and that the parallel plate capacitor becomes larger. The total size of this device is  $442 \mu\text{m}$  by  $298 \mu\text{m}$ .

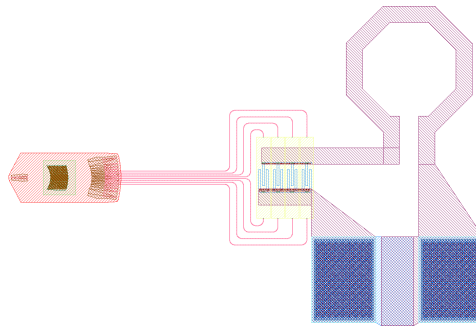


Figure 3.37: Layout of the implemented LC matched 4-PD array design.

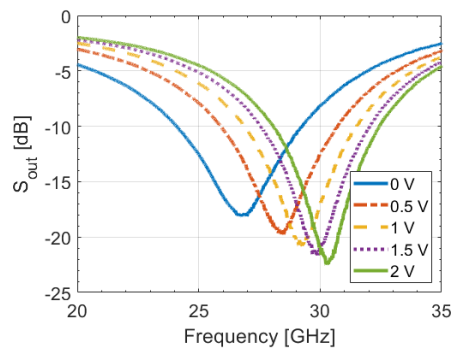


Figure 3.38: Reflection coefficient at the output of the LC matched 4-PD array as a function of the reverse bias.

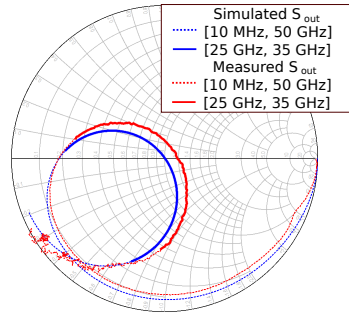


Figure 3.39: Comparison between the measured  $S_{out}$  at 2V and the simulated  $S_{out}$  (4-PD array).

### 3.5.5 Linearity

*Linearity measurements are not performed due to yield issues in the active devices for the fabricated wafer.*

However, the detectors used in these LC matched PD-arrays are intrinsically the same as the detectors used in the TWPD structures. Therefore, it is expected that the saturation current per photodetector is the same. Linearity limitations of the LC-matched detector array can be attributed to three contributions. First of all, the optical feeding network can suffer from two-photon absorption. However, we can ignore this contribution because a star coupler is used, which relaxes the on-chip optical power in the silicon waveguides. The second contribution relates to the optoelectronic power-to-current conversion. It was stated above that the detectors are intrinsically the same as for the TWPD and therefore should introduce identical power handling limits. Because the LC-matched detectors typically result in a higher conversion of generated current to output current sunk into the load (based on table 3.4), it can be concluded that the output power saturation is higher for the LC-matched detector array than for the TWPD. A final linearity aspect is related to the thermal contribution and we expect this to be worse for the LC-matched detector array since the detectors are located closer to each other, however it is not clear to what extent this will limit the overall linearity of the device.

## 3.6 Conclusion

Centralization is key in making cell densification in future wireless network architectures viable. Typical implementations of an ARoF link comprise

electrical amplification at the antenna. Shared amplification for multiple remote antenna units could be considered to further centralize the telecom infrastructure. Optical amplification at the CO will result in high optical powers and consequently requires high-linearity opto-electronic conversion at the remote antenna units.

To improve the linearity of the detector, the number of photodetectors should be increased such that each PD receives less power and space charge effects are consequently reduced. In literature, the power distribution network is typically implemented with a power splitting tree but this results in high optical on-chip power levels before the splitting occurs. Adopting a star coupler helps to preserve the high linearity of the traveling wave detector by combining on-chip coupling and power splitting functionality and thereby reducing two-photon absorption non-linearities. This proved to be a useful building block in the design of high-power monolithically integrated Ge-on-Si detectors. It was shown in this chapter that the TWPD is capable of combining high linearity with high bandwidth.

In this dissertation, narrowband applications are targeted hence the high-bandwidth property is not really required and optimal power conversion only needs to be available around the RF frequency. Therefore, monolithically integrated narrowband matching was looked at in section 3.5. Such resonantly matched detector arrays appear to outperform the traveling wave devices when high Q-factor passives are used. For the iSiPP platform, the Q-factor of the inductors is rather limited but this can be improved by using a platform with a higher substrate resistivity or using a local etch step. Even when poor-quality inductors are used, it is found that the narrowband solutions are at least comparable with the traveling wave design while requiring less space on the PIC and relaxing velocity matching requirements.

## References

- [1] C. H. Cox, E. I. Ackerman, G. E. Betts, and J. L. Prince, "Limits on the performance of RF-over-fiber links and their impact on device design," *IEEE Transactions on Microwave Theory and Techniques*, vol. 54, no. 2, pp. 906–920, February 2006.
- [2] G. P. Agrawal, *Fiber-Optic Communication Systems*, 4th ed. Wiley, 2010.
- [3] M. Piels and J. E. Bowers, "Photodetectors for silicon photonic integrated circuits," in *Photodetectors: Materials, Devices and Applications*, B. Nabet, Ed. Woodhead Publishing, 2015, ch. 1, pp. 3–20.
- [4] H. Chen, P. Verheyen, P. De Heyn, G. Lepage, J. De Coster, P. Absil, G. Roelkens, and J. Van Campenhout, "High-Responsivity Low-Voltage 28-Gb/s Ge p-i-n Photodetector With Silicon Contacts," *Journal of Lightwave Technology*, vol. 33, no. 4, pp. 820–824, February 2015.
- [5] Europractice, "imec-ePIXfab SiPhotonics: iSiPP50G," Accessed: June 2019. [Online]. Available: [http://www.europractice-ic.com/SiPhotonics\\_technology\\_imec\\_ISIPP50G.php](http://www.europractice-ic.com/SiPhotonics_technology_imec_ISIPP50G.php)
- [6] M. Pantouvaki, S. A. Srinivasan, Y. Ban, P. De Heyn, P. Verheyen, G. Lepage, H. Chen, J. De Coster, N. Golshani, S. Balakrishnan, P. Absil, and J. Van Campenhout, "Active Components for 50 Gb/s NRZ-OOK Optical Interconnects in a Silicon Photonics Platform," *Journal of Lightwave Technology*, vol. 35, no. 4, pp. 631–638, February 2017.
- [7] H. Chen, "Advanced Germanium p-i-n and Avalanche Photodetectors for Low-Power Optical Interconnects," Ph.D. dissertation, Ghent University, 2016.
- [8] A. Novack, M. Gould, Y. Yang, Z. Xuan, M. Streshinsky, Y. Liu, G. Capellini, A. E.-J. Lim, G.-Q. Lo, T. Baehr-Jones, and

- M. Hochberg, “Germanium Photodetector with 60 GHz Bandwidth using Inductive Gain Peaking,” *Optics Express*, vol. 21, no. 23, pp. 28 387–28 393, November 2013.
- [9] T. Ishibashi, T. Furuta, H. Fushimi, S. Kodama, H. Ito, T. Nagatsuma, N. Shimizu, and Y. Miyamoto, “InP/InGaAs Uni-Traveling-Carrier Photodiodes,” *IEICE Transactions on Electronics*, vol. 83, no. 6, pp. 938–949, June 2000.
- [10] D. Tulchinsky and K. Williams, “High Power RF Photodiodes,” *Optical Sciences*, pp. 193–195, 2005.
- [11] P.-L. Liu, K. J. Williams, M. Y. Frankel, and R. D. Esman, “Saturation Characteristics of Fast Photodetectors,” *IEEE Transactions on Microwave Theory and Techniques*, vol. 47, no. 7, pp. 1297–1303, July 1999.
- [12] K. J. Williams and R. D. Esman, “Design Considerations for High-Current Photodetectors,” *Journal of Lightwave Technology*, vol. 17, no. 8, pp. 1443–1454, August 1999.
- [13] K. Sun and A. Beling, “High-Speed Photodetectors for Microwave Photonics,” *Applied Sciences*, vol. 9, no. 4, February 2019.
- [14] C.-M. Chang, J. H. Sinsky, P. Dong, G. de Valicourt, and Y.-K. Chen, “High-power dual-fed traveling wave photodetector circuits in silicon photonics,” *Optics Express*, vol. 23, no. 17, pp. 22 857–22 866, August 2015.
- [15] T.-C. Tzu, K. Sun, R. Costanzo, D. Ayoub, S. M. Bowers, and A. Beling, “Foundry-Enabled High-Power Photodetectors for Microwave Photonics,” *IEEE Journal of Selected Topics in Quantum Electronics*, vol. 25, no. 5, September/October 2019.
- [16] X. Wu, H. Yu, Z. Fu, Q. Zhang, J. Yang, and X. Jiang, “A Silicon Aperiodically Distributed Traveling-Wave Photodetector With Enhanced RF Output Power,” *Journal of Lightwave Technology*, vol. 36, no. 16, pp. 3152–3161, August 2018.
- [17] Y. Zuo, Y. Yu, Y. Zhang, D. Zhou, and X. Zhang, “Integrated high-power germanium photodetectors assisted by light field manipulation,” *Optics Letters*, vol. 44, no. 13, pp. 3338–3341, July 2019.
- [18] M. J. Byrd, E. Timurdogan, Z. Su, C. V. Poulton, N. M. Fahrenkopf, G. Leake, D. D. Coolbaugh, and M. R. Watts, “Mode-evolution-based

- coupler for high saturation power Ge-on-Si photodetectors,” *Optics Letters*, vol. 42, no. 4, pp. 851–854, February 2017.
- [19] G. Chen, Y. Yu, X. Xiao, and X. Zhang, “High speed and high power polarization insensitive germanium photodetector with lumped structure,” *Optics Express*, vol. 24, no. 9, pp. 10 030–10 039, April 2016.
- [20] L. Bogaert, K. Van Gasse, G. Torfs, J. Bauwelinck, and G. Roelkens, “High-Power Traveling Wave Photodetector in Silicon Photonics with Monolithically Integrated Optical Power Splitter,” in *22nd Annual Symposium of the IEEE Photonics Society Benelux Chapter*, 2017, pp. 74–77.
- [21] L. Bogaert, K. Van Gasse, T. Spuesens, G. Torfs, J. Bauwelinck, and G. Roelkens, “Silicon Photonics Traveling Wave Photodiode with Integrated Star Coupler for High-Linearity mmWave Applications,” *Optics Express*, vol. 26, no. 26, pp. 34 763–34 775, December 2018.
- [22] L. Y. Lin, M. C. Wu, T. Itoh, T. A. Vang, R. E. Muller, D. L. Sivco, and A. Y. Cho, “High-Power High-Speed Photodetectors - Design, Analysis, and Experimental Demonstration,” *IEEE Transactions on Microwave Theory and Techniques*, vol. 45, no. 8, pp. 1320–1331, August 1997.
- [23] T. Spuesens, S. Pathak, M. Vanslembrouck, P. Dumon, and W. Bogaerts, “Grating Couplers With an Integrated Power Splitter for High-Intensity Optical Power Distribution,” *IEEE Photonics Technology Letters*, vol. 28, no. 11, pp. 1173–1176, June 2016.
- [24] A. R. Djordjevic, A. G. Zajic, D. V. Tasic, and T. Hoang, “A Note on the Modeling of Transmission-Line Losses,” *IEEE Transactions on Microwave Theory and Techniques*, vol. 51, no. 2, pp. 483–486, February 2003.
- [25] H. Jiang, D. S. Shin, G. L. Li, T. A. Vang, D. C. Scott, and P. K. L. Yu, “The Frequency Behavior of the Third-Order Intercept Point in a Waveguide Photodiode,” *IEEE Photonics Technology Letters*, vol. 12, no. 5, pp. 540–542, May 2000.
- [26] L. Bogaert, J. Verbist, K. Van Gasse, G. Torfs, J. Bauwelinck, and G. Roelkens, “Germanium Photodetector with Monolithically Integrated Narrowband Matching Network on a Silicon Photonics Platform,” in *21st European Conference on Integrated Optics*, 2019.

- 
- [27] M. S. Nezami, B. Radi, A. Gour, Y. Xiong, M. Taherzadeh-Sani, M. Menard, F. Nabki, and O. Liboiron-Ladouceur, “Integrated RF Passive Low-Pass Filters in Silicon Photonics,” *IEEE Photonics Technology Letters*, vol. 30, no. 23, pp. 2052–2055, December 2018.
  - [28] T. H. Lee, *The Design of CMOS Radio-Frequency Integrated Circuits*, 2nd ed. Cambridge University Press, 2004.
  - [29] A. Farsaei, R. Molavi, and S. Mirabbasi, “Modelling and Improving Performance of Inductors in a Silicon Photonics Process,” in *Advanced Photonics Congress, JTu4A.14*, 2016.

# 4

## Beamforming

### 4.1 Optical Beamforming Networks

Modulation and detection of the narrowband RF signal at the Remote Antenna Unit (RAU) is a critical part in the Radio over Fiber (RoF) architecture. A second important functional block is the addition of beamforming capabilities to the network. This will be key in mmWave communication as it helps to overcome the large path losses in the high-frequency wireless channel. Furthermore, beamforming will direct the transmit power to the intended user resulting in improved power efficiency of the mobile network. To start this chapter, several design considerations will be discussed. Firstly, optical beamforming networks will be compared with electrical variants. Secondly, it will be described why the beamforming functionality should not be centralized. Thirdly, narrowband solutions will be compared to broadband beamforming implementations. The rest of the chapter will consist of the design of a broadband beamforming device (true time delay via switchable optical delay lines, section 4.2) and the realization of a narrowband beamforming structure (phase steering with microrings, section 4.3). Finally, the comparison between the performance of narrowband and broadband solutions will be revisited in section 4.4, based on the fabricated devices.

### 4.1.1 Electrical or Optical Beamforming

Implementing the beamforming optically using integrated microwave photonics has some distinct benefits over the electrical implementations [1–4]. Firstly, Optical Beamforming Networks (OBFNs) offer strongly improved immunity to electromagnetic interference. Furthermore, microwave photonics provides a platform that enables the realization of large delays at mmWave with low loss and small delay-dependent loss variations which in turn makes high bandwidth true time delay possible. OBFNs also bring the Optoelectronic (O/E) conversion closer to the antenna elements, such that the routing can be done optically and the connector loss to the antenna is heavily reduced. Additionally, OBFNs can reduce the cost, weight, size and power consumption compared to traditional electrical implementations. Lastly, it is important to mention that carrier frequencies for mobile communication networks tend to increase over time and that OBFNs are more scalable in that respect due to the high processing bandwidth available in the optical domain.

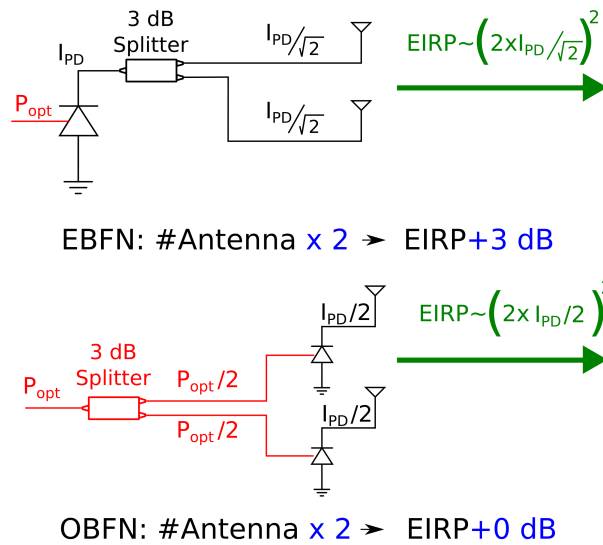


Figure 4.1: Beamforming gain: optical versus electrical beamforming.

The main drawback of OBFNs over electrical beamforming networks is the absence of passive beamforming gain. When the number of antenna elements is doubled in an Electrical Beamforming Network (EBFN), there

will be a 3 dB increase in beamforming gain. When the number of antenna elements is doubled in an OBFN, no beamforming gain is observed. This is caused by the fact that 3 dB power splitting in the electrical domain results in RF signals that are 3 dB lower at the antenna while 3 dB splitting in the optical domain results in signals 6 dB lower at the antenna after O/E conversion, as can be seen in Fig. 4.1. Consequently, the electrical power extracted from the Photodetector (PD) in the EBFN schematic is two times the total electrical power extracted from the two PDs in the OBFN schematic. However, the other advantages of beamforming still hold: interference between users decreases and beamforming helps to reduce overall power consumption since the linearity of the transmitters can be reduced.

#### 4.1.2 Centralized or Distributed Beamforming

One of the trends in future mobile communication networks is to centralize the main functionality to reduce complexity and cost at the RAU. Unfortunately, beamforming at the central office would require the RoF network to transport the signal for every individual antenna element, resulting in a tremendous increase of data to be transferred from the central office to the remote antenna units.

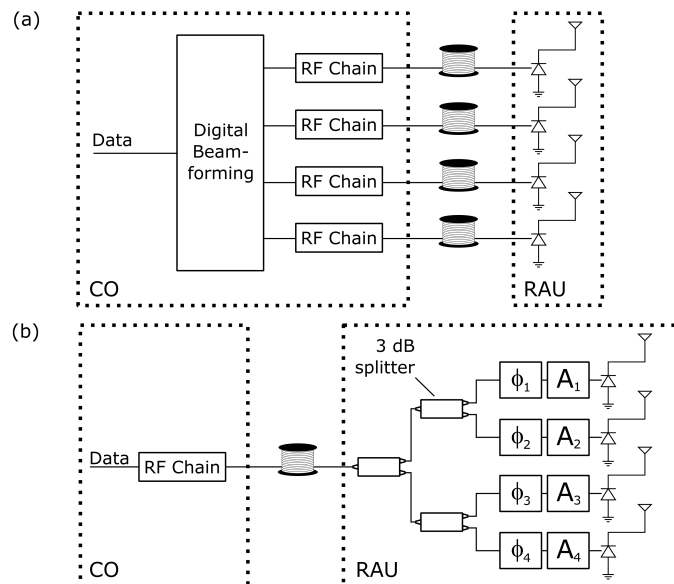


Figure 4.2: (a) Centralized digital beamforming (b) Distributed analog beamforming – CO: Central Office; RAU: Remote Antenna Unit.

For a typical 5G mmWave antenna array configuration, 64 to 256 antenna elements are expected per RAU. This shows that centralized beamforming tends to become unscalable. Analog beamforming offers the solution to this scaling issue [5–7]. In this distributed approach, the data passed over the network no longer scales with the antenna count but scales with the number of parallel beams to be emitted by the RAU. At the remote antenna unit, the signal is split in equal portions and the beamforming coefficients are applied before feeding the different versions of the same signal to the different antennas in the array (Fig. 4.2).

### 4.1.3 True Time Delay or Phase steering

Two phased antenna array solutions are discussed in this chapter. First True Time Delay (TTD) will be discussed in section 4.2 as a broadband beamforming solution. Subsequently, phase steering is looked at in section 4.3 offering an inherently narrowband beamforming technique. True time delay is required to avoid beam squint in broadband wireless communication (Fig. 4.3). Beam squint is the effect where the beamsteering angle deviates from the desired value for frequencies deviating from the center frequency [8]. This effect is however small when narrowband communication is targeted (small fractional bandwidth) and/or when the antenna array size is limited [9, 10]. In that scenario, phase steering solutions can be deployed. Firstly, a size reduction can be expected for phase steering beamforming networks. Furthermore, improved flexibility is found for phase steering compared to true time delay. Whereas TTD requires a maximum delay which scales with the physical dimensions of the antenna array, phase steering requires tuning capabilities between 0 and  $2\pi$  independent of the antenna array topology and size. Apart from the reduction in size and the increased flexibility and upgradability, the phase steering technique is also more suited for high RF carriers. When the RF carrier is increased, phase steering becomes easier since data and carrier are spaced further apart and are therefore easier to separate. True time delay on the other hand becomes harder since a smaller delay resolution is required with high accuracy.

## 4.2 True Time Delay

### 4.2.1 True Time Delay Architectures

Broadband frequency independent beamforming requires a true time delay implementation of the beamforming network. There are a multitude of techniques that can be used to implement a time delay in the optical domain.

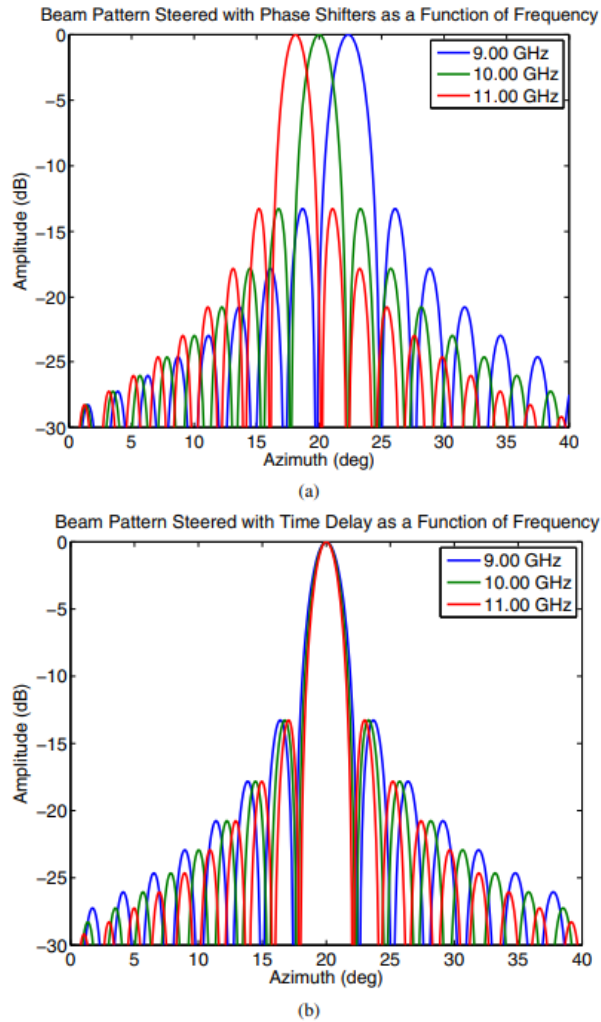


Figure 4.3: Beam squint – Phase steering versus TTD [8]

Two techniques are often adopted in literature when integrated true time delay is desired. On the one hand, Optical Ring Resonators (ORRs) can be used to trap the light in a ring resonator and by tuning the waveguide-ring coupling, the group delay can be changed [11–13] as can be seen in Fig 4.4. This solution allows for continuous tuning of the delay but it is a resonant solution and the delay element becomes even more narrowband when larger delays are desired.

On the other hand, Switchable Optical Delay Lines (SODLs) can be used [14, 15]. The total delay of the thermally tuned binary SODL shown in

Fig. 4.5 is  $b_1.T+b_2.2T+b_3.4T+b_4.8T$  with  $b_i$  equal to 0 or 1 depending on whether the short or long path was chosen respectively. Since the same SODL is used for each antenna element, the absolute time delay is irrelevant and the beamforming direction is determined by the relative delay difference between the different SODLs.

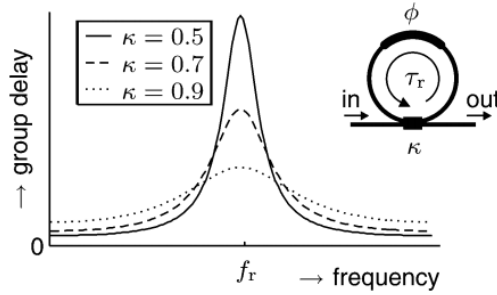


Figure 4.4: Optical ring resonator: Group delay [13].

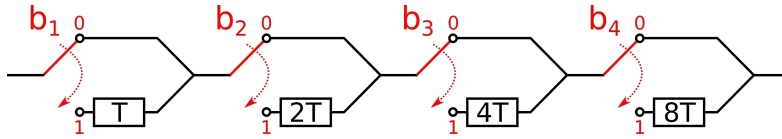


Figure 4.5: Switchable optical delay line.

The main drawback of this switched true time delay solution is the loss of continuous tunability. To counter this, both TTD architectures can be combined [16]. In such a structure, the SODL offers large-range coarse tuning of the optical delay while the ORR is used to perform small-range fine tuning of the delay. Consequently, such a device combines the continuous tunability feature of the ORR technique with the possibility to achieve large delays with a high bandwidth because these large delays are realized using the high-bandwidth SODL architecture.

## 4.2.2 Specifications

In this chapter, OBFNs for  $4 \times 1$  uniform linear antenna arrays are devised. The TTD solution implemented in this dissertation uses a binary SODL with **5-bit** tunability, a **1.6 ps tuning resolution** and hence a **tuning range of 49.6 ps**.

Introducing relative delay differences between the signals fed to the different antenna elements changes the angle with which the wavefronts leave

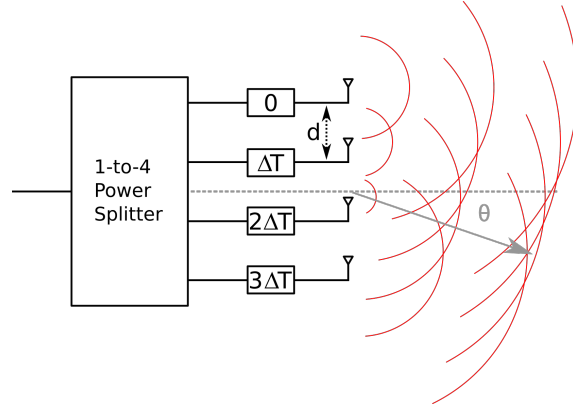


Figure 4.6: Beamforming: resulting wavefronts.

the antenna array and therefore the direction of the beam [11]. The angle of incidence can be calculated based on the delay difference  $\Delta T$  between consecutive antenna elements (Fig. 4.6). The element spacing  $d$  is typically chosen to be equal to half the wavelength to make sure that no significant side lobes are present in the emission pattern of the antenna array. At **28.5 GHz**, this means that the **angular resolution** of the OBFN is **5.2 degrees** and the **maximum angle is 70.5 degrees** according to equation 4.1. In this equation,  $\Delta T$  denotes the relative delay between consecutive elements,  $d$  denotes the antenna spacing and  $c$  is the speed of light constant.

$$\sin(\theta) = \frac{c\Delta T}{d} \quad (4.1)$$

### 4.2.3 First Generation TTD

#### 4.2.3.1 Design

The first generation TTD device is fabricated on the discontinued ePIXfab-imec SiPhotonics Passives platform. This platform includes 220nm waveguides, grating couplers and Multi Mode Interferometers (MMIs) but requires further processing steps to deposit the heaters and route the heater contacts to the side where they are accessible via a bondpad array. First, the bare Silicon on Insulator (SOI) design will be discussed and next the post processing steps will be covered. The design consists of six major parts that are discussed below and the final structure can be seen in Fig. 4.8:

1. **Fiber array:** To provide easy optical coupling to and from the chip, a grating coupler array is added to the design. The grating coupler

pitch is  $127 \mu\text{m}$  and the two outer grating couplers are interconnected to ease fiber array alignment.

2. **1-to-4 power splitter:** The input signal is split in 4 equal portions by cascading two 1-to-2 MMIs.
3. **Delay lines:** The overall delay experienced by the optical signal depends on the path taken through the SODL. Due to the binary nature of the SODL the delay difference between the short and long path increases by a factor 2 from one control bit to the next. The delay can be calculated by using equation 4.2. In this equation,  $c$  denotes the speed of light while  $n_g$  describes the group index which is 4.26 at  $1550 \text{ nm}$  for  $450 \text{ nm}$  wide,  $220 \text{ nm}$  high strip waveguides. Hence, the realized delay approximates  $1 \text{ ps}$  per  $70 \mu\text{m}$ .

$$\Delta T = \frac{\Delta L}{c/n_g} \quad (4.2)$$

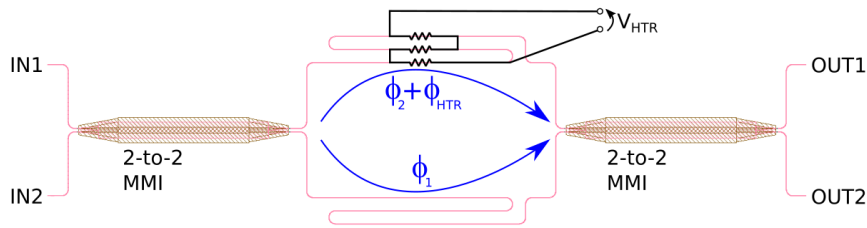


Figure 4.7: Thermal switch.

4. **Thermal switches:** To select the desired path, a thermal switch is present for every control bit (Fig. 4.7). Due to the thermal nature of the switch, response speeds on the order of  $10 \mu\text{s}$  are expected. In Fig. 4.7,  $\phi_1$  and  $\phi_2$  are random due to process variations. Adjusting the heater drive to make sure that  $\phi_2 + \phi_{HTR} - \phi_1$  is an integer multiple of  $2\pi$  results in the thermal switch to be in its cross state. When the heater drive is set to a value that makes  $\phi_2 + \phi_{HTR} - \phi_1 - \pi$  equal to an integer multiple of  $2\pi$ , the thermal switch is in its bar state.
5. **Power monitor:** Bar and cross voltages of the individual switches are not known a priori due to process variations. To enable the characterization of the chip, directional couplers are added to each short delay segment tapping of  $2.5 \%$  of the optical power and sending it to a grating coupler.

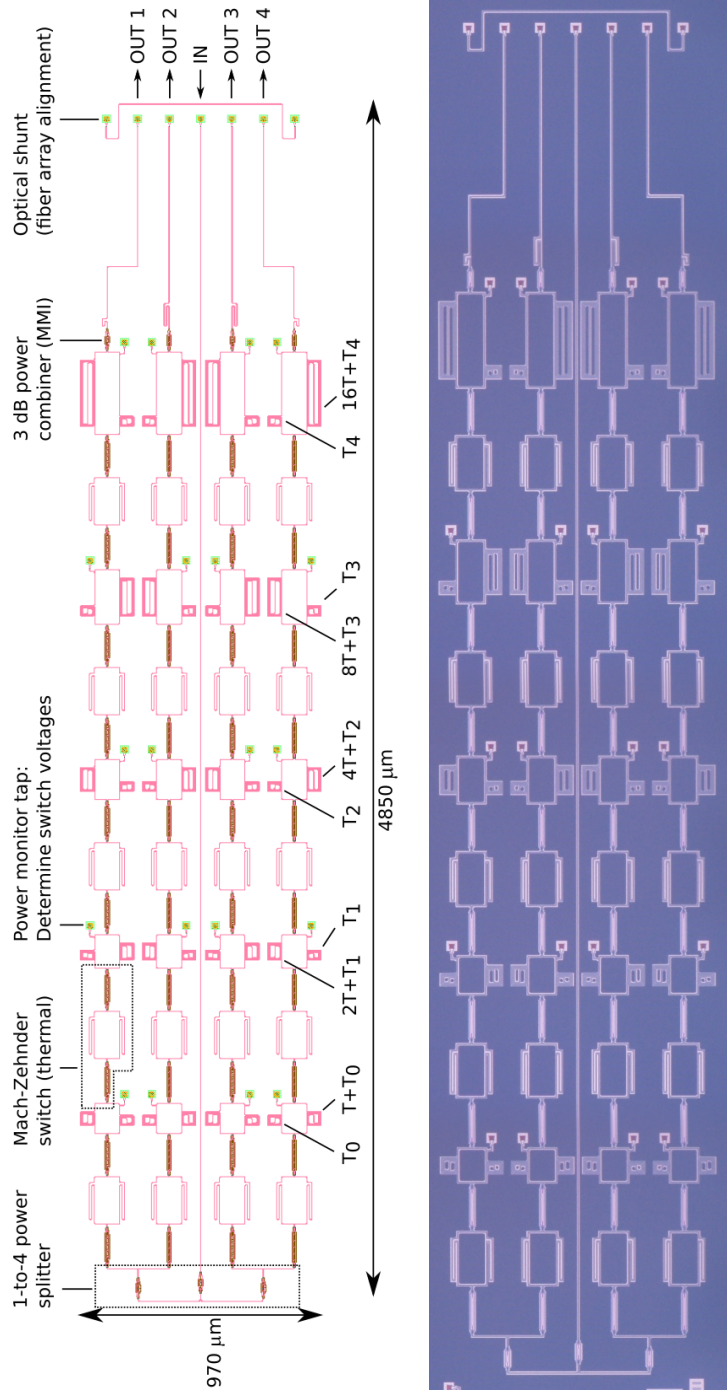


Figure 4.8: True time delay optical beamforming network generation 1: (top) annotated design (bottom) microscope image.

6. **3 dB combiner:** The last switch at the output is replaced by a 3 dB combiner. This reduces the driving complexity since each SODL requires one control signal less. Additionally, it results in a more compact design. However, this 3 dB combiner introduces an inherent 3 dB loss and is therefore one of the things that was changed in the second generation TTD device.

#### 4.2.3.2 Post-Processing

The designed device discussed in the previous section should subsequently go through several post-processing steps to add heaters [17] and make sure that the heater inputs are routed to a bondable bondpad array. The wafer from which we start is the aforementioned 220nm SOI platform containing the desired passive structures with 1.25  $\mu\text{m}$  topoxide. Two metal layers are subsequently deposited. The first is a high-ohmic metal layer which is a combination of 150 nm Ti and 15 nm Au. This layer is used to implement the heaters (Fig. 4.9), which were designed to be 2  $\mu\text{m}$  wide and approximately 500  $\mu\text{m}$  long and have a resistance of about 1 k $\Omega$ . The heating efficiency of these structures is measured to be approximately 16 mW per  $\pi$  phase shift. A second metal layer that was deposited is a low-ohmic metal layer which is used to route the contacts of the heaters to a bondpad array at the side. These bondpads are also implemented with the second metal layer. This layer consists of 40 nm Ti and 800 nm Au. The final step consists of adding BenzoCycloButene (BCB) and subsequently opening up the bondpads partially. This is required to make sure that the bondpads can be wirebonded without the gold being torn off.

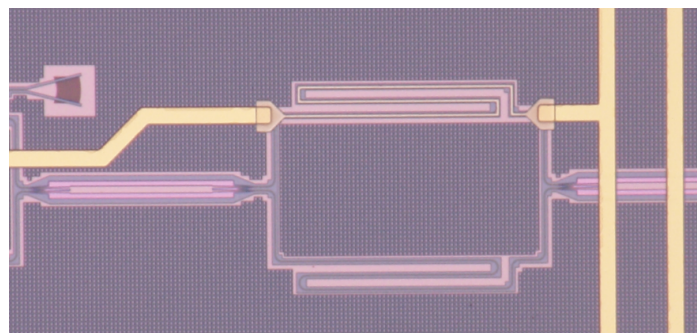


Figure 4.9: Thermal switch post-processing.

### 4.2.3.3 Delay Measurement

To characterize the TTD network, a single channel tunable delay cell was measured. This single channel delay cell is intrinsically the same as the delay lines in Fig. 4.8 but does not include the 6 dB splitting loss nor does it require a fiber array to be tested. The measurement setup required for the delay characterization is shown in Fig. 4.10. A sine (e.g. 28 GHz) is modulated on a 1550 nm Continuous Wave (CW) laser light and this modulated light is then split in two where most of the light (90 %) is fed to the tunable delay line before going to a photodetector and the reference light (10 %) is fed immediately to a photodetector. The photodetector outputs are subsequently compared to each other with an oscilloscope. For each delay setting, the time delay between the sine waves at the two outputs (TTD cell and reference path) is measured. Subsequently, the offset delay between the two paths is deducted from the shortest delay setting and this value is used as a calibration for the delay difference in the other delay settings. Since the delay is deducted from phase differences between the two sine waves, the initially obtained delay values are found modulo one period of the sine wave resulting in a sawtooth dependence of the realized delay on the delay setting.

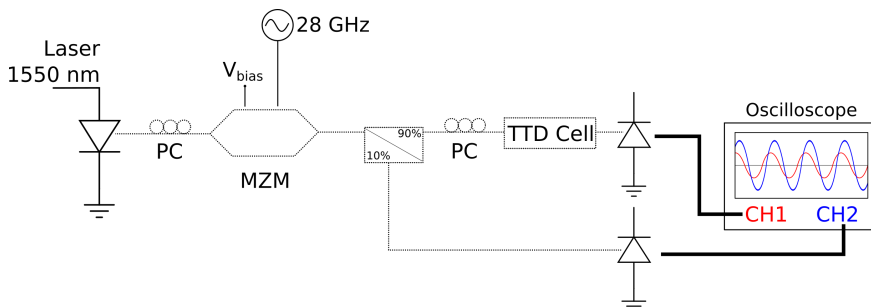


Figure 4.10: Optical delay line measurement setup.

The results of the delay measurements are shown in Fig. 4.11 after offset calibration for the 0 ps delay setting and the unwrapping of the sawtooth curve. The measurements agree very well with the designed delay values. The maximum deviation between expected and measured delay values is 828 fs and the average deviation is 231 fs which is about 15 % of the delay resolution. These deviations can be attributed to measurement noise, variations on group index and waveguide length, and the finite extinction ratio of the switches.

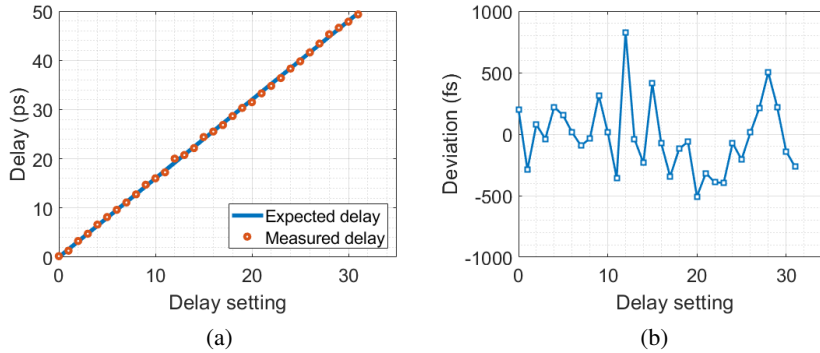


Figure 4.11: Optical delay line measurement results.

#### 4.2.4 Second Generation TTD

*At the time of writing this dissertation, the second generation OBFN devices were still under fabrication.*

A second version of the true time delay cell was designed on a 400nm SOI platform which again needs post-processing to implement the heaters. The main differences relative to the passive platform are changes in the dimensions of the basic building blocks (e.g. MMIs) and the use of a different group index which is measured to be about 3.82 at 1550 nm. Based on equation 4.2, the realized delay on this platform will be  $78.5 \mu\text{m}$  per ps. The second generation TTD device is shown in Fig. 4.12. It is again made for a 4 antenna element array and in contrast to the first generation device it can be used for the uplink. There are three important things to point out about this new device. Firstly, it was mentioned during the discussion of the previous TTD implementation that a 3 dB combiner was used at the output. This simplifies the driving scheme but it also introduces an inherent 3 dB insertion loss and is thus to be avoided. To make uplink beamforming possible, the 3 dB combiner should be replaced by a thermally controlled Mach Zehnder switch.

A second important addition is the fact that for the previous device grating couplers were used for initial calibration of the switches. These grating couplers are however only accessible one at a time and no longer available when a fiber array is attached. To solve this issue, markers are added next to the grating coupler to enable transfer printing [18] of monitor photodetectors to get real-time monitoring of the required switch voltages.

The third and final major difference can be found in the power division and

combination network to make the OBFN uplink-ready. For the downlink operation, the optical signal is split and the RF delays should be set correctly by the TTD network. For the uplink operation, it no longer suffices to only make sure that the RF delays are correct. It is also paramount that the optical carriers from each TTD cell align perfectly. If this is not the case, partial destructive interference will occur. To allow for optical phase matching of the signals coming from the different antenna elements, a thermal phase shifter is added in each branch and the 1-to-2 MMI splitters in the input network are replaced by 2-to-2 MMIs. The optical signals can then be optically aligned such that they constructively interfere by tuning the thermal phase shifters  $\phi_1$  to  $\phi_4$  such that the power in the photodetectors indicated with an asterisk in Fig. 4.12 is minimized.

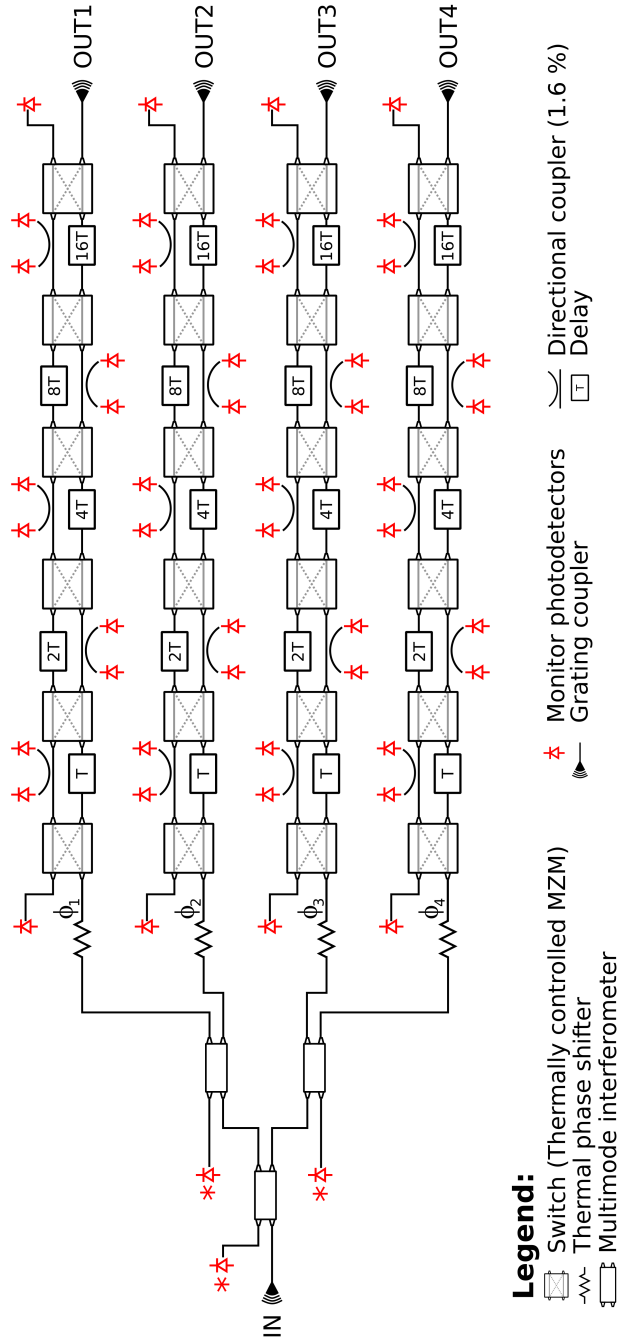


Figure 4.12: True time delay optical beamforming network generation 2.

## 4.3 Phase Steering

### 4.3.1 Concept

Phase steered OBFNs require the availability of RF phase shifters in the optical domain. To understand how one can implement such an optical RF phase shifter, it should first be discussed how the signal is converted from the optical to the electrical domain. As discussed before, this functionality is performed by a photodetector. The current generated by the photodetector is given by equation 4.3 where  $\mathcal{R}$  denotes the responsivity. This formula shows that applying a phase shift to the optical field will not have an impact on the photodetector current as it does not alter the optical power.

$$I_{PD}(t) = \mathcal{R} \times P_{opt}(t) \quad (4.3)$$

Equation 4.3 can be rewritten as eq. 4.4 where the received optical power is expressed as a sum of optical field components  $E_{opt,k}$  [19] where  $\omega_k$ ,  $A_k$  and  $\phi_k$  respectively describe the radial frequency, amplitude and phase of the k-th component of the optical field.

$$\begin{aligned} I_{PD}(t) &= \mathcal{R} \times |E_{opt,tot}(t)|^2 \\ &= \mathcal{R} \times \left| \sum_k E_{opt,k}(t) \right|^2 \\ &= \mathcal{R} \times \left| \sum_k A_k \exp[-j(\omega_k t + \phi_k)] \right|^2 \end{aligned} \quad (4.4)$$

Assume two optical field components arriving at the photodetector. The output current of the photodetector can then be described with formula 4.5. The difference between the frequencies of both optical field components will determine the RF frequency  $\omega_{RF}$  of the output current. In this equation, the subscript c describes the carrier component while the subscript d denotes the data component.

$$\begin{aligned} I_{PD}(t) &= \mathcal{R} \times \left| A_c \exp[-j(\omega_c t + \phi_c)] + A_d \exp[-j((\omega_c + \omega_{RF})t + \phi_d)] \right|^2 \\ &= \mathcal{R} [A_c^2 + A_d^2 + 2A_c A_d \cos(\omega_{RF} t + \phi_d - \phi_c)] \end{aligned} \quad (4.5)$$

It can be seen that one can tune the phase of the output sine wave when the phase of the carrier can be adjusted independently of the phase of the data. This is the principle that will be used for phase steering and it is

shown schematically in Fig. 4.13. Hence, optical RF phase shifters rely on the separation of carrier and data field components, the phase shifting of one of the two field components relative to the other and subsequently the recombination of the data and carrier fields.

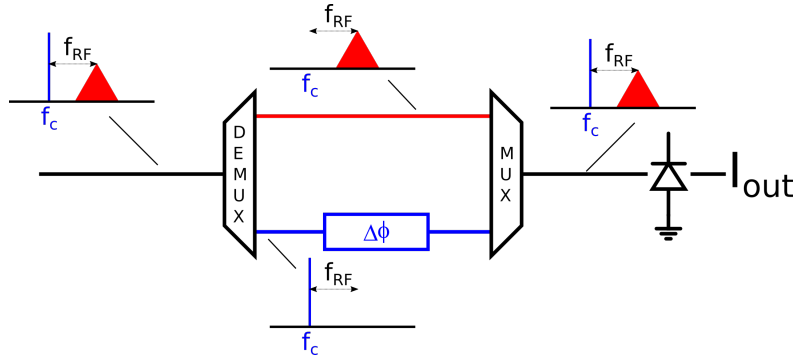


Figure 4.13: Phase steering principle.

The main difficulty in such an optical RF phase shifter lies in the need for (near-) perfect separation of carrier and data components. In this dissertation, carrier and data are separated by making use of high-Q Add Drop Ring Resonators (ADRRs) [20]. Photonic integrated RF phase shifters have been explored in literature [1, 21] where they are typically implemented with Mach Zehnder based structures. Due to the fact that our solution instead relies on microrings to separate data from carrier, our photonic integrated RF phase shifters will be significantly more compact. Furthermore, in this work the phase shifters are implemented thermally which further reduces the size and insertion loss compared to electro-optic variants. The speed of such a thermo-optic OBFN is on the order of several tens of microseconds and should be sufficient for quasi-static beamsteering [22]. If nanosecond beamsteering is required, electro-optic phase shifters should be used instead of thermo-optic phase shifters. Nevertheless, the idea of using ADRRs to implement the (de)interleaving of carrier and data components is still viable in such an electro-optic OBFN.

### 4.3.2 Optical Single Sideband

Up to now, the signal processed by the phase steered OBFN was assumed to be Optical Single Sideband (OSSB). In this section, it will be explained why this OSSB property simplifies the photonic RF phase shifter. Equation 4.5 can be rewritten as eq. 4.6 when an optical double sideband signal

is transmitted. Lsb and usb respectively denote the lower and upper sideband of the optical spectrum and they are assumed to be equally strong to simplify the discussion.

$$\begin{aligned}
I_{PD}(t) &= \mathcal{R} \times \left| A_{d,lsb} \exp[-j((\omega_c - \omega_{RF})t + \phi_{d,lsb})] \right. \\
&\quad \left. + A_c \exp[-j(\omega_c t + \phi_c)] + A_{d,usb} \exp[-j((\omega_c + \omega_{RF})t + \phi_{d,usb})] \right|^2 \\
&= I_{DC}(t) + I_{2\omega_{RF}}(t) + 2\mathcal{R}A_c A_d \left[ \cos(\omega_{RF}t + \phi_c - \phi_{d,lsb}) \right. \\
&\quad \left. + \cos(\omega_{RF}t + \phi_{d,usb} - \phi_c) \right] \\
&= I_{DC}(t) + I_{2\omega_{RF}}(t) + 4\mathcal{R}A_c A_d \left[ \cos\left(\phi_c - \frac{\phi_{d,lsb} + \phi_{d,usb}}{2}\right) \right. \\
&\quad \left. \times \cos\left(\omega_{RF}t + \frac{\phi_{d,usb} - \phi_{d,lsb}}{2}\right) \right]
\end{aligned} \tag{4.6}$$

In the previous section, the phase shifting was implemented by performing an optical phase shift on the carrier. In equation 4.6, the phase of the carrier is no longer present in the argument of the sine with frequency  $\omega_{RF}$  and hence the phase shifting can no longer be done in the same way. We are still able to do the phase shifting on the data components but the complexity increases heavily. Both the upper and lower sideband need to be separated from the carrier and each other. Additionally, antisymmetric phase shifting is required such that no parasitic amplitude modulation occurs. Hence, OSSB is preferred for photonic integrated RF phase shifting.

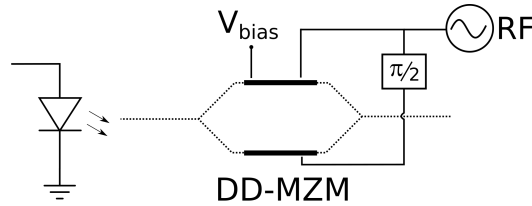


Figure 4.14: Optical single sideband generation with a DD-MZM.

With off-the shelf components one can easily generate OSSB data by quadrature driving [23] the two inputs of a Dual Drive MZM (DD-MZM) at its quadrature point as shown in Fig. 4.14. In [24], a monolithically integrated 28 GHz OSSB electroabsorption modulator was devised where the 90 degree RF phase shift required for OSSB data transmission is implemented optically on-chip.

### 4.3.3 Add Drop Ring Resonator

In this work add drop microring resonators [20] are used to deinterleave the carrier and data. The phase steering element is described in Fig. 4.15. The input signal is decomposed into the carrier and data by locking the input ring to the carrier wavelength. Subsequently, the carrier undergoes an optical phase shift by using a thermal phase shifter. Finally, the shifted carrier and original data are recombined by a second ring which is again locked to the carrier wavelength.

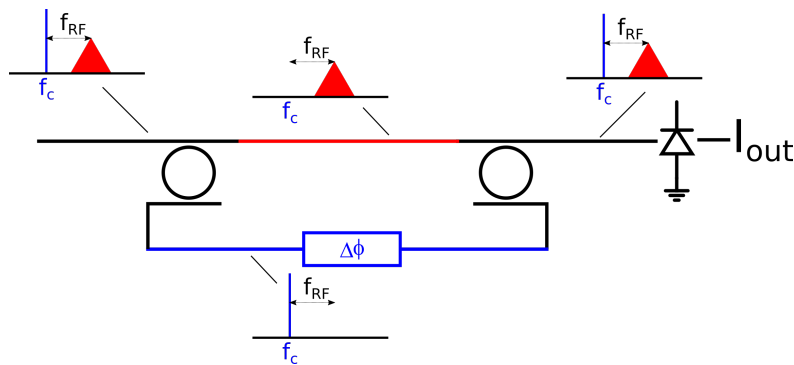


Figure 4.15: Phase steering principle with add drop ring resonators.

Ring resonators are temperature sensitive devices, and the center wavelength tends to shift 0.8 nm per 10 K. This 0.8 nm shift corresponds to about 100 GHz at 1550 nm and thus ring locking is required to stabilize the phase shifter. In practice, thermal control up to 0.125 degree centigrade is achievable resulting in a maximum shift of 10 pm of the center wavelength. The ADRRs used in this work are designed by ir. Jing Zhang and have a ring radius of 25  $\mu\text{m}$  resulting in a free spectral range of 3.6 nm (or equivalently 448 GHz).

In practice, ring resonators have a finite Q-factor. This unfortunately means that there will be data leakage through the carrier path (Fig. 4.16). Consequently, the data follows two paths and this introduces parasitic interference effects resulting in PM-to-AM conversion. To find out the impact of a finite Q-factor on the parasitic amplitude modulation, VPItransmissionmaker was used. The results of the parasitic PM-AM conversion are plotted in Fig. 4.17 where the output optical power reduction is given for different Quality factors in function of the phase setting of the optical phase shifters in the carrier path. The final ring design adopted in the phase steering OBFN has a Q-factor of approximately 30K resulting in a maximum parasitic amplitude modulation of 1.8%.

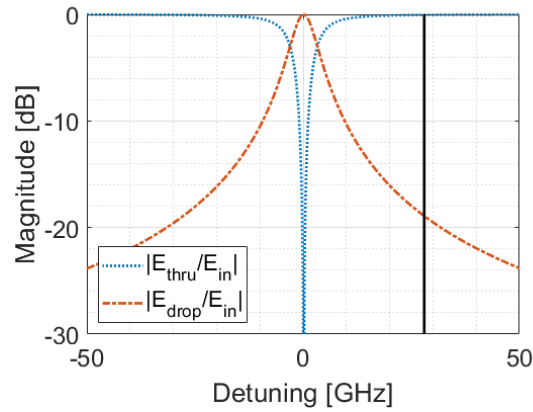


Figure 4.16: Transfer functions of the ADRR in function of frequency detuning ( $Q=30K$ ).

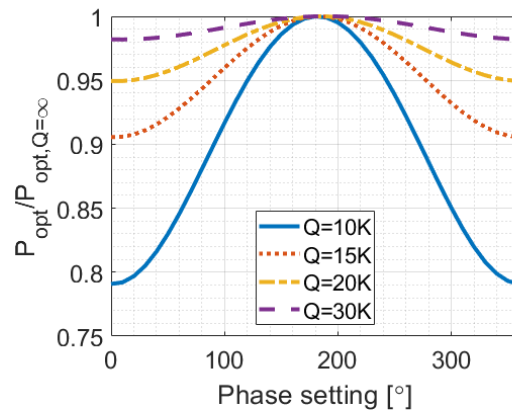


Figure 4.17: Parasitic PM-AM conversion due to finite  $Q$ -factor.

#### 4.3.4 First Generation Phase Steering

The first generation TTD device is fabricated on the discontinued ePIXfab-imec SiPhotonics Passives platform. This platform includes 220nm waveguides, grating couplers and MMIs but requires further processing steps to deposit the heaters and route the heater contacts to the side where they are made accessible via a bondpad array. The bare SOI design will be discussed while the required post processing steps were covered during the TTD discussion.

#### 4.3.4.1 Design

The first generation phase steering design before post-processing is shown in figures 4.19 (annotated layout) and 4.18 (microscope). The optical I/O uses a grating coupler array. The input is first split uniformly in four and each portion is subsequently passed on to a phase steering element (Fig. 4.15). Each phase steering element starts with an ADRR separating the data from the carrier. The carrier is subsequently thermally phase and amplitude modulated. After the beamsteering coefficients are set in the phase modulator  $\phi_i$  and amplitude modulator  $A_i$ , the data and carrier are recombined and passed on to the output of the OBFN. Grating couplers are added to the design to allow for power monitoring and in this way enable ring locking to the carrier wavelength.

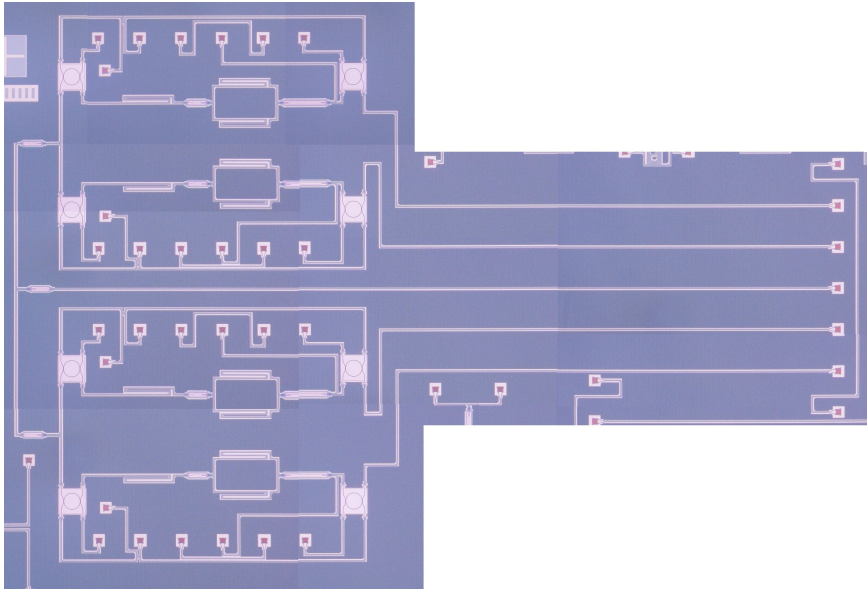


Figure 4.18: Phase steering optical beamforming network generation 1: microscope image.



#### 4.3.4.2 Post-Processing

Heaters and routing traces were deposited on the SOI design with  $1.25\ \mu\text{m}$  topoxide by using the same fabrication steps as for the TTD device. A microscope image is shown for the heaters deposited on the ADRR. It is important to mention that the heaters overlap the ring but not the coupling region to make sure that the Q-factor is unaltered when thermally shifting the center wavelength of the ring. The adopted ring design uses  $70\ \text{nm}$  shallow etched rib waveguides, has a  $500\ \text{nm}$  waveguide-ring gap and a ring radius of  $25\ \mu\text{m}$ . The ring heater resistance was measured to be approximately  $400\ \Omega$ .

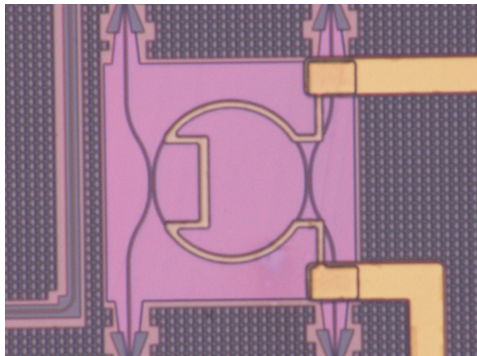


Figure 4.20: Microscope image of heater on add drop ring resonator

#### 4.3.4.3 Measurement

A first step to test the phase steering consists of characterizing the adopted ADRR as this is a critical component for the correct operation of the phase steering OBFN. The measured transfer characteristics are shown in Fig. 4.21. Unfortunately it is clear that the extinction ratio of the through port is very limited. Consequently, the carrier will be approximately equally strong in the data path as it is in the carrier path. This will result in very strong parasitic amplitude modulation effects and hence this phase steering device will not work adequately. Furthermore, the realised Q-factor appears to be only 10-15K instead of the designed value of 30K. No further experiments were performed with the phase steered OBFN since no good operation can be expected when the carrier and/or data are approximately equally strong in both the data and carrier arm.

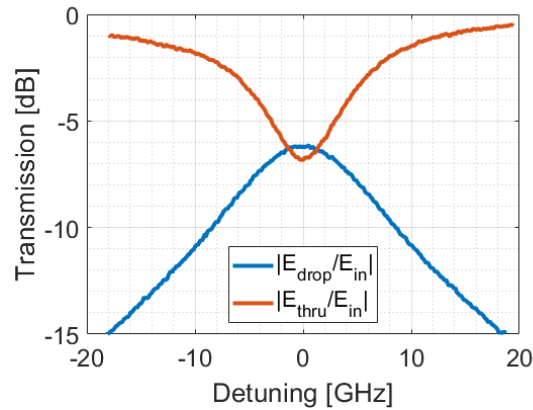


Figure 4.21: Measured transfer characteristics of the adopted ADRR

### 4.3.5 Second Generation Phase Steering

*At the time of writing this dissertation, the second generation OBFN devices were still under fabrication.*

A second version of the true time delay cell was designed on a 400nm SOI platform which again needs post-processing to implement the heaters. The main additions relative to the first generation device concern adjustments to the ring to improve its extinction ratio, the addition of the uplink and the addition of transfer printing markers. The latter is required for transfer printing of monitor photodetectors to allow real time ring locking. The final design is depicted in Fig. 4.22. In contrast with the thermal switches used for TTD, the switches in the phase steering OBFN are not only used for perfect bar or cross switching but can also be set in an intermediary state to implement the amplitude modulation.

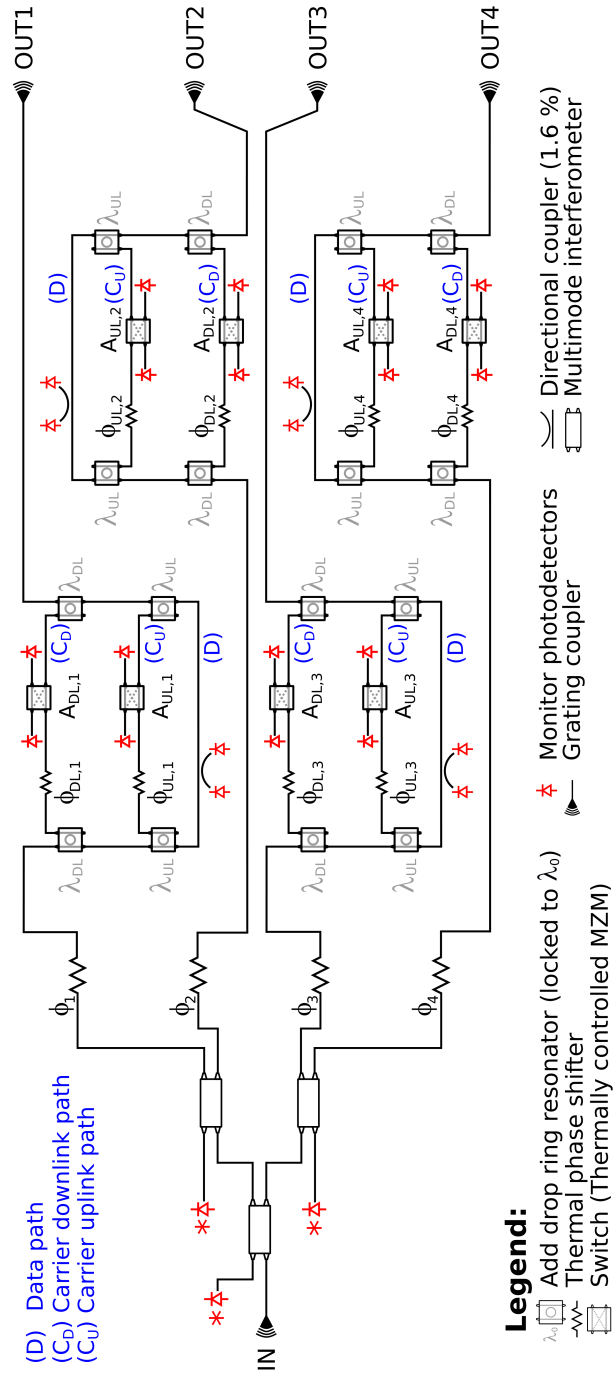


Figure 4.22: Phase steering optical beamforming network generation 2.

## 4.4 Performance Comparison of the Fabricated Optical Beamforming Networks

### 4.4.1 Size

For the phase steering solution, the photonic IC surface area required per antenna element per beam equals  $0.32 \text{ mm}^2$ . For the 5-bit switchable optical delay line implementation the required surface area increases to  $0.94 \text{ mm}^2$  per antenna element per beam. Furthermore, the phase steering element already includes amplitude tuning while this is not the case for the SODL which would result in an additional size increase for the SODL.

### 4.4.2 Power Consumption

To realize beamsteering, thermal control of the switches and microrings was adopted. The heating efficiency of these devices corresponds with 16 mW per  $\pi$  phase shift and the microring tuning efficiency of the resonance wavelength is 100 mW per FSR. On average this results in 96 mW power consumption per antenna element per beam for a 5-bit SODL where the output 3-dB coupler is replaced by an additional switch. For the phase steering structure, an average power consumption of 132 mW is expected per beam per antenna element. It should again be noted that the phase steering includes setting the amplitude coefficient while this is not the case for the SODL.

### 4.4.3 Beamsteering Speed

Due to the thermo-optic control of the OBFN, beamsteering speeds of several tens of  $\mu\text{s}$  are expected, both for the phase steering and SODL implementation. When shorter switching speeds are required, the thermo-optic phase shifters need to be replaced by electro-optic phase shifters. Apart from the different phase shifting scheme, the discussed architectures and conclusions still hold, e.g. high-Q microring resonators can be used to (de)interleave the carrier and data components. Optical beamforming networks relying on electro-optic phase shifting can offer nanosecond scale switching speeds and quasi-zero power consumption but they are significantly larger and introduce a higher insertion loss.

### 4.4.4 Insertion Loss and Variations

The insertion loss of the phase shifter depends on the Q-factor of the microrings. For the adopted ring with a Q-factor of 30K, the insertion loss

from the in- to the drop port is 1.3 dB, resulting in a total insertion loss of about 3 dB for the carrier path. Meanwhile, the data path experiences nearly no insertion loss. Hence, the phase shifter element based on rings with a Q-factor of 30K will introduce a total optical insertion loss of approximately 1.5 dB (eq. 4.5). Since electrical power scales quadratically with the optical power, this results in an equivalent electrical insertion loss of 3 dB. Additionally, the insertion loss will depend on the phase setting as shown in Fig. 4.17. For a Q-factor of 30K and thus a maximum parasitic amplitude modulation of 1.8%, the optical insertion loss is expected to have a maximum variation of 0.08 dB in the optical domain or equivalently 0.16 dB in the electrical domain.

In the SODL, the insertion loss depends on the path taken for each bit. The shortest delay per bit suffers an additional insertion loss of 0.11 dB due to the presence of a power tap, while the longest delay per bit suffers from an excess loss at a rate of 1.3 dB per cm extra waveguide. When replacing the final 3-dB coupler with an additional switch, as was done in the second iteration SODL, it can be found that the SODL introduces an optical loss between 4.225 dB and 4.59 dB depending on the delay setting. Hence the maximum insertion loss variation of the fabricated broadband solution is 0.365 dB in the optical domain or equivalently 0.73 dB in the electrical domain.

#### 4.4.5 Tuning Resolution and Range

Phase steering is continuously tunable over 0 to  $2\pi$ , hence every phase coefficient can be chosen. True time delay implementations relying on the SODL principle introduce a limit to the maximum achievable delay (49.6 ps) as well as the resolution (1.6 ps).

### 4.5 Conclusion

Due to the high propagation losses of the wireless channels at mmWave frequencies, beamforming capabilities are paramount in the next generation mobile communication networks. Furthermore, beamforming will help to improve the power efficiency of the network since the data is transmitted to the intended user instead of having signal emission in all directions. In this chapter, we first take a closer look at the different design choices. In the discussion of electrical versus optical beamforming it was shown that the main benefits of the optical variant include immunity to electromagnetic interference and the potential improvements in size, cost and power consumption.

Furthermore, OBFN offers large delays and high bandwidths at mmWave frequencies with low propagation loss. The main hurdle compared to the electrical beamforming networks is the lack of passive beamforming gain. A second design consideration is the question where it is best to implement the beamforming functionality. It was shown that due to scalability issues, beamforming should not be centralized but should be implemented using analog beamforming at the RAU. Two distinct beamforming solutions were covered. First, true time delay beamforming was implemented which offers squint-free beamforming. The constructed device is a binary switchable optical delay line offering 5-bit tunability of the delay with a 1.6 ps delay resolution and a total realizable delay of nearly 50 ps. The second beamforming network that was implemented is a narrowband device and relies on phase steering. It uses add drop microring resonators to separate carrier and data. Subsequently the carrier is phase-adjusted relative to the data component of the optical signal and after recombination of data with carrier by using a second microring, this same phase shift will be present in the RF signal. Unfortunately, this phase steering device did not operate as expected due to the limited extinction ratio of the fabricated microring.



## References

- [1] C. Porzi, G. Serafino, M. Sand, F. Falconi, V. Sorianello, S. Pinna, J. E. Mitchell, M. Romagnoli, A. Bogoni, and P. Ghelfi, “Photonic Integrated Microwave Phase Shifter up to the mm-Wave Band With Fast Response Time in Silicon-on-Insulator Technology,” *Journal of Lightwave Technology*, vol. 36, no. 19, pp. 4494–4500, October 2018.
- [2] R. Bonjour, M. Singleton, S. A. Gebrewold, Y. Salamin, F. C. Abrecht, B. Baeuerle, A. Josten, P. Leuchtmann, C. Hafner, and J. Leuthold, “Ultra-Fast Millimeter Wave Beam Steering,” *IEEE Journal of Quantum Electronics*, vol. 52, no. 1, January 2016.
- [3] Y. Liu, A. Wichman, B. Isaac, J. Kalkavage, E. J. Adles, T. R. Clark, and J. Klamkin, “Tuning Optimization of Ring Resonator Delays for Integrated Optical Beam Forming Networks,” *Journal of Lightwave Technology*, vol. 35, no. 22, pp. 4954–4960, November 2017.
- [4] Y. Liu, A. Wichman, B. Isaac, J. Kalkavage, E. J. Adles, T. R. Clark, and J. Klamkin, “Ultra-Low-Loss Silicon Nitride Optical Beamforming Network for Wideband Wireless Applications,” *IEEE Journal of Selected Topics in Quantum Electronics*, vol. 24, no. 4, July/August 2018.
- [5] S. Sun, T. S. Rappaport, R. W. Heath Jr., A. Nix, and S. Rangan, “MIMO for Millimeter-Wave Wireless Communications: Beamforming, Spatial Multiplexing, or Both?” *IEEE Communications Magazine*, vol. 52, no. 12, pp. 110–121, December 2014.
- [6] R. W. Heath Jr., N. Gonzalez-Prelcic, S. Rangan, W. Roh, and A. M. Sayeed, “An Overview of Signal Processing Techniques for Millimeter Wave MIMO Systems,” *IEEE Journal of Selected Topics in Signal Processing*, vol. 10, no. 3, pp. 436–453, April 2016.
- [7] M. Shafi, A. F. Molisch, P. J. Smith, T. Haustein, P. Zhu, P. De Silva, F. Tufvesson, A. Benjebbour, and G. Wunder, “5G: A Tutorial

- Overview of Standards, Trials, Challenges, Deployment, and Practice,” *IEEE Journal on Selected Areas in Communications*, vol. 35, no. 6, pp. 1201–1221, June 2017.
- [8] M. Longbrake, “True Time-Delay Beamsteering for Radar,” in *IEEE National Aerospace and Electronics Conference (NAECON)*, July 2012.
- [9] C. Tsokos, E. Mylonas, P. Groumas, L. Gounaridis, H. Avramopoulos, and C. Kouloumentas, “Optical Beamforming Network for Multi-Beam Operation With Continuous Angle Selection,” *IEEE Photonics Technology Letters*, vol. 31, no. 2, pp. 177–180, January 2019.
- [10] G. Serafino, C. Porzi, F. Falconi, S. Pinna, M. Puleri, A. D’Errico, A. Bogoni, and P. Ghelfi, “Photonics-Assisted Beamforming for 5G Communications,” *IEEE Photonics Technology Letters*, vol. 30, no. 21, pp. 1826–1829, November 2018.
- [11] M. Morant, A. Trinidad, E. Tangdiongga, T. Koonen, and R. Llorente, “5G NR Multi-Beam Steering employing a Photonic TTD Chip assisted by Multi-Core Fiber,” in *Optical Fiber Communications Conference and Exhibition (OFC)*, March 2019, w2A.41.
- [12] G. Choo, C. K. Madsen, S. Palermo, and K. Entesari, “Automatic Monitor-Based Tuning of an RF Silicon Photonic 1X4 Asymmetric Binary Tree True-Time-Delay Beamforming Network,” *Journal of Lightwave Technology*, vol. 36, no. 22, pp. 5263–5274, November 2018.
- [13] A. Meijerink, C. G. H. Roeloffzen, R. Meijerink, L. Zhuang, D. A. I. Marpaung, M. J. Bentum, M. Burla, J. Verpoorte, P. Jorna, A. Hulzinga, and W. van Etten, “Novel Ring Resonator-Based Integrated Photonic Beamformer for Broadband Phased Array Receive Antennas—Part I: Design and Performance Analysis,” *Journal of Lightwave Technology*, vol. 28, no. 1, pp. 3–18, January 2010.
- [14] Y. Liu, B. Isaac, J. Kalkavage, E. Adles, T. Clark, and J. Klamkin, “93-GHz Signal Beam Steering with True Time Delayed Integrated Optical Beamforming Network,” in *Optical Fiber Communications Conference and Exhibition (OFC)*, March 2019, th1C.5.
- [15] P. Zheng, C. Wang, X. Xu, J. Li, D. Lin, G. Hu, R. Zhang, B. Yun, and Y. Cui, “A Seven Bit Silicon Optical True Time Delay Line for Ka-Band Phased Array Antenna,” *IEEE Photonics Journal*, vol. 11, no. 4, August 2019.

- [16] X. Wang, L. Zhou, R. Li, J. Xie, L. Lu, K. Wu, and J. Chen, "Continuously tunable ultra-thin silicon waveguide optical delay line," *Optica*, vol. 4, no. 5, pp. 507–515, May 2017.
- [17] K. Van Acoleyen, "Nanophotonic Beamsteering Elements Using Silicon Technology for Wireless Optical Applications," Ph.D. dissertation, Ghent University, 2012.
- [18] J. Zhang, G. Muliuk, J. Juvert, S. Kumari, J. Goyvaerts, B. Haq, C. Op de Beeck, B. Kuyken, G. Morthier, D. Van Thourhout, R. Baets, G. Lepage, P. Verheyen, J. Van Campenhout, A. Gocalinska, J. O'Callaghan, E. Pelucchi, K. Thomas, B. Corbett, A. J. Trindade, and G. Roelkens, "III-V-on-Si photonic integrated circuits realized using micro-transfer-printing," *APL Photonics*, vol. 4, no. 11, p. 110803, November 2019.
- [19] G. P. Agrawal, *Fiber-Optic Communication Systems*, 4th ed. Wiley, 2010.
- [20] W. Bogaerts, P. De Heyn, T. Van Vaerenbergh, K. DeVos, S. K. Selvaraja, T. Claes, P. Dumon, P. Bienstman, D. Van Thourhout, and R. Baets, "Silicon microring resonators," *Laser & Photonics Reviews*, vol. 6, no. 1, pp. 47–73, January 2012.
- [21] V. J. Urick, M. J. Mondich, C. E. Sunderman, D. A. Kozak, P. G. Goetz, W. S. R.ovich, M. W. Pruessner, R. Mahon, and K. J. Williams, "Microwave Phase Shifting Using Coherent Photonic Integrated Circuits," November/December 2016.
- [22] A. Morgado, K. M. S. Huq, S. Mumtaz, and J. Rodriguez, "A survey of 5G technologies: regulatory, standardization and industrial perspectives," *Digital Communications and Networks*, vol. 4, no. 2, pp. 87–97, April 2018.
- [23] C. W. Chow, C. H. Wang, C. H. Yeh, and S. Chi, "Analysis of the carrier-suppressed single-sideband modulators used to mitigate Rayleigh backscattering in carrier-distributed PON," *Optics Express*, vol. 19, no. 11, pp. 10973–10978, May 2011.
- [24] J. Van Kerrebrouck, L. Bogaert, H. Li, C.-Y. Wu, P. Demeester, G. Roelkens, and G. Torfs, "Monolithically Integrated Quadrature EAM Structure for 28 GHz Full Duplex Radio over Fiber," in *24th Annual Symposium of the IEEE Photonics Society Benelux Chapter*, 2019.



# 5

## System Experiments

### 5.1 Introduction

In the previous chapters, the building blocks for implementing detection & modulation (chapter 2) and beamforming (chapter 4) in an Analog Radio over Fiber (ARoF) link were discussed. This chapter will describe system experiments performed with the components from chapter 2. First, the photoreceiver and reflective Electro-Absorption Modulator (EAM) driver were tested individually and the results are provided in sections 5.2 and 5.3. Subsequently, section 5.4 describes the fiber-wireless downlink and uplink based on the aforementioned GaAs electronics – Si photonics transceivers resulting in low-cost, laser-less Remote Antenna Units (RAUs) for scalable Radio Frequency over Fiber (RFoF) architectures.

*Due to the COVID-19 outbreak in 2020, system experiments with the optical beamforming networks designed in chapter 4 were postponed and are therefore not a part of this dissertation.*

## 5.2 Narrowband Photoreceiver

The work in this section has been published in [1, 2].

Two types of data transmission experiments are discussed. First, the performance of the photoreceiver is validated according to 5G New Radio Interface specifications nr257 and nr258 [3]. Secondly, the photoreceiver is tested as part of a high data rate link [4].

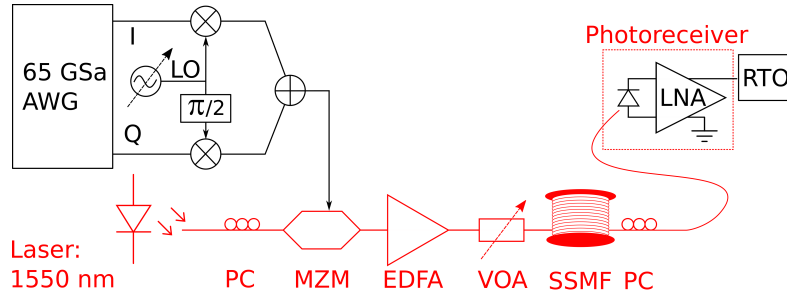


Figure 5.1: Setup used for photoreceiver link experiments (5G NR) [1].

The adopted setup for photoreceiver measurements is depicted in Fig. 5.1. The transmitter comprises a Continuous Wave (CW) laser, Polarization Controller (PC), Mach Zehnder Modulator (MZM), Erbium Doped Fiber Amplifier (EDFA) and Variable Optical Attenuator (VOA). The laser emits 13 dBm, 1550 nm CW light which is subsequently modulated by a quadrature biased MZM. The RF signal fed to the MZM is constructed by an I/Q-mixer (*Hittite HMC-1063*) where the in-phase (I) and quadrature (Q) signals are generated by an Arbitrary Waveform Generator (AWG) (*Keysight M8195A*) at an Intermediate Frequency (IF) frequency of 2.5 GHz. The Local Oscillator (LO) frequency can then be adjusted to choose the carrier frequency of the generated RF frequency. The adopted transmission scheme results in a modulation index of 0.15. Before transporting this signal to the receiver, the modulated light is first passed to an EDFA-VOA combination where the launched optical power is chosen. Subsequently the light passes through up to 21 km Standard Single Mode Fiber (SSMF). At the photoreceiver the light is converted back to the electrical domain, amplified and passed on to a Real-Time Oscilloscope (RTO) (*Keysight DSA-Z634A*). In this chapter, the Low Noise Amplifier (LNA) supply of the photoreceiver is set to 3 V.

### 5.2.1 5G New Radio

The 5G new radio standards nr257 and nr258 target channel bandwidths of 50, 100, 200 and 400 MHz [3]. In Fig. 5.2, the Error Vector Magnitude (EVM) is shown for an Optical Back-to-Back (OB2B) ARoF link under the influence of changing center frequency with baud rates of 100 and 400 MBd. In these experiments, single-carrier 16-QAM signals were used with a roll-off factor of 0.28 and 0 dBm on-chip optical power incident on the photodetector. To compensate bandwidth limitations in the probing setup and MZM transmission function, 9-tap equalization was used at the RTO. The EVM definition used in this dissertation is the EVM normalized to the average power. For ARoF communication in the nr257/nr258 bands, values of EVM stay below 2.46 and 3.47 % for 100 and 400 MBd channels respectively, which satisfies the 3GPP requirements for 16-QAM (< 12.5 %), 64-QAM (< 8 %) and 256-QAM (< 3.5 %) [5]. Furthermore, the ARoF tests were repeated for 16-QAM communication at a 28 GHz carrier over 10 and 21 km of SSMF. For 10 km SSMF the 100/400 MBd signals have an EVM of 2.09/3.24 %. When 21 km SSMF is used, this becomes 2.88/5.56 % (Fig. 5.3).

To complete the study of the presented photoreceiver for new radio channels nr257/258, a sensitivity analysis is performed at 28 GHz for 100 and 400 MBd signals using 3 and 9 tap equalization respectively. The results are depicted in Fig. 5.4. When the sensitivity would be depicted relative to the input optical power, the results would differ depending on the modulation depth. Therefore, the sensitivity study is performed relative to the output peak-to-peak voltage provided by the LNA to a 50  $\Omega$  load. When the 8 % EVM criterion is taken as a guideline, it is found that the  $V_{out,pp}$  of the LNA should be above 25 and 44 mV for 100 and 400 MBd communication respectively. This can be calculated back to the sensitivity of the RF photocurrent by taking into account the transimpedance of the LNA (865 V/A at 28 GHz) resulting in a sensitivity of 29 and 51  $\mu A_{pp}$  respectively.

### 5.2.2 High Data Rate

The photoreceiver was subsequently tested for high data rate applications. This is possible because of the combination of a low Noise Figure (NF) and a reasonably large bandwidth. The 3-dB bandwidth of the photoreceiver has been shown to be 8 GHz centered around 27.5 GHz. With a 0.28 roll-off factor, baud rates up to approximately 6 GBd are consequently possible.

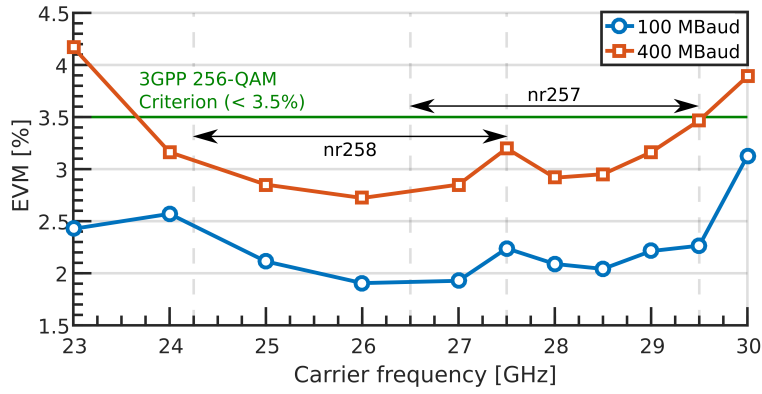


Figure 5.2: Photoreceiver – EVM as a function of the carrier frequency [2].

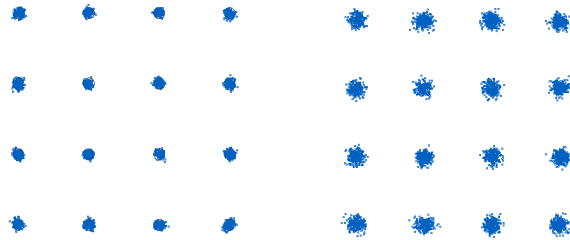


Figure 5.3: Photoreceiver – Constellation diagram at the RTO when transmitting (left) 100 MBd, (right) 400 MBd at 28 GHz over 21 km SSMF [1].

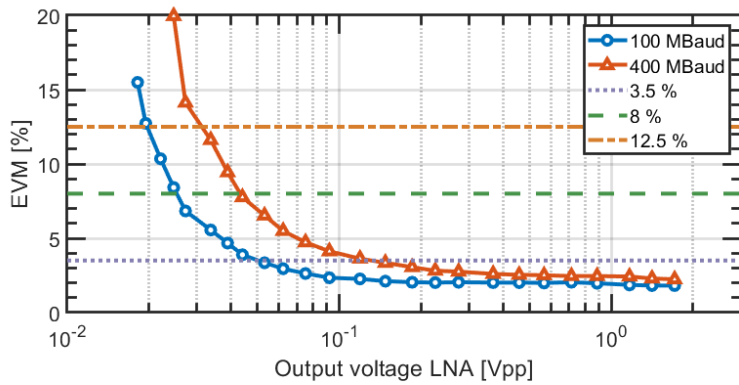


Figure 5.4: Photoreceiver – EVM as a function of the LNA  $V_{out,pp}$  [2].

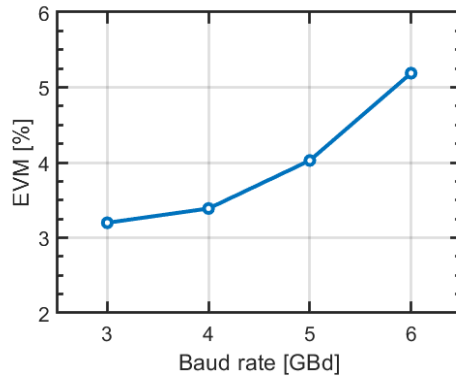


Figure 5.5: Photoreceiver – EVM as a function of the baud rate [2].

Implementing the same link as for the new radio experiments (Fig. 5.1) shows low Signal-to-Noise Ratio (SNR) at high baud rates because of the limited bandwidth of the mixer. To overcome this, the transmitter was replaced by a 92 GSa/s AWG followed by an LNA (*HMC-1040*) driving the MZM. Fig. 5.5 depicts the EVM as a function of the baud rate for an OB2B configuration. For these experiments the LNA was supplied with 3V and the incident power on the photodiode equals 0 dBm. The transmitted 16-QAM signal with roll-off of 0.28 was centered around 27.5 GHz and 41 tap equalization was used at the RTO to compensate for bandwidth limitations in the transmitter, MZM and probing setup. The received RF signal in OB2B configuration offers an EVM equal to 5.2 %, which is well below the 8% 3GPP criterion [5]. Constellation diagrams for 5 and 6 GBd 64-QAM ARoF links are shown in Fig. 5.6. Sending 4 GBd, 32-QAM over 21 km SSMF results in an EVM of 5.8% (Fig. 5.7).

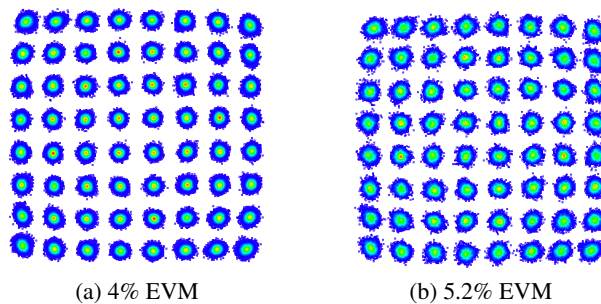


Figure 5.6: Photoreceiver – (a) 5 GBd, (b) 6 GBd at 27.5 GHz, OB2B [2].

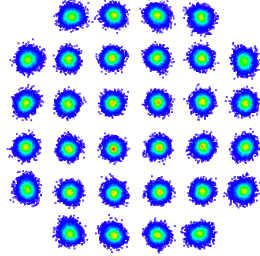


Figure 5.7: Photoreceiver – 4 GBd, 27.5 GHz, 21km SSMF [2].

### 5.3 Narrowband Reflective EAM Driver

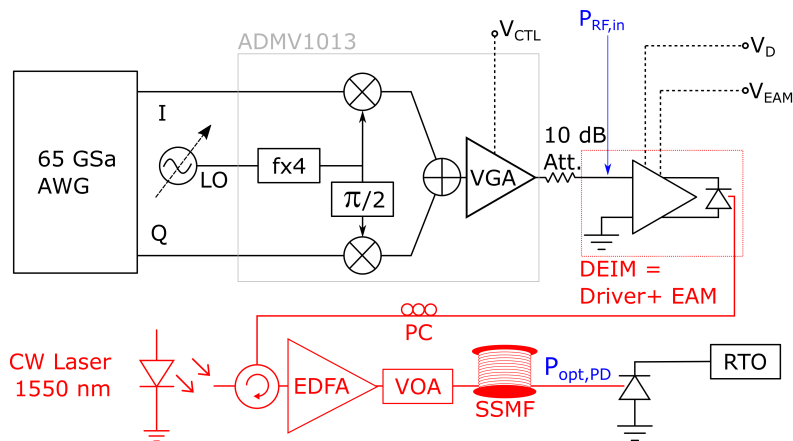


Figure 5.8: Setup used for EAM-driver link experiments (5G NR).

The adopted setup for the EAM-driver measurements is depicted in Fig. 5.8. The laser emits a 0 dBm, 1550 nm CW laser light which is passed on to the reflective EAM. A dedicated narrowband driver modulates this CW laser light with an RF signal that is generated by upconverting an IF signal at 2 GHz to the desired RF frequency with an I/Q-mixer (*ADMV1013*). This mixer includes a frequency quadrupler for the LO frequency and a Variable Gain Amplifier (VGA) at the output. This VGA allows for tuning of the RF power  $P_{RF,in}$  at the input of the driver. The driver is designed to modulate the received signal in the uplink path on an optical carrier. The signal amplitude of the uplink is typically low, hence, the signal injected in the driver needs to be attenuated (10 dB in Fig. 5.8). During the experiments in this section,  $P_{RF,in}$  was set to -34 dBm, which is 10 dB below

the 1-dB compression point at 1550nm for a 1V reverse biased EAM according to chapter 2. After the driver modulates the CW tone incident on the reflective EAM, the light couples from the Photonic Integrated Circuit (PIC) back into the fiber. An optical circulator is required to separate the CW laser light and the modulated light. Subsequently, an EDFA-VOA pair is used to set the optical power launched into the fiber. At the receiver side, a 50 GHz photodetector (*XPDV2120RA*) converts the light back to the electrical domain where an RTO is used to analyze the received signal. The Driver and EAM In Mirror (DEIM) assembly is used as EAM-driver where the EAM uses a 1V reverse bias and the driver uses a 2V bias. During the Orthogonal Frequency-Division Multiplexing (OFDM) measurements in section 5.4, the EAM reverse bias is increased to 2V, to cope with the large Peak-to-Average Power Ratio (PAPR) of the OFDM signals.

### 5.3.1 5G New Radio

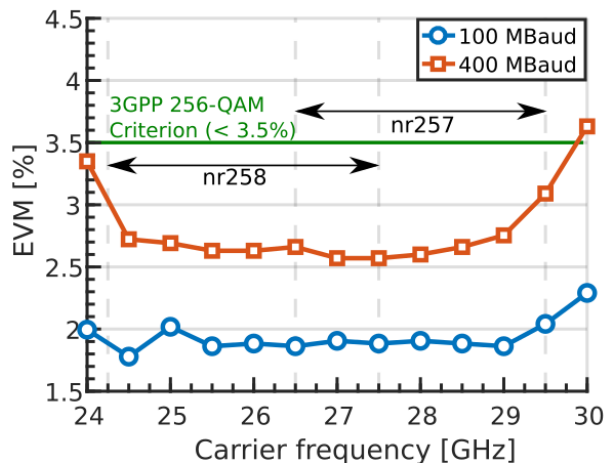


Figure 5.9: DEIM – EVM as a function of the carrier frequency.

The 5G new radio channels nr257/258 target bandwidths of 50, 100, 200 and 400 MHz [3]. In Fig. 5.9, the EVM is shown for an OB2B ARoF link (DEIM - 50GHz Photodetector) under the influence of changing center frequency with baud rates of 100 and 400 MBd. In these experiments, single-carrier 16-QAM signals were used with a roll-off factor of 0.28 and 8 dBm optical power incident on the photodetector. To compensate bandwidth limitations in the probing setup, 7-tap equalization was used at the RTO. For ARoF communication in the nr257/nr258 bands, values of EVM

stay below 2.04 and 3.09 % for 100 and 400 MBd channels respectively, which satisfies the 3GPP requirements for 16-QAM (< 12.5 %), 64-QAM (< 8 %) and 256-QAM (< 3.5 %) [5].

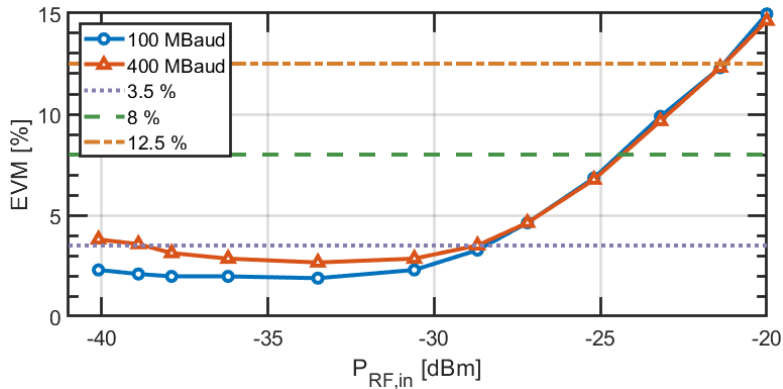


Figure 5.10: DEIM – EVM as a function of the RF input power.

A sensitivity analysis for the OB2B link with the DEIM as transmitter and 50 GHz photodetector as receiver is shown in Fig. 5.10 for 100 and 400 MBd data transmission. The increase in EVM at higher input powers is due to the non-linearities arising in the DEIM and this limit is the same for 100 and 400 MBd signals. The increase in EVM at lower input powers is due to Relative Intensity Noise (RIN) and can thus be lowered by repeating the experiment using a laser with a lower RIN. At these lower powers, we can clearly see a difference in signal quality between 100 and 400 MBd data transmission. The EVM measurement over the new radio bands nr257/258 (Fig. 5.9) was performed with -34 dBm input RF power in the driver. At those power levels, non-linearities have a minor impact on the signal quality.

### 5.3.2 High Data Rate

For the high data rate experiments discussed in this section, the same setup as depicted in Fig. 5.8 is used. The IF frequency is increased to 3 GHz, the RF carrier frequency is set to 27 GHz and a 41-tap equalizer is used. Fig. 5.11 depicts the EVM as a function of the baud rate for an OB2B configuration. Hence with the link discussed in Fig. 5.8, up to 4 GBd can be transmitted with EVM values below 7.59%, meeting the 64-QAM 3GPP criterion [5]. Consequently, this link has a data capacity of 24 Gb/s. Figure 5.12 shows the received signal for a 20 Gb/s link adopting 4 GBd, 32-QAM.

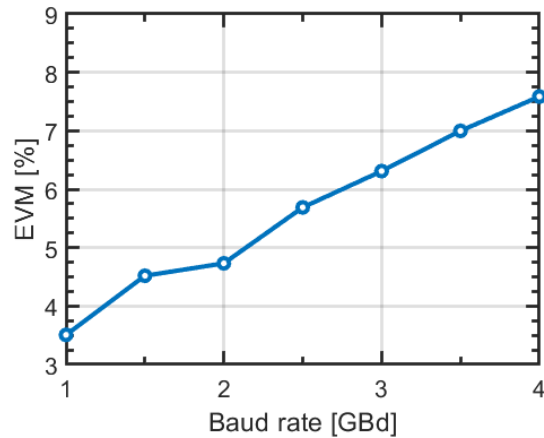


Figure 5.11: DEIM – EVM as a function of the baud rate.

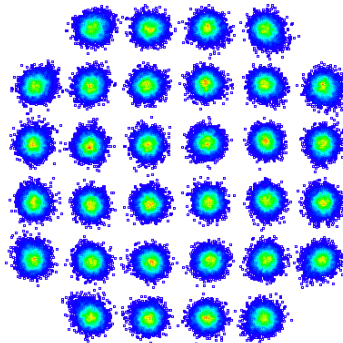


Figure 5.12: DEIM – 4 GBd, 27 GHz, OB2B.

### 5.3.3 Reflective Modulator Operation

In Fig. 5.13, the influence of fiber length in the setup depicted in Fig. 5.8 is looked at. From these results, it is found that a chromatic dispersion notch appears at 4.5 km [6]. Fiber dispersion heavily degrades the signal quality when optical double sideband signals at 28 GHz are transmitted over fiber lengths close to 4.5 km.

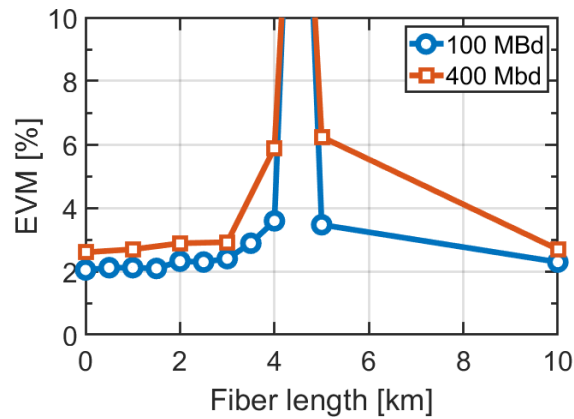


Figure 5.13: DEIM – EVM as a function of SSMF length.

Reflective modulators are devised in this dissertation to allow for laser-free operation in RAUs without the need for circulators at the RAU side or multiple fibers between Central Office (CO) and RAU. Consequently, it should be tested what happens if the fiber in Fig. 5.8 is placed in between the circulator and the DEIM.

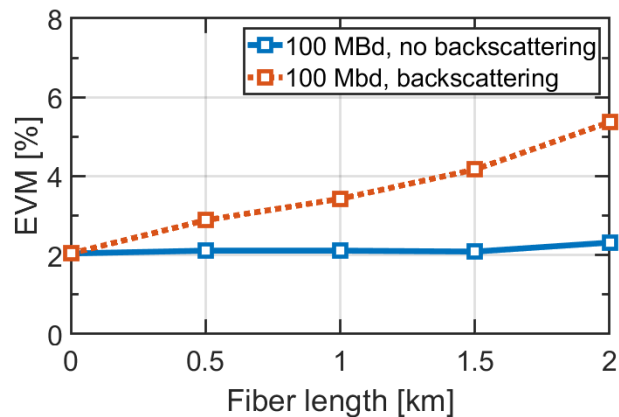


Figure 5.14: DEIM – EVM degradation due to reflective operation.

In Fig. 5.14, the EVM degradation due to reflective operation is looked at. In the original setup (Fig. 5.8), the signal passes in one direction over the fiber. However, when the fiber is placed in between the circulator and DEIM, Rayleigh scattering occurs along the fiber. This results in strong signal degradation, especially at large fiber lengths. The unmodulated light

that is sent to the reflective EAM undergoes distributed reflections while passing along the fiber and this reflected CW tone interferes with the carrier of the modulated light traveling back from the reflective EAM over that same fiber [7]. After 2km SSMF, the EVM increases from 2.32% to 5.37% due to backscattering. The received 16-QAM signals, with SSMF in between the circulator and DEIM, are depicted in Fig. 5.15 for fiber lengths up to 10km.

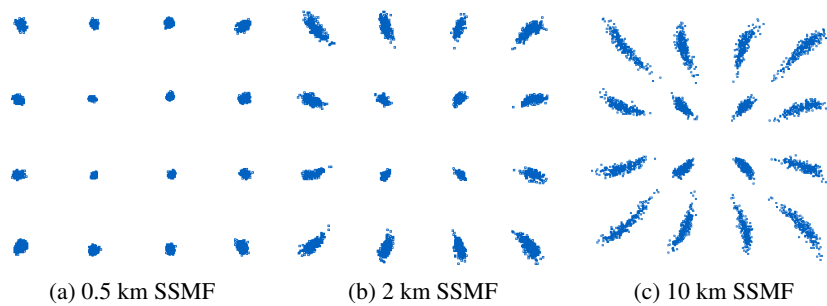


Figure 5.15: DEIM – Received signal when unmodulated and modulated light pass over the same fiber due to reflective operation.

## 5.4 Narrowband mmWave-over-Fiber RAUs

*The work in this section has been published in [8].*

Meeting the demands for future wireless mobile communication will require significant changes in the underlying network [9]. A first important change is the migration to higher carrier frequencies as these bands offer more bandwidth and are less congested than the sub-6 GHz bands. Secondly, a small-cell approach will be adopted to increase the overall data capacity of the network. To allow for the densification of the network, a centralized approach with distributed low-complexity RAUs is of paramount importance. In such a configuration, COs contain the high-complexity functionalities, such as the generation and processing of the RF signal, and subsequently distribute the generated data to the intended RAU using Radio over Fiber (RoF) technology. Typical RoF implementations for mmWave distribution rely on IF-over-Fiber and accomplish the frequency up-conversion at the RAU [10, 11]. This approach requires the distribution of a synchronous carrier which is used to generate a local oscillator signal in the RAU.

In this dissertation, the complexity of the RAU is reduced by adopting RFoF. Furthermore, a reflective EAM, with compact footprint, is used to realize laser-free RAUs, thereby further reducing cost, complexity and weight. In contrast to the broadband approaches used in literature, a dedicated DEIM and photoreceiver are designed for optimal performance in the 28 GHz band using a combination of GaAs pHEMT electronics and silicon photonics. The signal processing and computing resource allocation are transferred to the CO to further simplify the RAU and reduce the latency. This proposed RFoF system features low-complexity, low-cost and easy to install RAUs, which is highly desired in centralized networks and Distributed Antenna Systems (DAS). Besides small signal characterization, the performance and throughput of the RFoF system is evaluated for mmWave communications demonstrating 12 Gb/s transmission over 2km SSMF. After introduction of a 5m wireless path 7 Gb/s transmission is obtained.

#### 5.4.1 Setup

The experimental setup, consisting of both the uplink (UL) and downlink (DL) of the proposed RFoF system, is shown in Fig. 5.16. In this work, the 5G New Radio channels nr257/258 were targeted with frequency ranges between 24.25 and 29.5 GHz. Furthermore, nr257/258 adopt a Time Division Duplexing (TDD) scheme [3].

The downlink path starts with an AWG (*Keysight M8195A*) that generates an IF signal which is subsequently up-converted to the RF frequency. The generated RF signal is amplified by a dedicated narrowband GaAs EAM-driver, which offers a small signal gain of 25.2 dB over a 3-dB bandwidth between 24.4 and 29.5 GHz with a noise figure of 2.0 dB. The driver has an input referred 1-dB compression point of -20 dBm and consumes 124 mW. The output of the GaAs driver is fed to a SiGe reflective EAM coupled to silicon waveguides and modulates the incident CW 1550 nm laser tone incident on the EAM. Since the modulator is reflective, an optical circulator is required to separate the modulated from the unmodulated light. The reflective EAM has a very compact footprint of 340  $\mu\text{m}$  by 220  $\mu\text{m}$  and is fabricated on the iSiPP50G silicon photonics platform with a bandwidth far beyond 28 GHz, which opens the opportunity to realize RFoF systems at even higher frequency bands, such as the extended frequency range in 5G New Radio and the 60-GHz band used by WiGig.

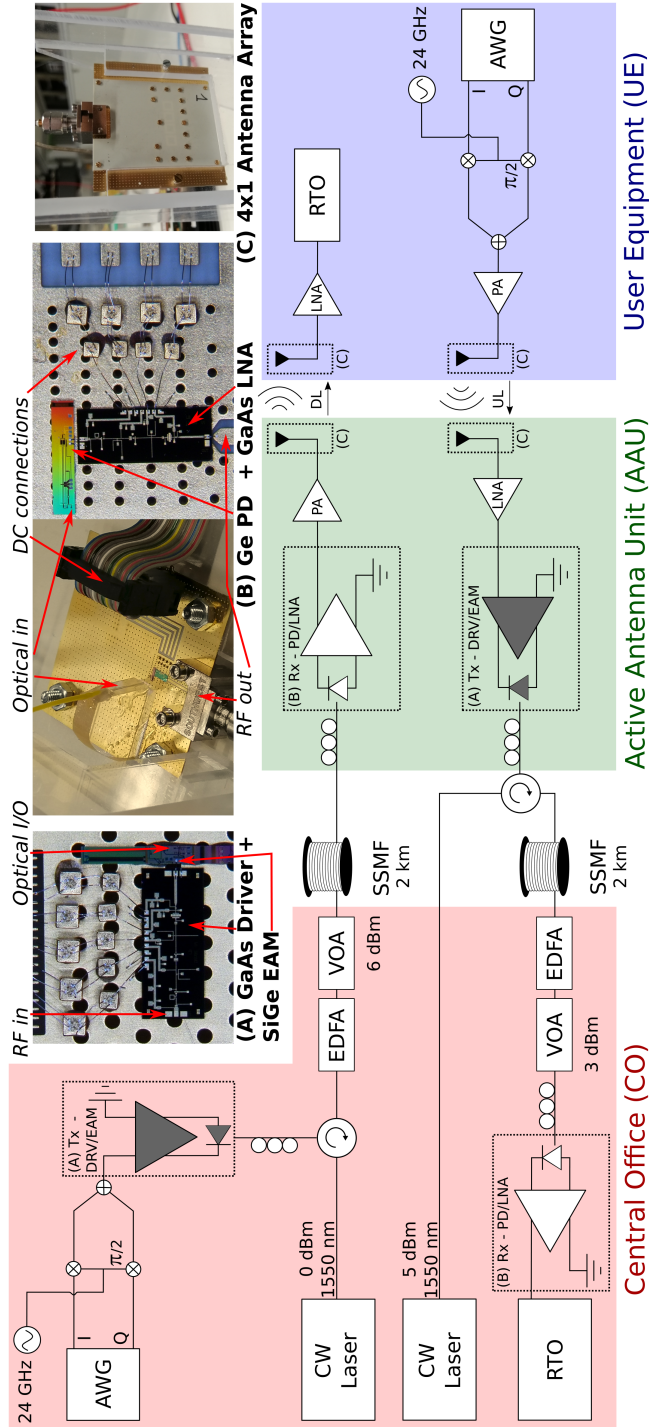


Figure 5.16: Block diagram and experimental setup for bidirectional 28 GHz RFoF link.

An EDFA and a VOA are used to set the power launched into the SSMF. At the RAU, the photoreceiver converts the light back to the RF domain and subsequently amplifies the signal. The devised photoreceiver comprises a silicon waveguide coupled Ge-on-Si Photodetector (PD) and a co-designed GaAs LNA. The LNA offers 24 dB gain, corresponding to 224 V/W external conversion gain, over a 3-dB bandwidth between 23.5 and 31.5 GHz. Its associated noise figure is 2.1 dB and an output referred third order intercept point up to 26.5 dBm can be obtained with a power consumption of 303 mW. The devised narrowband GaAs/SiGe transceiver has a total power consumption of 427 mW (driver and receiver). A commercial power amplifier (HMC943) is added to ensure that the signal fed to the antenna is sufficiently strong (approximately 10 dBm). Furthermore,  $4 \times 1$  linear and passive antenna arrays with integrated Wilkinson splitters are used to achieve beamforming gain in the broadside direction. The downlink signal received by the antenna at the User Equipment (UE) is first amplified and subsequently monitored by a RTO (*Keysight DSA-Z634A*). The captured data was demodulated offline in Matlab.

The uplink path first generates an RF signal and subsequently passes the signal over the wireless link. Next, the signal is amplified with a commercial LNA (HMC1040) and fed to the DEIM which modulates the incident CW laser tone. A reflective EAM was used to enable laser-free operation of the RAU. To separate the CW tone incident on the reflective EAM from the modulated light coming from the EAM, an optical circulator is used. Subsequently, the light passes through SSMF and is converted back to the electrical domain at the central office by making use of the aforementioned photoreceiver.

The transfer function of the RFoF link in OB2B starting from the input of the DEIM to the output of the photoreceiver is shown in Fig. 5.17. The 3-dB bandwidth of the link spans from 24.7 to 28.6 GHz and shows a small signal gain of 28.4 dB when 3 dBm optical power is incident on the photoreceiver.

#### 5.4.2 Multichannel Single Carrier Data Transmission

To explore the maximum RFoF link capacity, downlink multiband single carrier experiments were performed. Five 400 MBd channels centered at 25.0, 25.7, 26.5, 27.2 and 28.0 GHz were transmitted simultaneously over the fiber-wireless link. The EVM values (normalized to the average power) of the transmitted data are measured in the absence of a wireless channel for an OB2B link and compared to different wireless scenarios in Fig. 5.18. For 1m wireless, the EVM stays well below the 8% requirement for

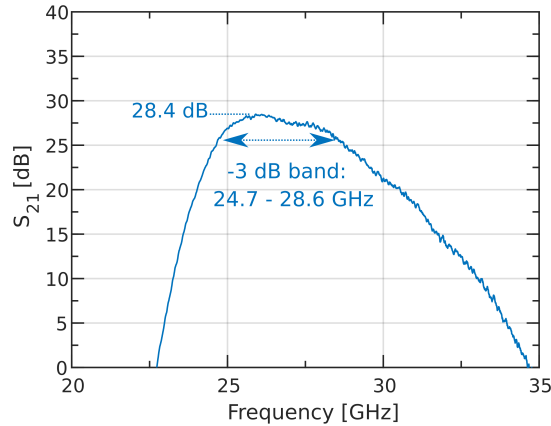


Figure 5.17:  $S_{21}$  narrowband RFoF link .

64-QAM [5]. It should be pointed out that the optical insertion loss and dispersion induced by 2km SSMF has a limited impact on the signal reception quality. When the wireless distance is increased to 3m, the 12.5% EVM requirement for 16-QAM is still met [5]. Consequently, using 5-channel multiband single carrier data transmission allows for data rates up to 12 Gb/s over 1m wireless distance and up to 8 Gb/s over 3m wireless distance in a typical indoor environment. At larger distances, fading significantly degrades the signal quality.

### 5.4.3 Orthogonal Frequency Division Multiplexing

To overcome equalization challenges after fading, OFDM signals were also evaluated for this RFoF system. OFDM signals make the data transmission over the wireless channel more robust at the cost of increased requirements on the dynamic range of the E/O and O/E converters and its associated drivers and amplifiers [12]. The OFDM signal parameters used for each channel and its data rate are summarized in table 5.1. Each OFDM channel can support 2.34 Gb/s using 16-QAM. The uplink and downlink path are tested separately due to the envisioned TDD duplexing mode [3]. For one OFDM channel, the EVM after 2km fiber was below 4%. For three OFDM channels after 2km fiber, all EVMs were below 8% [5] and the averaged EVM was around 6%, as shown in Fig. 5.19. An aggregated capacity of 7.02 Gb/s was achieved over 2km SSMF and 5m wireless distance for both downlink and uplink with an EVM that meets the 3GPP specification. For 1m wireless distance, the measured EVMs can even support 64-QAM, resulting in an aggregated capacity of 10.53 Gb/s for downlink and uplink.

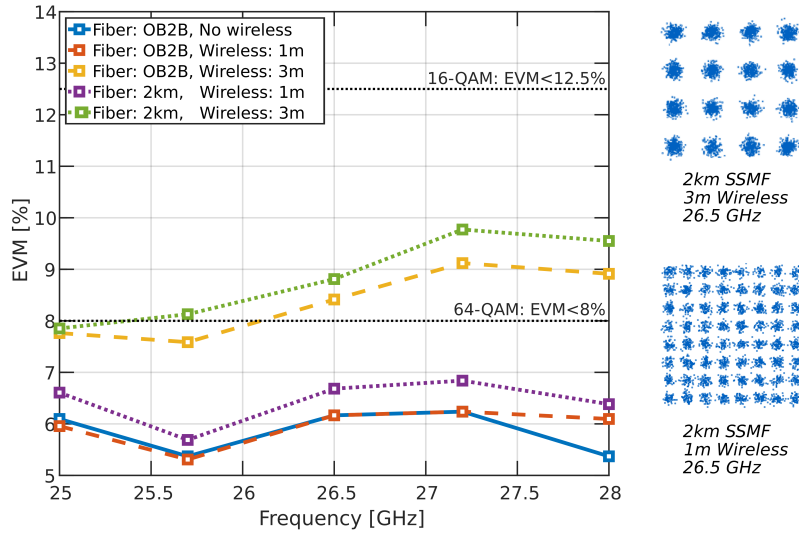


Figure 5.18: Downlink single carrier –  $5 \times 400$  MBaud multiband.

Bandwidth	800 MHz
Number of subcarriers	512
Number of pilots	16
Number of null subcarriers	28
Cyclic prefix (CP) size	1/4
Peak-to-average-ratio	10.8 dB
Data rate per channel (16-QAM)	2.34 Gb/s

Table 5.1: OFDM signal parameters.

## 5.5 Conclusion

The first part of this chapter focuses on the characterization of the standalone photoreceiver and DEIM for 5G New Radio on the one hand and high data rate applications on the other hand. The photoreceiver results in EVM values below 2.46/3.47% for 100/400-MBaud 16-QAM transmission over the 24.25—29.5 GHz band corresponding with new radio channels nr257 and 258. Furthermore, the photoreceiver was used in a high data rate link showing the potential of receiving 36 Gb/s in OB2B configuration at an EVM of 5.2% and 20 Gb/s over 21 km of SSMF at an EVM of 5.8%.

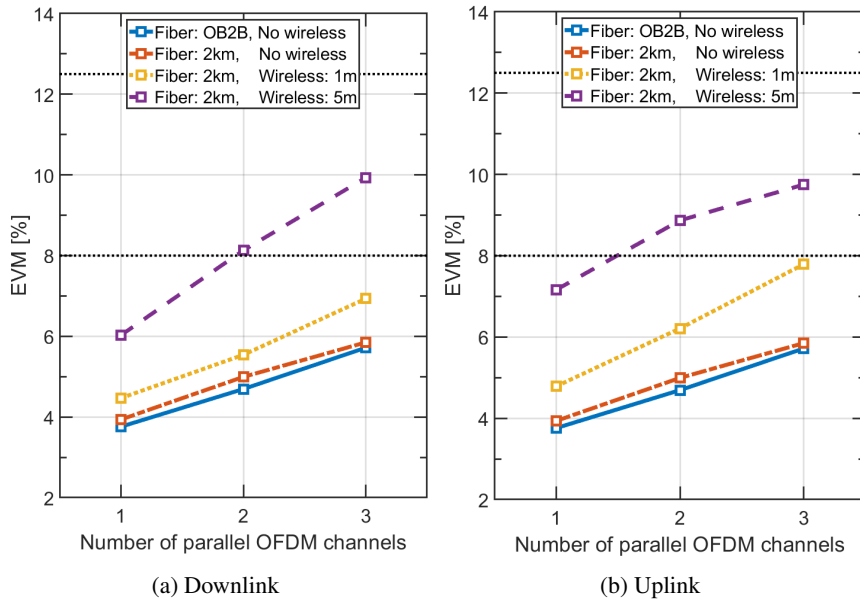


Figure 5.19: Measured EVM in RFoF-wireless for OFDM signals – Data rate per channel = 2.34 Gb/s.

The experiments were repeated for the DEIM assembly (combination of reflective EAM and driver), resulting in EVM values below 2.04/3.09% for 100/400-MBaud 16-QAM transmission over the 24.25–29.5 GHz band. The link consisting of the DEIM assembly and 50 GHz photodetector shows a 24 Gb/s data capacity in an OB2B scenario. Furthermore, it should be noted that Rayleigh backscattering results in severe signal quality degradation when the modulated and unmodulated light are transported over the same fiber.

The final part of this chapter discusses the GaAs electronics/Si photonics bidirectional narrowband transceiver enabling low-cost, low-complexity RAUs for scalable RFoF architectures. The transceiver chipset consumes 427 mW, introduces a link gain of 28.4 dB — with 3 dBm optical power — and supports a link bandwidth from 24.7 to 28.6 GHz. With this transceiver, over 7 Gb/s downlink and uplink were demonstrated for a 2km fiber – 5 m wireless mmWave link with an EVM around 10%. For 2km fiber – 1m wireless, the measured EVMs can even support 64-QAM, resulting in a potential aggregated capacity of 10.53 Gb/s for downlink and uplink.



## References

- [1] L. Bogaert, H. Li, K. Van Gasse, J. Van Kerrebrouck, J. Bauwelinck, G. Roelkens, and G. Torfs, "Narrowband photoreceiver for analog radio-over-fiber in the 24.25-29.5 GHz band," in *45th European Conference on Optical Communication (ECOC)*, 2019, M.2.C.2.
- [2] L. Bogaert, H. Li, K. Van Gasse, J. Van Kerrebrouck, J. Bauwelinck, G. Roelkens, and G. Torfs, "36 Gb/s Narrowband Photoreceiver for mmWave Analog Radio-over-Fiber [Early Access]," *Journal of Lightwave Technology*, 10.1109/JLT.2020.2968149.
- [3] 3GPP, *TR 38.815: New Frequency Range for NR (24.25 -- 29.5 GHz) -- Release 15*, v. 15.0.0, 2018.
- [4] G. Torfs, H. Li, S. Agneessens, J. Bauwelinck, L. Breyne, O. Caytan, W. Joseph, S. Lemey, H. Rogier, A. Thielens, D. Vande Ginste, J. V. Kerrebrouck, G. Vermeeren, X. Yin, and P. Demeester, "Atto: Wireless networking at fiber speed," *Journal of Lightwave Technology*, vol. 36, no. 8, pp. 1468–1477, April 2018.
- [5] 3GPP, *TR 36.104: LTE; Evolved Universal Terrestrial Radio Access (EUTRA); Base Station (BS) radio transmission and reception – Release 15*, v. 15.3.0, 2018.
- [6] U. Gliese, S. Norskov, and T. N. Nielsen, "Chromatic Dispersion in Fiber-Optic Microwave and Millimeter-Wave Links," *IEEE Transactions on Microwave Theory and Techniques*, vol. 44, no. 10, pp. 1716–1724, October 1996.
- [7] G. Talli, C. W. Chow, E. K. MacHale, and P. D. Townsend, "Rayleigh noise mitigation in longreach hybrid DWDM-TDM PONs," *Journal of Optical Networking*, vol. 6, no. 6, pp. 765–776, June 2007.
- [8] L. Bogaert, J. Van Kerrebrouck, H. Li, I. L. De Paula, K. Van Gasse, S. Lemey, H. Rogier, P. Demeester, G. Roelkens, J. Bauwelinck, and

- G. Torfs, “SiPhotonics/GaAs 28-GHz Transceiver for mmWave-over-Fiber Laser-Less Active Antenna Units,” in *Optical Fiber Communications Conference and Exhibition (OFC)*, 2020, Th4A.5.
- [9] J. G. Andrews, S. Buzzi, W. Choi, S. V. Hanly, A. Lozano, A. C. K. Soong, and J. C. Zhang, “What Will 5G Be?” *IEEE Journal on Selected Areas in Communications*, vol. 32, no. 6, pp. 1065–1082, June 2014.
- [10] J. Kim, M. Sung, S. Cho, Y. Won, B. Lim, S. Pyun, J. K. Lee, and J. H. Lee, “OTA Enabled 147.4 Gb/s eCPRI-Equivalent-Rate Radio-Over-Fiber Link Cooperating with mmWave-Based Korea Telecom 5G Mobile Network for Distributed Antenna System,” in *Optical Fiber Communications Conference and Exhibition (OFC)*, 2019.
- [11] N. Argyris, G. Giannoulis, K. Kanta, N. Iliadis, C. Vagionas, S. Papaioannou, G. Kalfas, D. Apostolopoulos, C. Caillaud, H. Debrégeas, N. Pleros, and H. Avramopoulos, “A 5G mmWave Fiber-Wireless IFoF Analog Mobile Fronthaul Link With up to 24-Gb/s Multiband Wireless Capacity,” *Journal of Lightwave Technology*, vol. 37, no. 12, pp. 2883–2891, June 2019.
- [12] A. A. Zaidi, R. Baldemair, H. Tullberg, H. BJORKEGREN, L. Sundstrom, J. Medbo, C. Kilinc, and I. Da Silva, “Waveform and Numerology to Support 5G Services and Requirements,” *IEEE Communications Magazine*, vol. 54, no. 11, pp. 90–98, November 2016.

# 6

## Conclusions & Future Work

### 6.1 Conclusion

To cope with the increased data rate requirements for future wireless links, densification of the cellular network and shifting towards mmWave communication are key. This densification is enabled by the centralization of the complex functionality and optical communication is used to distribute the signal between the Central Office (CO) and the Remote Antenna Units (RAUs). In this work, a next-generation GaAs electronics/Si photonics bidirectional narrowband transceiver was designed enabling low-cost, low-complexity RAUs for scalable Radio Frequency over Fiber (RFoF) architectures. A photoreceiver was designed to retrieve the RF signal from the optical carrier and provide narrowband amplification in the 28 GHz band. Furthermore, the Low Noise Amplifier (LNA) in the photoreceiver was adjusted in a second GaAs design to operate as an Electro-Absorption Modulator (EAM) driver. In combination with a reflective EAM this results in a narrowband reflective transmitter.

The devised photoreceiver comprises a Ge-on-Si photodetector and co-designed GaAs LNA offering 24 dB gain, corresponding to 224V/W external conversion gain, over a 3-dB bandwidth between 23.5 and 31.5 GHz. The associated noise figure is 2.1 dB and an output referred third order intercept point up to 26.5 dBm can be obtained with a power consumption of 303 mW. The devised EAM driver offers 25.2 dB gain, over a 3-dB

bandwidth between 24.4 and 29.5 GHz, and a noise figure of 2.0 dB. The linearity of the driver-EAM combination depends heavily on the operation wavelength and EAM bias. For a 1550 nm signal and a 1V/2V reverse bias, the driver has an input referred 1-dB compression point of -24/-20 dBm. Since the EAM is the limiting factor in the linearity of the transmitter, the drain supply of the driver can be set to 2V without loss of linearity resulting in 124 mW power consumption.

The transceiver chipset consumes 427 mW, introduces a link gain of 28.4 dB — with 3 dBm optical power — and supports a link bandwidth from 24.7 to 28.6 GHz. With this transceiver, over 7 Gb/s downlink and uplink were demonstrated for a 2km fiber – 5 m wireless mmWave link with an Error Vector Magnitude (EVM) around 10%. For 2km fiber – 1m wireless, the measured EVMs can even support 64-QAM, resulting in a potential aggregated capacity of 10.53 Gb/s for downlink and uplink. The complexity and cost of the chipset is low due to the fact that mmWave-over-Fiber is used, in contrast with the IFoF typically used in literature, and because a reflective modulator is adopted, resulting in laser-less operation in the RAU.

Furthermore, two expansions of this demonstrated RAU were looked at, namely the centralization of the amplification functionality and the addition of beamforming. To reduce complexity and cost of the network, centralization will be key. One of the functionalities that is typically not centralized is the amplification. Therefore, shared optical amplification was considered to relax electrical amplification requirements. To accomplish this, high-linearity Photodetectors (PDs) are needed. Multi-PD solutions in combination with a star coupler to limit on-chip optical powers are considered. While multi-PD solutions improve the linearity, they are typically also much slower. In this work, two detector architectures were devised. In a first topology, detector parasitics are included in the transmission line design. This results in a broadband, high-power silicon photonics integrated photodetector with Output referred third order Intercept Point (OIP3) values ranging up to 21 dBm at 28 GHz for a 16-PD array. In a second high-power PD design, the narrowband nature of the wireless communication signal was taken into account. An integrated LC matching network was included between the photodetector array and the interface to the electrical chip resulting in a more compact multi-PD structure with relaxed velocity matching requirements. Furthermore, such a narrowband matched detector-array has the potential to offer a higher conversion efficiency – up to 40% higher output power for a 16-element photodetector – than the broadband traveling wave photodetector.

Finally, beamforming will play a key role in future wireless networks. Beamforming helps to improve power efficiency, reduces the wireless path loss and limits multi-path effects. The trend of centralizing the core functionalities of the network does not hold for beamforming. In case of centralized beamforming, each antenna needs to be addressed separately resulting in an unscalable solution for antenna arrays with a large number of antenna elements. Therefore, a single RF signal is transmitted to the RAU and divided over the different antenna elements. For each antenna element a beamforming coefficient is subsequently applied resulting in a beamsteering phased antenna array. Two variants of the beamsteering array were devised. In a first solution, True Time Delay (TTD) was used based on the switchable optical delay line principle. This is a broadband solution that does not suffer from beam squint, an effect that deviates the beam from the intended steering angle when the carrier frequency deviates from the center frequency. In a second design, the narrowband property of the signal was taken into account and a phase steering device was implemented. To enable optical phase shifting of the RF signal, the data and carrier component of the signal are first deinterleaved using microrings. Subsequently, the carrier experiences a phase shift relative to the data component. Finally, the data and adjusted carrier are recombined and fed to the photodetector. In this work, both devices were measured and the TTD worked as expected while the phase steering suffered from microring extinction ratio issues. The phase steering device however promises a more compact design that is also more future proof with respect to higher RF carriers and upgradability of the antenna array dimensions.

## 6.2 Future Work

### 6.2.1 Optical Beamforming Networks

The first generation TTD Optical Beamforming Network (OBFN) worked and a second generation TTD device was designed to optimize loss, include real-time monitoring of the switch states and include full duplex functionality. The first generation phase steering device unfortunately suffered from a low extinction ratio in the microring resonators resulting in strong parasitic modulation due to the poor de-interleaving of carrier and data components of the signal. Therefore, there is still a need to experimentally verify the phase steering architecture. Furthermore, uplink beamforming based on the adapted power combining tree for perfect optical carrier alignment should be checked.

### 6.2.2 MEMS Switches for True Time Delay

In the TTD OBFN, thermal switches are used to set the delay path and consequently tune the delay difference between neighboring antenna elements. While these thermal switches are compact and are easily implemented, they are slow and consume quite a lot of power (approximately 20-25 mW per control bit on average). Switching speeds are on the order of 10  $\mu$ s which is sufficient for the given application. Power consumption is however the main drawback and should be reduced. Micro-Electro-Mechanical Systems (MEMS) can offer the solution since ultra-low power consumption can be achieved where power is only consumed during switching between delay states [1, 2]. Non-volatile MEMS structures are required to make sure that they are fixed in the set delay state and this is achieved by using mechanical latching. Another important benefit when using MEMS devices to implement the TTD OBFN rather than thermal switches is that thermal crosstalk between switches is avoided.

### 6.2.3 Reflective Modulator

One of the main limitations in the link experiments in Ch. 5 is the fact that the reflective operation suffers from signal degradation due to Rayleigh scattering when the unmodulated and modulated uplink signal are respectively transmitted to the RAU and CO using the same fiber. A first way to deal with this problem is by limiting the fiber length between the CO and RAU. This is for example possible in an environment using atto cells [3] where the communication cells are dense but the maximum distance that needs to be bridged is limited.

The problem during reflective communication is the interference of the carrier in the modulated light with the reflected unmodulated carrier. Hence, increasing the relative power difference between the modulated and unmodulated carrier will also help to relax the Rayleigh scattering induced signal degradation. To accomplish this, one can for example replace the grating couplers with edge couplers. To avoid Rayleigh scattering issues altogether, carrier suppressed modulation at the RAU or carrier reinjection at the CO can be used. In the latter, the carrier passed between CO and RAU is ignored and a kind of coherent detection scheme is adopted.

If none of the above is acceptable, the reflective modulator can be replaced by a regular single-passage EAM, requiring two fibers to communicate between CO and RAU. The laser is still implemented at the CO side, the unmodulated light is passed over one fiber together with the modulated light for the downlink, and the modulated light with the uplink data passes along the other fiber back to the CO.

#### 6.2.4 60 GHz

In this dissertation, designs target the licensed band at 28 GHz. Another band of particular interest for future wireless communication is the unlicensed 60 GHz band which was made available to extend capabilities of WiFi systems into mmWave frequencies [4] known as WiGig. For the transceiver circuits, the same technology platforms can be used. The adopted iSiPP50G silicon photonics platform includes sufficiently fast photodetectors and EAMs. The adopted 0.1  $\mu\text{m}$  pHEMT GaAs platform has a transition frequency  $f_t$  of 130 GHz and at 60 GHz it offers a minimum noise figure of 1.8 dB with an associated gain of 6 dB. Consequently, 60 GHz devices can be constructed with the GaAs platform used in this dissertation. When scaling the developed devices to enable operation in the 60 GHz band, a different integration technique is required. Wirebonding will result in unacceptably large inductance values and flip chipping will be required to reduce these interconnection parasitics and get more predictable inductance values.

At 60 GHz, the wireless path becomes significantly more lossy. On the one hand, Friis formula [5] shows that the free space path loss results in a reduction of the received power with a factor 4 when the frequency is doubled. On the other hand, atmospheric absorption shows a strong attenuation peak at 60 GHz [6]. However, shifting to higher frequencies allows for scaling down the size of the antennas and therefore increases the beamforming gain possible for a given antenna array size.

When the beamforming is implemented optically, shifting to a higher frequency simplifies the phase steering implementation since lower Q-factor rings suffice to separate data and carrier components of the optical signal. For the true time delay implementation, increasing the frequency requires finer delay resolution while maintaining the original antenna array size results in the requirement for maintaining the same maximum required delay setting. Hence, more control bits are required and the delay error should be reduced when increasing the targeted carrier frequency. Consequently, the phase steering approach is more scalable to higher frequencies.

#### 6.2.5 Antenna-on-Interposer

An interposer is used to interconnect the different electrical and optical components of the active RAU. To ensure that optical distribution losses are limited, triplex can be used [7]. The substrate of the interposer typically consists of mono crystalline silicon.

In [8], a microfabrication technique was discussed to implement the antennas in the substrate of the interposer. First, an etching step with KOH

(Potassium Hydroxide) is used to define the antenna cavity due to the well-defined etching angle of KOH in Si ( $54.74^\circ$ ). Subsequently, the cavity walls are plated with gold. Next, a Printed Circuit Board (PCB) is added that includes a stacked patch. This hybrid microfabrication-PCB integration strategy results in excellent performance in terms of radiation efficiency, broadside gain and bandwidth. Additionally, the compact antenna footprint in combination with the large beamwidth and high antenna-to-integration platform isolation makes the antenna element in [8] an attractive building block for multi-antenna systems with beam-steering capabilities.

## References

- [1] N. Quack, H. Sattari, A. Y. Takabayashi, Y. Zhang, P. Verheyen, W. Bogaerts, P. Edinger, C. Errando-Herranz, and K. B. Gylfason, “MEMS-Enabled Silicon Photonic Integrated Devices and Circuits,” *IEEE Journal of Quantum Electronics*, vol. 56, no. 1, February 2020.
- [2] C. Errando-Herranz, A. Y. Takabayashi, P. Edinger, H. Sattari, K. B. Gylfason, and N. Quack, “MEMS for Photonic Integrated Circuits,” *IEEE Journal of Selected Topics in Quantum Electronics*, vol. 26, no. 2, March 2020.
- [3] G. Torfs, H. Li, S. Agneessens, J. Bauwelinck, L. Breyne, O. Caytan, W. Joseph, S. Lemey, H. Rogier, A. Thielens, D. Vande Ginste, J. V. Kerrebrouck, G. Vermeeren, X. Yin, and P. Demeester, “ATTO: Wireless Networking at Fiber Speed,” *Journal of Lightwave Technology*, vol. 36, no. 8, pp. 1468–1477, April 2018.
- [4] X. Lu, V. Petrov, D. Moltchanov, S. Andreev, T. Mahmoodi, and M. Dohler, “5G-U: Conceptualizing Integrated Utilization of Licensed and Unlicensed Spectrum for Future IoT,” *IEEE Communications Magazine*, vol. 57, no. 7, pp. 92–98, July 2019.
- [5] H. T. Friis, “A Note on a Simple Transmission Formula,” *Proceedings of the IRE*, vol. 34, no. 5, pp. 254–256, May 1946.
- [6] J. Wells, “Faster than fiber: The future of multi-G/s wireless,” *IEEE Microwave Magazine*, vol. 10, no. 3, pp. 104–112, May 2009.
- [7] C. G. H. Roeloffzen, M. Hoekman, E. J. Klein *et al.*, “Low-Loss Si<sub>3</sub>N<sub>4</sub> TriPleX Optical Waveguides: Technology and Applications Overview,” *IEEE Journal of Selected Topics in Quantum Electronics*, vol. 24, no. 4, July/August 2018.
- [8] Q. Van den Brande, S. Lemey, S. Cuyvers, S. Poelman, L. De Brabander, O. Caytan, L. Bogaert, I. Lima de Paula, S. Verstuyft, A. C. F. Reyniers, B. Smolders, B. Kuyken, D. Vande Ginste, and H. Rogier, “A

Hybrid Integration Strategy for Compact, Broadband, and Highly Efficient Millimeter-Wave On-Chip Antennas,” *IEEE Antenna and Wireless Propagation Letters*, vol. 18, no. 11, pp. 2424–2428, November 2019.



